

Spontaneous Ignition of a Single Fuel Droplet in

Spontaneous Ignition of a Single Fuel Droplet in
High Temperature and High Pressure Surroundings

(高温高压雰囲気中における単一燃料液滴の自発点火)

Mitsuaki TANABE

田 辺 光 昭

平成7年12月

Mitsuaki TANABE

①

Spontaneous Ignition of a Single Fuel Droplet in
High Temperature and High Pressure Surroundings
(高温高圧雰囲気中における単一燃料液滴の自発点火)

Mitsuaki TANABE

referee: Prof. Michikata KONO

(指導教官 河野通方 教授)

(学籍番号37085 田辺光昭)

学位論文(東京大学)、平成7年12月

Contents

1. Introduction	1
2. Experimental setup and procedure	7
2-2. Experimental setup	7
2-1-1. High pressure chamber and electric furnace	7
2-1-2. Suspender configuration and traverse device	8
2-1-3. Fuel and gas supply system	9
2-1-4. Interferometer	10
2-2. Microgravity facilities	11
2-2-1. Bremen Droptower	11
2-2-2. Parabolic flight with Caravelle airplane	12
2-3. Procedure	12
2-3-1. Normal gravity experiments	12
2-3-2. Droptower experiments	13
2-3-3. Parabolic flight experiments	14
2-4. Data evaluation and definition	14
2-4-1. Droplet diameter	14
2-4-2. Induction times and their origins	15
2-4-3. Interferometer interpretation	15
2-5. Experimental conditions and their accuracies	16
3. Numerical modeling	19
3-1. Governing equations and matching conditions of liquid-gas interface	19
3-1-1. Conservation equations	19
3-1-2. Auxiliary equations	20
3-1-3. Matching conditions at liquid-gas interface	21

3-2.	Properties	21
3-2-1.	Thermodynamic properties	21
3-2-2.	Transport properties	23
3-3.	Computation procedure	24
3-3-1.	Grid arrangement	24
3-3-2.	Numerical methods	24
3-3-3.	Program flow	25
3-4.	Reaction models	26
3-4-1.	10 reaction empirical model of Griffiths	27
3-4-2.	12-step systematically reduced model of Pitsch and Peters	28
3-5.	Assesment of the physical and chemical modelings of the present simulation	28
4.	Phenomenology of droplet ignition	31
4-1.	Temperature history and distribution for the case of two-stage ignition	31
4-1-1.	Temperature field visualization	31
4-1-2.	Radial temperature distribution	32
4-2.	Ignition regions	34
4-2-1.	Characteristic temperatures, ignition regions and their definition	34
4-2-2.	Ambient and fuel dependence of the characteristic temperatures	37
4-3.	Place of ignition	39
4-3-1.	Normal gravity cases	39
4-3-2.	Microgravity cases	41
4-4.	Simulated result	42
4-4-1.	Temperature history and heat release rate of the low- and the high-temperature reactions	42
4-4-2.	Place of ignition, initial flame propagation and diffusion flame establishment	43
4-5.	Discussion	45
4-5-1.	Observed phenomena	46

4-5-2. Analysis on the criticality for the reaction development	47
4-5-3. Interactive process of mixture development and reaction	49
5. Induction times	53
5-1. The first induction time	53
5-1-1. Temperature dependency	54
5-1-2. Pressure dependency	56
5-2. The second induction time	56
5-2-1. Temperature dependency	57
5-2-2. Pressure dependency	60
5-3. The total induction time	60
5-4. Influence of initial droplet diameter	62
5-5. Influence of natural convection	63
5-6. Simulated result	67
5-6-1. The total induction time of numerical simulation	67
5-6-2. Temperature history	68
5-6-3. Sensitivity analysis	68
5-7. Discussion	69
6. Conclusions	71
Nomenclature	
Acknowledgement	
References	
Tables and Figures	
Appendix A. Numerical reconstruction of temperature field with an assumption of axis symmetry.	
Appendix B. Considered reactions in 12 step model of Pitsch and Peters.	
Appendix C. Comprehensive data set of induction times	

1. Introduction

The detailed understanding of spontaneous ignition process is of major interest since many of practical problems associated with this process remain to be solved. Engine knock, for example, is one of these problems. The efficiency of Otto cycle can be improved by increasing its compression ratio. Knocking occurs when the compression ratio is raised. Strong knock may damage engines and therefore it must be avoided. The cause of knocking is clarified to be spontaneous ignition in a cylinder. Controlling ignition characteristics prevents the knocking occurrence and allows a higher compression ratio. Another problem that must be solved promptly is back-fire. The reduction of pollutant emission due to combustion is strongly required currently. Research on pollutant production processes clarified that the best way to reduce NO_x, that is one of the most harmful staff for environment, is to avoid high temperatures during combustion. Lean-premixed combustion is the most favorable for the purpose. The most promising device that can realize this type of combustion with liquid fuels is prevaporized-premixed combustor. Back fire problem arises in the prevaporization-premixing section of the combustor. Fuel is injected in high-temperature and high-pressure air to vaporize and to mix in the section. Although both high temperature and high pressure are favorable conditions to activate chemical reactions, fuel must not burn before it is brought into its combustion section. Ignition in the prevaporization-premixing section yields an unwanted pressure rise and may cause mechanical damages. Not only avoiding spontaneous ignition, but also a well-defined ignition occurrence can serve numerous purposes. An improvement in the efficiency of a

Diesel cycle is possible if the injected fuel starts burning at a desired crank angle, for instance.

Spontaneous ignition of an isolated liquid fuel droplet is the most suited to understand the ignition problem of practical systems. Firstly, it is a heterogeneous system that contains both liquid and gas. Almost all of the practical systems are specified to this category. Knowledge on the droplet ignition process can be utilized for practical problems directly. Secondly, it is the simplest system consisting from a liquid droplet and surrounding gas. If the system is in the absence of gravity, a spherically symmetric phenomenon can be realized about the center of a spherical fuel droplet. This simplicity helps to understand the process by allowing to model in one-dimension [1]. Radial distance from the droplet center is the only dimension since phenomena are identical for all directions.

An amount of research has been carried out on the spontaneous ignition of a droplet due to the demands and the advantages described above. The pioneering works of Faeth et al. [2, 3] dealt with droplet ignition of several fuels under microgravity. Ambient condition dependence of ignition delay and a simple model that put importance on the heat-up and the vapor formation of liquid fuel is made. Experiments and theoretical models for different fuels and ambient conditions have been made by others as well [4-16]. Law and coworkers [4-7] built up a theory combining the transient heat-up of liquid droplet and the Damköhler number dependent ignition criteria for the fuel-air mixture in gas phase. The influence of heat-up characteristics on ignition is investigated by many researchers. Bryant [8] tried to correlate the volatility of fuel and ignition delay, for example. The influence of Damköhler number, that is a ratio between activity of reaction and rate of mass-or heat-transfer, is clarified experimentally by Saitoh [9] and by Nakanishi [10] recently. The numerical models [17-23], that is initially done by Nioka [17], enable more detailed investigations. High

pressure effects and critical behaviors are studied by Ruszalo [18] as well as Tsukamoto[19]. Influence of convective flow is clarified by Tsai [20] with a two-dimensional axis-symmetric model. All of these researcher's interests, however, were the roles of physical processes like evaporation, dissipation or convection. Chemical reactions have been over-simplified in those studies. In the theoretical models, ignition is thought to occur when a particular condition is satisfied somewhere in the gas phase. Even in the numerical models, the simplest global reaction model such as Westbrook's empirical model [24,25] is commonly used. Fuel is oxidized to the final products in one step for such global models. The heat production of the reactions is directly related to the consumption of fuel. This type of reaction model produces significant errors in the heat release history. Transient behaviors of chemical reactions have been completely neglected while extensive considerations were made for that of physical processes. It is necessary to clarify the roles of transient reaction process. The most part of discussions and models that have been made so far falls into vain and needs to be re-examined if the neglected reaction characteristics dominate the ignition process.

The reactions that may control the ignition process have been clarified through the research on premixed gas explosion. From the early studies [26-31], it is known that cool flame(s), that has a flame temperature typically below 1000 K, occurs preceding the occurrence of a hot flame. Chemical reactions yield two-step temperature rise during an ignition process, that is called two-stage ignition. Many studies have been done to model the transient behavior of reactions. A few types of reaction models now are able to simulate the experimentally observed two-step temperature rise. Distinction of reactions for low and high temperatures becomes important in these models. A set of reactions (the low-temperature reactions) is active only at relatively low temperatures and another set (the

high-temperature reactions) is only at high temperatures. The low-temperature reactions cause a cool flame and the high-temperature ones cause a hot flame. As well as the two-stage process, the two types of reactions give a unique temperature dependence of ignition delay. For most of temperatures, ignition delay decreases with increasing temperature. This is a result of a general tendency that the reaction frequency increases with temperature. This is not the case at an intermediate temperature range where the low-temperature reactions switch to the high-temperature one. The low-temperature reactions are inhibited if gas temperature exceeds a certain ceiling value. This inhibition is the cause of the cool flame whose temperature can not exceed a certain value but remains to be cool. Ignition delay increases with temperature at the intermediate range because the low-temperature reactions are inhibited more as temperature increases and because the high-temperature reactions are not active at these low temperatures. This unique temperature dependence is called as NTC (negative temperature coefficient) behavior. The first successful model that predicts the two-stage phenomena and the NTC behavior quantitatively is the Halstead's "shell model" [32,33]. Reaction types and their dependence on reactant concentration or ambient conditions are analyzed theoretically and a set of reaction pattern is selected to produce both cool and hot flames. Even though this empirical model was made before experiments [34-40] uncover some of important reaction paths, the model includes the principle feature that is the degenerated-branched-chain reactions. It is now clarified that the cool flame is induced by those chain reactions that are active only at relatively low temperatures and are inhibited above a ceiling temperature [41,42]. The decomposition-oxidation steps of the high-temperature reactions that cause a hot flame are also well clarified. The increased knowledge on reaction paths and the intermediates involved in the path enabled the detailed

modeling [43-50] of hydrocarbon oxidation. As well as the improvements [51-54] of the shell model by including realistic reaction routes, a completely different approach is possible. The growing computer power and the development of numerical algorithms made the use of detailed model realistic. Thousands of reactions among hundreds of species can be calculated in a reasonable time for dimensionless problems like ignition of homogeneous premixed gas. Every possible reaction can be included at first and unimportant reactions are deleted after sensitivity analysis. Peters introduced a systematic reduction [55] method that outputs a compact reaction model [56-58] keeping the original characteristics of the detailed model. These improved shell models and systematically reduced models are applicable to the numerical model of droplet ignition that is a one-dimensional problem. It is now possible to model the droplet ignition based on a better understanding of chemistry.

A new view point on spontaneous ignition of a droplet, by combining the knowledge of chemistry and the existing understanding on physical processes, must be introduced. Chemical reactions have a transient behavior that is the two-stage ignition process. It is expected to happen also for droplet ignition. All of the existing results are restricted to the occurrence of a hot flame but non of a cool flame. A comprehensive study on droplet ignition dealing both cool and hot flames is required. The present study is aimed to clarify the roles of chemical process including both the low- and the high-temperature reactions as well as physical processes. The temperature field around a droplet and its change with time is observed with an interferometer by using microgravity that realizes the one-dimensional system. An extensive set of experimental data is obtained covering a wide range of temperature and pressure. A numerical model is developed by combining the latest knowledge about chemistry and most reliable physical models. The numerical experiments enabled a closer look at the processes. Ignition process of a droplet is described in detail

based on these observations. A specification of the types of ignition process is done including the two-stage ignition and the mechanisms behind each phenomenon at each process are analyzed considering both chemistry and physics including their interactions.

2. Experimental setup and procedure

A static high pressure chamber system is employed to simulate a fuel droplet that is injected into a high-pressure high-temperature environment. The system consists of a pressure chamber, an electric furnace, optics, fuel and gas supplies and several kinds of controlling elements. The whole system can operate by either remote or automatic control so that it can fit to the microgravity facilities. The configuration is identical for normal-gravity and microgravity experiments.

2-1. Experimental setup

2-1-1. High pressure chamber and electric furnace

A pressure chamber with four windows and two flanges is shown in Fig. 2-1-1. The two windows that exist at the lower portion are omitted in the figure to show the interior. The inner space is $\phi 80 \text{ mm} \times 260 \text{ mm}$ and designed for pressures up to 40 MPa. A furnace is placed at the upper part of the chamber. Its inner hot section is $\phi 30 \text{ mm} \times 40 \text{ mm}$. It is heated with a hot wire driven by pulsed electric current that enables a maximum gas temperature of 1100 K. The hot section is thermally insulated with porous ceramics that has an extremely low heat conductivity. This configuration allows to keep the lower section of the chamber at room temperature and the inside the furnace at high temperature with minimized temperature non-uniformity. The fuel droplet produced at the lower section can

remain in room temperature until it is brought into the furnace.

All the windows are made of reinforced quartz glass so as to withstand the high pressures. Two windows are mounted at the upper side for optical access to the furnace. The other two windows are placed at the lower to monitor the droplet generation procedure. There are two flanges at the upper and the lower side. The upper mounts the furnace, cables to supply electric power, a gas exhaust, and a thermocouple output that measures the furnace temperature. The lower one mounts a mechanism to move a droplet into the furnace (traverse device), a fuel supply nozzle that is retractable by a solenoid, a thermocouple output measuring the gas temperature near the droplet and several cables to control these devices.

2-1-2. Suspender configuration and traverse device

A horizontally placed quartz glass filament is employed to suspend a fuel droplet. Use of suspender is inevitable for the present experiment to control the position of the fuel droplet. The influence of this sort of suspender on droplet evaporation rate has been clarified to be very small from a numerical simulation [59] and it is thought to be small as well for ignition process. The diameter of the suspender filament is 0.15 mm and the tip shapes a sphere that has a diameter of about 0.3 mm as is shown in Fig. 2-1-2. This spherical part holds the droplet. Two thermocouples (type K) are placed in the vicinity of the suspender. One (ϕ 0.1 mm) is at a distance of 8 mm from the tip of the suspender to monitor the furnace temperature (i.e. ambient temperature). The other (ϕ 0.04 mm) is put on the suspender to measure the transient gas phase temperature near the droplet. The horizontal direction of the suspender is chosen not to have any staff on the vertical axis of the droplet. Such a thing will influences ignition behavior [15] by causing natural convection that flows vertically onto the droplet. This

direction also is advantageous to hold the droplet when inserting it into the furnace and therefore a higher insertion speed can be used compared with the case a vertical suspender is employed.

The insertion is done by a traverse device that consists of a rack-and-pinion gear that is driven by a step motor. The stepping of the motor is controlled by a programmable micro-computer. Determination of ignition delays requires a stepwise temperature rise at the insertion and hence an infinitesimal short insertion process. A constant-acceleration constant-deceleration procedure is applied to maximize the speed of insertion as well as preventing the droplet from falling off the suspender. The temperature history that a droplet undergoes during the insertion is shown in Fig. 2-1-3. The whole procedure takes 120 msec for the travel distance of 65 mm. The effective period to vary the temperature from room temperature to the set value is only 30 msec. This is considered to be short enough since the typical time scale of the ignition process observed in this work is the order of 100 msec.

2-1-3. Fuel and gas supply system

Initial diameter of the droplet is one of the most important parameter for the time scale of the ignition process. A step-motor driven fuel pump system shown in Fig. 2-1-4 is employed to control fueling and enables a very precise adjustment of initial diameter. The motor drives a pressure cylinder that is fed with fuel from a reservoir and the pressurized fuel is brought into the chamber with a very fine tube. The fuel is put onto the suspender through a needle nozzle. The nozzle is retractable by a solenoid-driven mechanical link so as not to block the way of the droplet at the insertion.

The ambient gas is brought through a gas supply system shown in Fig. 2-1-5. Since

ambient pressure is an important controlling factor for reactions, its adjustment is done precisely with a regulator and a strain gauge type pressure transducer (SENSOTEC STJE 1833-25) coupled with a factory-calibrated digital meter (buster Sensor Master Type 9158).

2-1-4. Interferometer

The present experiments are aimed to detect cool flames as well as visible hot flames. Cool flames have almost no light emission. The only possible method to observe them is to look at the gas phase temperature. The most-popular thermocouple measurement does not achieve a high response to detect the cool flame appearance unless the thermocouple is placed just at where the cool flame occurs. Interferometry has an advantage over such point measurements because it allows to observe a two-dimensional temperature field with an extremely high time resolution. It can detect cool flames that start from any place. Time resolution is unlimited by the method itself. Only the performance of a device to acquire the images limits it.

A Michelson interferometer is developed for the purpose. A He-Ne laser (632.8 nm) of 1.2 mW is used as the light source and the light beam is expanded to a parallel beam of 15 mm in diameter. The beam is split into reference-beam and object-beam that goes through the test section (i.e. the furnace). The use of laser brings an advantage on the freedom of optics arrangements since different optical path lengths can be used for the reference- and the object-beams for the sake of its high coherence. The beam splitter, the reference- and the object-mirrors are attached directly to the high pressure chamber. This way of attachment is very rigid and is resistant against vibration that is the weakest point of interferometry. A convex singlet lens is used as the camera objective. A CCD (charge coupled device) with 8

mm video recorder and a high-speed camera (in some of experiments) store the interferometric images with a shutter speed of 1/10,000 for both and with a frame rate of 50 and 500 per second respectively.

The sensitivity of the interferometry varies with gas pressure, temperature and with the size of the object. The temperature difference that gives 2π phase shift is expressed as:

$$\frac{\lambda}{2l} \frac{P_0}{(n_0 - 1)T_0} \frac{T^2}{P}$$

where ' λ ' is the wave length of the laser light, ' l ' is the size of the object, ' n ' is the refractive index, ' P ' is pressure and ' T ' is temperature. The subscript ' 0 ' denotes a reference state. For example, if the object sizes 1 mm and the ambient is air of 1 MPa and 700 K, 20 K difference gives 2π phase shift. This performance is powerful enough for the detection of cool flames.

2-2. Microgravity facilities

Two kinds of microgravity facilities are used for microgravity experiments. Droptower experiments are for short term phenomena and parabolic flights are for long ones.

2-2-1. Bremen Droptower

Free-fall in a evacuated tube of 114 m high realizes a high quality of microgravity. The schematic of the droptower is shown in Fig. 2-2-1. The experimental setup is put into a gas-tight capsule so that the setup is operated at atmospheric conditions even the capsule is in vacuum. It realizes about 4.74 seconds' microgravity. The gravity level during the free-fall is

shown in Fig. 2-2-2. A very high quality of microgravity is achieved (less than $1e-5$ g) for the sake of the reduced air drag by the evacuation to less than 10 Pa. At the end of the free fall, capsule is decelerated by entering a pool of small polymer spheres that act as a viscous fluid. The deceleration yields about 40 g.

2-2-2. Parabolic flight with Caravelle airplane

Parabolic flights are performed with the Caravelle twin jet airplane shown in Fig. 2-2-3. The flight profile and the quality of microgravity are also shown in Fig. 2-2-4 and Fig. 2-2-5. It realizes about 20 seconds' microgravity. Its quality is not as high as free-fall facilities. Ignition process is not as sensitive against gravity as combustion process that has more variations in gas temperature around a droplet. This quality could produce the same experimental data as the droptower experiments.

2-3. Procedure

2-3-1. Normal gravity experiments

The furnace temperature is set and kept at least for 30 minutes before an experiment starts so that all the complete set up is in a thermally steady state. The ambient pressure is also adjusted from the time when the furnace is powered and a fine adjustment is done just before the droplet insertion. The ambient gas (air) is introduced from the gas inlet and continuously flowed out from the exhaust when several experiments are done in a sequence. This procedure flushes out combustion products. The minimum interval of each experiment is 5

minutes.

A droplet is formed on the suspender after an ambient condition is prepared. The droplet generation procedure is observed by a CCD camera through the lower window. The fuel nozzle is brought to the suspender to introduce the fuel to the suspender. The sizing of droplet is done by either forwarding or rewarding the fuel pump. The size is checked on a monitor screen and the droplet is inserted into the furnace when it is the desired size and after retracting the fuel nozzle. The droplet is stopped and fixed at the center of the furnace.

The observation of the igniting droplet is started shortly before the insertion. Either interferometric image or direct photograph is recorded. The thermocouple output is recorded as well in some of experiments. The size of droplet is checked from these recorded pictures at the moment when the droplet reaches the center of the furnace and stopped. The experiment is dropped and is repeated whenever the measured size is out of the desired range. To check the size just after insertion is necessary since a part of the droplet has fallen down occasionally during the travel.

2-3-2. Droptower experiments

The same procedure as normal-gravity experiments is used except ambient pressure control. Ambient pressure is adjusted on ground after heating up the furnace. The hot wire is turned off and the ambient cools down to room temperature. The experimental setup is integrated into the drop capsule after this and brought to the top of the droptower. All the electricity is switched off during this period to save battery power. The hot wire is on 30 minute before the free fall and no pressure adjustment is done at this moment.

The insertion of the droplet is done two seconds after starting free-fall to avoid initial

disturbances due to the transition from 1-g to micro-g.

All the experimental procedure is done by a remote control before the free-fall and by an automatic one during the fall.

2-3-3. Parabolic flight experiments

The same procedure as normal-gravity experiments is used except temperature adjustments. All the experiments are done in a sequence that has very tight interval (about 5 minutes) due to the flight schedule offered by the facility. Therefore there are little time to wait until the setup is in thermally steady state. Experimental sequences are started from a higher temperature and the hot wire is switched off between experiments to decrease temperature for the next experiment. It is switched on about 1 minutes before the next parabola starts to hold the temperature. Pressure is kept constant during one sequence.

The insertion of the droplet is done some seconds after the parabola started.

About 30 parabolas is performed in two sequences.

2-4. Data evaluation and definition

2-4-1. Droplet diameter

Diameter of the suspended droplet is measured from a monitor screen that projects the CCD output. The accuracy of the measurement is a few per cents because the measurement precision is a single pixel of the monitor and the magnification of the CCD optics is chosen so that the droplet has about 50 pixels. Since the droplet takes an ellipsoidal shape, the diameter

is defined as that of a sphere that has the same volume as the ellipsoid. Namely,

$$D = (a^2 \cdot b)^{1/3}$$

where, D is diameter, 'a' is the shorter diameter and 'b' is the longer.

2-4-2. Induction times and their origins

Three kinds of induction times are used in this work. First induction time is the time from the insertion of the droplet to the appearance of a cool flame. Second induction time is from the appearance of a cool flame to that of a hot flame. Total induction time is from the insertion to the appearance of a hot flame.

The insertion procedure yields about 120 msec of transient period. Since temperature is one of the most dominant parameter for ignition process, the time when the surrounding gas temperature reaches the set value is chosen as the origin of the above induction times. Namely, 80 msec in the Fig. 2-1-3 is defined to be the origin of induction times.

2-4-3. Interferometer interpretation

A simplified interpretation method is applied to assess the temperature of gas phase. Complete transformation from the interferometric fringe pattern to the temperature field requires a perfectly two-dimensional temperature distribution and to know the composition of gas phase to calculate its refractive index. These are not available in the present measurement. A reasonable treatment, however, is possible.

Microgravity experiments offer spherical symmetric temperature fields, in theory. Assumption of spherical symmetry enables to evaluate the field because it is one-dimension instead of three. Imperfection in the symmetricity observed in the experiments due to the

cooling of the suspender is little and the assumption can be applied.

The composition of the gas is treated as those of standard air here. Though it is a mixture of fuel, reaction intermediates and air in reality, this treatment possibly produces fair estimates of the height of temperature peak like flame temperature. The mixture that gives the maximum temperature does not contain a great portion of fuel. The fuel mass fraction of the stoichiometric mixture is 0.062 for *n*-heptane. This amount does not cause a significant difference in refractive index compared with air alone. Many of other components have refractive indices similar to air, since their molecular weight is similar. Since soot has a very different index, interpretation is not tried when soot appears.

Numerical reconstruction of temperature field with an assumption of axis symmetry, that includes spherical symmetry as a special case, is described in Appendix A.

2-5. Experimental conditions and their accuracy

Fuels used are *n*-heptane, *n*-dodecane and *iso*-octane that have purities of more than 99 per cent. The first two have similar reaction behavior but different physical properties. The first and the third have similar physical properties but different reactions. All of these are typical primary reference fuels of gasoline or kerosene. Their properties are shown in Table 1.

Initial droplet diameter is about 0.7 mm. The deviation allowed will be mentioned in each context or figure.

Ambient gas is air throughout this work. Ambient conditions are pressure of 0.1-2.0 MPa and temperature of 500-1100 K. Since the present context put importance on the two-stage

ignition process, namely the appearance of cool flames and hot flames, the above conditions are chosen.

The accuracy of ambient pressure is about ± 5 percent of absolute value for the droptower experiments and is less than ± 1 per cent for other experiments. The reduced accuracy for the case of droptower experiments is due to the fact that the pressure control is possible only before the system is brought into the droptower. The heating up of the furnace yields a slight pressure increase and compensation for this effect had to be done not at the start of the experiment but before the setup is integrated into the drop capsule.

Ambient temperature has two errors. One is temperature non-uniformity in the hot section, that is approximately 1 K/mm in the vertical direction and less in the horizontal one. The error due to the thermocouple measurement mainly depends on the electric circuit employed (OMRON C5W). It is smaller than ± 0.5 per cent of the temperature value in degree-Celsius. No correction for radiative heat transfer is done. The temperature difference between the place of measurement and that of infinity govern the amount of transfer. For the present case, the infinity is the furnace wall that is heated by hot wire. The difference between the gas temperature at the center of the furnace and the wall temperature is minimized by the use of isolation material and is confirmed to be 30 K at maximum. According to the report of Heitor and Moreira [60], the error is at most 100 K for measuring gas temperature of 1000 K by comparing several cases where thermocouple's bead diameter is 40 to 350 micron. Assuming that the conductive heat transfer between thermocouple and gas is proportional to the temperature difference between them, the maximum possible error (ϵ) for the present case can be estimated by solving the following relation.

$$\epsilon = 1.5e-10 \times [(T+30)^4 - (T+\epsilon)^4], \quad \epsilon, T \text{ in Kelvin}$$

The error is 11 K for ambient temperature of 1000 K and 5 K for 700 K.

The above equation surely overestimates error. Convection or conduction at elevated pressures promotes heat flow to the thermocouple to agree its temperature with that of gas, in reality. In addition, the wall temperature does not have so high temperature everywhere. The temperature is even colder than gas at the place where the windows exist. Since accurate error estimation is impossible and the error is not significant, compensation for radiation does not supply any benefit.

3. Numerical modeling

3-1. Governing equations and matching conditions of liquid-gas interface

The present numerical simulation model is made assuming spherical symmetry and constant pressure. Radiative heat transfer, thermal diffusion, viscosity and kinetic energy term are not taken into account. Liquid phase formulation is simplified by neglecting solution from gas components. Fugacity equilibrium is assumed at the liquid-gas interface. Surface tension is not taken into account.

3-1-1. Conservation equations

Liquid phase

L-1. Mass conservation:
$$\frac{\partial \rho}{\partial t} + \frac{1}{r^2} \cdot \frac{\partial}{\partial r} (r^2 \rho v) = 0$$

L-2. Energy conservation:
$$\frac{\partial \rho h_l}{\partial t} + \frac{1}{r^2} \frac{\partial}{\partial r} (r^2 \rho h_l v) = \frac{1}{r^2} \frac{\partial}{\partial r} (r^2 q_T)$$

Gas phase

G-1. Mass conservation:
$$\frac{\partial \rho}{\partial t} + \frac{1}{r^2} \cdot \frac{\partial}{\partial r} (r^2 \rho v) = 0$$

G-2. Species conservation:
$$\frac{\partial \rho Y_i}{\partial t} + \frac{1}{r^2} \cdot [r^2 \rho Y_i (v + V_i)] = \dot{w}_i$$

G-3. Energy conservation:
$$\frac{\partial \rho h}{\partial t} + \frac{1}{r^2} \frac{\partial}{\partial r} (r^2 \rho h v) = \frac{1}{r^2} \frac{\partial}{\partial r} (r^2 q_T)$$

3-1-2. Auxiliary equations

Liquid phase

L-1-A1. Equation of state: $P = \rho Z_r RT$ (Peng-Robinson type [61])

L-2-A1. Absolute enthalpy: $h_i = h_{i0} + \int_{T_0}^T C_{pi} dT$

L-2-A2. Conductive heat flux: $q_T = \lambda_l \frac{\partial T}{\partial r}$

Gas phase

G-1-A1. Equation of state: $P = \rho RT$

G-2-A1. Diffusive velocity (Oran and Boris [62]):

$$V_i = \sum_j -D_j^i \frac{\partial X_j}{\partial r}$$

where $D_j^i = \frac{D_{mi}}{X_i} \left(1 + Y_i + Y_i^2 + \sum_{k \neq i} \frac{D_{mi} D_{mk}}{D_{ik}^2} X_i X_k \right)$

(for $j = i$)

$$= D_{mi} \left[(1 + Y_j) \frac{D_{mj}}{D_{ij}} + \sum_{k \neq j} \frac{D_{mk} D_{mj}}{D_{ik} D_{kj}} X_k \right]$$

(for $j \neq i$)

and $D_{mj} = \frac{1 - Y_j}{\sum_{k \neq j} \frac{X_k}{D_{jk}}}$

G-3-A1. Absolute enthalpy: $h_i = h_{i0} + \int_{T_0}^T C_{pi} dT$ and $h = \sum_i Y_i h_i$

G-3-A2. Conductive heat flux (Coffee and Heibel [63]):

$$q_T = \lambda_m \frac{\partial T}{\partial r}$$

$$\text{where } \lambda_m = \frac{1}{2} \left[\sum_i (\lambda_i X_i) + \frac{1}{\sum_i (\lambda_i / X_i)} \right]$$

3-1-3. Matching conditions at liquid-gas interface

I-1. Mass flux: $\rho(v - \dot{R})|_{r=R-} = \rho(v - \dot{R})|_{r=R+} = \dot{m}$

I-2. Species flux: $Y_i \dot{m}|_{r=R-} = Y_i (\dot{m} + \rho V_i)|_{r=R+}$

here $Y_i|_{r=R-} = 1$ ($i = \text{fuel}$), $= 0$ ($i \neq \text{fuel}$)

I-3. Energy balance: $q_T|_{r=R-} - q_T|_{r=R+} = \dot{m}L$

I-4. Temperature continuity: $T|_{r=R-} = T|_{r=R+}$

I-5. Fugacity equilibrium: $f_i|_{r=R-} = f_i|_{r=R+}$

3-2. Properties

These properties are taken from Reid et al. [61].

3-2-1. Thermodynamic properties

Liquid phase compression factor, phase equilibrium and latent heat are calculated with the following equations. Fuel-air binary system is used instead of multi-component system for the equilibrium.

P-1. Compression factor Z is given as a solution of the cubic equation;

$$Z^3 - (1-B)Z^2 + (A - 2B - 3B^2)Z - AB + B^2 + B^3 = 0$$

$$\text{where } A = \frac{aP}{R^2T^2} \quad , \quad a = \frac{0.45724R^2T_c^2}{P_c} \left[1 + f_\omega (1 - T_r^{1/2}) \right]^2$$

$$T_r = \frac{T}{T_c}$$

$$f_\omega = 0.37464 + 1.54226\omega - 0.26992\omega^2$$

$$\text{and } B = \frac{bP}{RT} \quad , \quad b = \frac{0.07780RT_c}{P_c}$$

P-2. Binary mixing rules

$$T_{cij} = (T_{ci}T_{cj})^{1/2} (1 - k_{ij})$$

$$V_{cij} = \left(\frac{V_{ci}^{1/3} + V_{cj}^{1/3}}{2} \right)^3$$

$$Z_{cij} = \frac{Z_{ci} + Z_{cj}}{2}$$

$$\omega_{ij} = \frac{\omega_i + \omega_j}{2}$$

$$P_{cij} = \frac{Z_{cij}RT_{cij}}{V_{cij}}$$

P-3. Fugacity

$$f_i = \phi_i X_i P$$

$$\text{where } \ln(\phi_i) = \frac{b_i}{b} (Z - 1) - \ln(Z - B) + \frac{A}{2\sqrt{2}B} \left(\frac{b_i}{b} - \delta_i \right) \ln \left[\frac{Z + (1 + \sqrt{2})B}{Z + (1 - \sqrt{2})B} \right]$$

$$\frac{b_i}{b} = \frac{T_{ci} / P_{ci}}{\sum_j X_j T_{cj} / P_{cj}}$$

$$\delta_i = \frac{2a_i^{1/2}}{a} \sum_j X_j a_j^{1/2} (1 - k_{ij})$$

P-4. Latent heat

$$L = \frac{\partial \ln(\phi_{fuel}^l / \phi_{fuel}^g)}{\partial(1/T)} R$$

Absolute enthalpy and specific heat capacity are calculated with NASA-polynomial form.

For liquid heat capacity, excess heat capacity expressed as following is added. Namely,

P-5. Liquid heat capacity (Rowlinson)

$$C_{pl} = C_{pl_ex} + C_p$$

where

$$\frac{C_{pl_ex}}{R} = 1.45 + (1 - T_r)^{-1} + 0.25\omega \left[17.11 + 25.2(1 - T_r)^{1/3} T_r^{-1} + 1.742(1 - T_r)^{-1} \right]$$

3-2-2. Transport properties

P-6. Liquid thermal conductivity (Roy Thodos)

$$\lambda = \frac{8.757 \left[\exp(0.0464T_r) - \exp(-0.2412T_r) \right] + C \cdot f(T_r)}{210 \left(\frac{T_c M^3}{P_c^4} \right)^{1/6}}$$

where $f(T_r) = -0.152T_r + 1.191T_r^2 - 0.039T_r^3$

and C is a constant (23.27 for *n*-Heptane)

P-7. Gas thermal conductivity (modified Eucken)

$$\lambda_i = \lambda_{tri} \left(0.115 + 0.354 C_{pl} / R \right)$$

$$\lambda_{tri} = 8.322E-4 \cdot \frac{\sqrt{T/M_i}}{\sigma_i^2 \Omega}$$

in addition, a simple pressure correction is done with:

$$\lambda = \lambda \cdot 1.01^{P/P_0} \quad \text{where } P_0 = 0.1 \text{ MPa}$$

P-8. Binary diffusivity(Wilke and Lee)

$$D_{ij} = \frac{\left[3.03 - (0.98 / M_{ij}^{1/2})\right] (10^{-3}) T^{3/2}}{P M_{ij}^{1/2} \sigma_{ij}^2 \Omega}$$

$$\text{where } M_{ij} = 2 \left(1 / M_i + 1 / M_j\right)^{-1}$$

$$\sigma_{ij} = \frac{\sigma_i + \sigma_j}{2}$$

3-3. Computation procedure

A complete program is newly developed for the present work. The same program can simulate ignition process of premixed gas (without transport) or evaporation (without reaction).

3-3-1. Grid arrangement

Since the droplet shrinks as it evaporates, a droplet surface fixed grid is employed. An exponential gridding is applied for the gas phase to increase the accuracy and the efficiency of simulation giving a high resolution near the liquid-gas interface. These methods are explained in the pioneering work of Niioka et al. [17].

3-3-2. Numerical methods

Numerical integration of reacting flow is very stiff when a realistic reaction model is employed. A fully implicit multi-order backward differentiation method by using extrapolants is employed. The formulation is described by Winslow [64]. This algorithm chooses integration order of 2 to 6 and an appropriate time step size according to a truncation error control. The discretization of gradient term is done in second order or higher for all the grid points including the liquid-gas interface. These high-order approximations are applied to reduce the number of time step and that of grid point necessary to produce an accurate result. The present program needs only 5 grid points in liquid phase and 15 in gas phase to produce the results of negligible dependency on grid density.

The set of equations at one grid point is solved with a simplified Newton-Raphson iteration that neglects the off-diagonal elements of Jacobean matrix. Aitken's Δ^2 -method [64] is applied to stabilize and to accelerate the convergence of this iteration. The coupling of all grids is done in the Gauss-Seidel manner.

3-3-3. Program flow

The program produces, in advance, tables of heat conductivity, binary diffusivity, vapor pressure and latent heat at different temperatures. These properties at a given temperature are calculated by interpolating the table.

The procedure at each time step is as follows; 1. Choose a time step size so that the truncation error (relative value) becomes less than $1e-4$. 2. Update history arrays that contain the information at the previous several steps. 3. Calculate boundary conditions. 4. Derive liquid phase values. 5. Derive gas velocity from the mass conservation equation. 6. Iterative solution of temperature and species distribution.

The procedure 3 to 6 is repeated to couple liquid phase and gas phase as well as velocity and the other scalars. The iteration is continued until maximum round-off error (relative value) becomes less than $2e-5$. The thermodynamic and transport properties are updated whenever a change in temperature or in species concentration occurred.

3-4. Reaction models

There are three requirements for reaction models to be applied for the simulation of ignition process of a droplet;

1. Mass and species conservation
2. Inclusion of low temperature reactions. Namely, a branched chain mechanism that can be inhibited at high temperature.
3. Inclusion of high temperature reactions that have fuel consumption process and oxidation process.

The first one is for coupling of a reaction model with the transport model. The second one is necessary to produce the two-stage ignition process. The third one is for a diffusion flame that is formed at the final phase of the ignition process. The reaction types of the second and of the third are important to produce an accurate fuel consumption history and that of heat release both of which characterize the qualitative behavior of the process.

The most promising model is so-called detailed model that consists from thousands of elementary reactions. This kind of reaction model, however, is too large to be solved except it is in zero-dimensional problem. The limited power of the computers requires simplifications

of these models.

Two kinds of simplified reaction model are employed here. One is the empirical-model that consists of least number of reactions based on the realistic reaction path. The 10-reaction model from Griffiths [52] is chosen in the present model from this kind of models. The other is the reduced-model [55] that is made of elementary reactions and that assumes steady-state and equilibrium to reduce the number of species and that of reaction steps. The 12-step model from Pitsch [58] is chosen here.

3-4-1. 10 reaction empirical model of Griffiths

The schematic of the reaction mechanism is shown in Fig. 3-4-1. This model is chosen because it is the simplest one among the models that satisfies the present requirements. It includes the well-known low-temperature branched-chain reactions that are typical for the NTC behavior. It also has a two-step decomposition-oxidation scheme of high-temperature reactions that are initially proposed by Müller et al. [56]. While gas temperature is low, the branched chain (reaction route 8-4-5-7) grows cycle by cycle. Above a ceiling temperature, this chain cycle is inhibited due to the arise of the backward reaction (reaction 6). When temperature is high, the high-temperature reactions (route 1-2) govern the process. In this work, the pre-exponential factor of reaction 5 is modified by a factor of two from the original value for a better agreement with the shock tube ignition experiments of Ciezki and Adomeit [65].

One problem in applying this model is that mass conservation is not taken into account. This is true to the most of this kind of model. Many of intermediate species appearing here are not real ones but are groups or combinations of species. To overcome the problem, the

molecular weight of these imaginary species is chosen so that no mass unbalance happens in the each reaction step. The choice of molecular weights does not affect the reaction itself since every reaction frequency is determined by number density instead of mass density. The only possible error due to mischoices occurs in physical properties. It is not the case of the present work, however, since their properties are taken from that of fuel and an identical diffusivity for all species is used for this reaction model. This is a way of simplification widely used for theoretical analysis. The binary diffusivity of fuel and air is used not to cause a significant error in the evaporation rate. This kind of simplification is reasonable because the reaction scheme itself is made without considering physical properties. This model allows to clarify the roles of the low- and the high-temperature reactions but is not expected to quantify the phenomena.

3-4-2. 12-step systematically reduced model of Pitsch and Peters

In spite of the disadvantage of the amount of calculation over the above empirical model, this model is used to achieve a quantitative prediction. The model consists of 64 reactions among 35 species. All the species are real ones and 19 is treated as steady state forming 12-step reaction path. These steps are shown in Table 2 and Appendix B lists the reactions considered.

This model's reactions are the same as the empirical one in principle. Reactions for middle temperature range, that form a chain through H_2O_2 , are included in addition.

3-5. Assessment of the physical and chemical modeling of the present simulation

Before coupling the transport model and reaction model, the validity of the individual part is checked. Fig. 3-5-1 shows a comparison of squared droplet diameter history between the experimental measurements under microgravity and the present evaporation simulations. The numerical results agree extremely well with the experimental results. Heat-up and thermal expansion of a droplet are reproduced as well as quasi-steady evaporation rate. The droplet life time agrees with experiments within an error of less than 10 per cent at ambient conditions of between 0.1 to 1.0 MPa in pressure and 400 to 800 K in temperature. The higher pressure cases fail to achieve such a good accuracy because the present method of transport properties' derivation is not aimed for near-critical point conditions.

Ignition delays of stoichiometric fuel-air mixture for the 10-reaction empirical model and for the 12-step reduced model are plotted against temperature in the Fig. 3-5-2. Both models successfully reproduced the "negative temperature coefficient (NTC)" behavior. In the NTC region, ignition delay increases with temperature. This is the least requirement to have two-stage ignition process. The NTC behavior is a proof of the inhibition of the low-temperature reactions. Below the NTC region, the low-temperature reactions become more active as temperature increase. In the region, the activity decreases with temperature. Above NTC region, high-temperature reactions govern the ignition process and increased temperature yields shorter ignition delay again. The agreement between experiments and these models is fair for these relatively low pressures like the present experimental conditions because both models are made and tuned to produce the experimental result of 4.2 MPa [65]. The 10-reaction model produces ignition delays shifted up. Although the 12-step model achieves a better agreement with experiments, the average error is several tenths of percentage. Both

models show stronger negative temperature dependence at the intermediate temperature range than the experiments. The transition from the low-temperature reactions dominated ignition to the high-temperature reaction one seems not to be smooth. Further understanding on chemistry is desired to improve these models in the intermediate temperature range.

The present model of physical part is quantitatively reliable and of chemical part qualitatively.

4. Phenomenology of droplet ignition

There are two types of ignition observed from the present experiments. They are single-stage and two-stage ignition. Single-stage ignition is a case where a sudden gas phase temperature rise occurs only once leading a hot flame. Two-stage ignition has twice of it; one leads a cool flame and the other does a hot flame. Since two-stage ignition has not been known for the droplet ignition, a special address is put in this chapter.

Observed processes are described in detail and are specified. The numerical experiments enable a more detailed process analysis including the roles of the low- and the high-temperature reactions.

4-1. Temperature history and distribution for the case of two-stage ignition

4-1-1. Temperature field visualization

The typical of the two-stage ignition process is the existence of a low temperature flame preceding the occurrence of a hot flame. The present experiments clarify the two kinds of flame through visualizing the temperature field around a droplet with the interferometer.

A time varying phase shift distribution obtained with the interferometer in one case of two-stage ignition is shown in Fig. 4-1-1 as false-colored images. The images show different states in one ignition process of a *n*-heptane droplet under microgravity. Temperature is correlated with these phase shifts through optical density that is

approximately gas density.

Before the onset of the first stage, i.e. image 1, the very high optical density in the vicinity of the droplet causes negative phase shift (objective beam is retarded). Gas phase temperature around the droplet before the first stage occurrence is low because the droplet acts as a heat sink. There is almost no chemical heat release that can compensate for the heat loss to the droplet. The reduced temperature yields the higher optical density. Evaporated fuel contributes to the high density as well due to its larger molecular weight than that of the ambient gas (i.e. air). Cooling effect of the suspender is noticeable, too.

A certain temperature rise is seen from the first image to the second. The gas temperature keeps almost a constant value for about 80 msec after it. There is no significant density difference between the second and the third images. A hot flame appears in the fourth images indicating the occurrence of ignition.

Phenomena, in all of the images, seem not to be perfectly spherical even though these are obtained under microgravity condition. This is due to the cooling of the suspender and of the vertical rod on which the suspender is attached. The suspender side is slightly cooler than the other side.

4-1-2. Radial temperature distribution

Radial temperature distribution estimated from the Fig. 4-1-1 is shown in Fig. 4-1-2. The origin of the radial distance is the center of the droplet. Spherical symmetry is assumed on the right-side-hemisphere of the droplet for the interpretation from phase shift distribution to temperature. The interferometric images show phase shifts that are integrated through the object beam path. Inversion from the integrated value to the

original concentric phase shift distribution is explained in Appendix A. The first stage of ignition starts between curve 1 and 2 in the figure, leading to a temperature of about 750 K. The temperature remains almost constant during the first stage. This plateau temperature agrees with the temperature of a cool flame stabilized by the premixed burner of Morley [34]. The same mechanism of cool flame as that of premixed gas ignition is controlling the phenomena. This first stage has a temperature plateau because the degenerated branched chain reaction, which is typical low-temperature reactions, is inhibited when temperature exceeds a ceiling value.

The temperature field during the first stage of a cool flame does not have a clear peak as is the case of a diffusion flame. Diffusion flame has a very local reaction zone defined by the supply of fuel and oxygen through diffusion. The reaction zone exists just at the place where fuel meets oxygen with a suitable stoichiometry. The cool flame of the first stage is not such a diffusion flame. The reactions and its heat release are governed not by diffusive supply of reactants but by the temperature dependency of the reactions themselves. The partially premixed condition around the droplet realizes the cool flame everywhere forming a very wide high-temperature zone. The cool flame can behave like that of premixed gas. The slight decrease in the maximum temperature between curve 2 and 3 can be explained by the dynamic behavior of the cool flames [67]. The first stage once reaches a temperature higher than an equilibrium temperature at which the heat release through the inhibited reactions balances heat dissipation. A certain stock of intermediates is formed by the chain reaction before the occurrence of the cool flame. These intermediates go heat release step when temperature starts raising. The heat release step works separately from the chain. It is seen also in the Griffiths' model. The heat release step is the reaction numbered as 9

and 10 in Fig. 3-4-1 that is not a part of chain. The pooled intermediates can produce heat, if the amount is enough, even after the ceiling temperature is reached and chain is inhibited. This realizes an excess temperature. The temperature rise stops after consuming almost all of the intermediates and there will be less heat release in the succeeding because the chain can keep producing only little amount of these intermediates. The exceeded temperature slowly settles down to the equilibrium temperature.

4-2. Ignition regions

4-2-1. Characteristic temperatures, ignition regions and their definition

There are three types of critical temperature that are defined here for a given pressure condition. The first one is cool flame lower limit. The first stage is observed at ambient temperatures higher than this limit. The second is cool flame upper limit. Since the low-temperature reactions are not active above a ceiling temperature, the first stage of a cool flame does not occur when ambient temperature is too high. Cool flame is observed only at temperatures below this limit. There are certain cases where the ambient temperature is higher than the temperature of a cool flame and the first stage still exists. In these cases, a cool flame appears in the very vicinity of the droplet where the local gas temperature is below the cool flame temperature due to the cooling effect of the droplet. The third is hot flame lower limit below which the second stage is not observed. Hot flame appears at temperatures higher than the limit. For both of these two lower limits, the definition is taken as the appearance of cool or hot flames during the droplet life time, i.e. before the

completion of droplet evaporation.

Cool flame temperature is also plotted in the figures. These temperatures are determined from the direction of natural convection caused by the cool flame. There is no buoyancy nor sedimentation force that causes convection if density at the cool flame region and that of ambient are almost identical. When the cool flame takes spherical shape under normal gravity, ambient temperature is thought to be equal to the cool flame temperature. The mean molecular weight of the cool flame region is slightly high compared with that of ambient because the region contains fuel and other intermediates which are large molecules. Accordingly, the current method slightly underestimates cool flame temperature. The variation of cool flame temperature on initial mixture conditions in gas phase is not considered. In spite of these points that yields less accuracy, the obtained value agrees fairly with the result of temperature measurement [34] of a burner-stabilized cool flame with a thermocouple. The present cool flame temperature can be used as an approximate value.

Ignition phenomena are specified to the following four regions by using the aforementioned critical temperatures. They are no-ignition, cool-flame, single-stage ignition and two-stage-ignition regions. There is a certain temperature rise but it yields neither cool flame nor hot flame in the no-ignition region. Cool flame alone or hot flame alone appears in the cool-flame region or ignition region respectively. A cool flame followed by a hot flame is observed in the two-stage ignition region. These regions are shown in the Fig. 4-2-1 to 4-2-3 for different fuels.

No cool flame is observed for *iso*-octane droplet. The activity of the low-temperature reactions is governed by a process that is the internal hydrogen abstraction through which the reaction chain is branched [41]. The abstraction process requires a ring structure

consists of typically more than five members. The structure of *iso*-octane molecule has less freedom of bending and it is hard to form a ring structure compared with the other two fuels that have long straight chains [44]. This yields fewer opportunities of the internal abstraction and hence less-active low-temperature reactions. The resulting temperature rise is too little and is too slow to be specified to a cool flame.

These figures clearly show the relative importance of chemical characteristics on the type of ignition process compared with physical ones (i.e. heating up, evaporation rate or diffusion) from a phenomenological point of view. Since the structure and the reactions of *n*-heptane and of *iso*-octane are different, the ignition regions take very different locations in spite of the similarity in their physical properties. On the other hand, the regions of *n*-heptane and *n*-dodecane are very similar though their physical properties are different. In addition, the locations of the regions agree with those of homogeneous premixed gas ignition [26,27,42] that are free from physical processes.

Cool-flame region exists at low pressure and in the middle temperature range for the two normal alkanes. The low-temperature- or high-temperature border of the region meets the no-ignition region. The high-temperature and high-pressure side of the region meet the two-stage ignition region. Note that cool flames appear also in the two-stage ignition region.

There are two separated no-ignition regions for these figures. They are where almost no temperature rise can be seen during the droplet life time. The only one no-ignition region of *iso*-octane is the same case.

There are also two separated single-stage ignition regions. In the one that exists at lower temperatures, the process is equal to the two-stage region in principle. The low-

temperature reactions cause a certain temperature rise and immediately yield a hot flame by activating the high-temperature reactions. It can be specified to a special case of two-stage ignition where the duration of the first stage is infinitesimal. In the current definition, the case where the duration is shorter than the temporal resolution of the measurement (i.e. 20 msec) is treated as single-stage ignition. The single-stage region at the higher temperatures is where the high-temperature reactions instead of the low-temperature ones lead the process. The high-temperature reactions cause a hot flame before the low-temperature ones cause a cool flame.

4-2-2. Ambient and fuel dependence of the characteristic temperatures

Cool flame temperature increases with pressure. This is simply due to the characteristics of the low-temperature reactions. The ceiling temperature of the low-temperature reactions is governed by the equilibrium of an oxygen addition process [41]. The reaction chain of the low-temperature reaction propagates through this step. The process goes forward while temperature is low. The reverse step arises as temperature increase since the activation energy of the reverse step is higher than that of the forward one. The process stops going forward when temperature exceeds a ceiling value. Since the forward step of this reaction is two-body reaction and the reverse step is single-body reaction, the process prefers forward as pressure increase. The ceiling temperature rises with pressure due to this increase in forgoing speed of this process.

At low pressures (0.1 to 0.5 MPa) the hot flame lower limit decreases with increasing pressure. The decrease is in one part due to the activity of the high-temperature reactions. The rate of the reactions is estimated to be proportional to the -1.75th power of pressure

[25]. When pressure is high, even low ambient temperatures can activate the high-temperature reactions to cause ignition. The other reason of the decrease is the existence of the first stage at the middle temperature range. The temperature rise at the first stage activates the high-temperature reactions regardless of ambient temperature. When the second-stage lower limit comes below the first-stage upper limit as pressure increases, it suddenly decreases to agree with the cool flame lower limit. Cool flame preceding a hot flame surely promotes the activity of the high-temperature reactions through its temperature rise. The increased cool flame temperature at high pressures makes ignition more probable because the higher temperature activates more the high-temperature reactions. The hot flame lower limit at low pressures (i.e. when it exists at high temperatures) is determined by the high-temperature reactions and that at high pressures (i.e. when it exists at low temperatures) by the low-temperature ones. The tendency of the hot flame lower limit is equal to the all of these fuels. Even though no observable cool flame occurs for the case of *iso*-octane, the distinction of the low- and the high-temperature reactions seems to be important. Namely, the low-temperature reactions of *iso*-octane play the same roles on ignition process as those of normal alkanes through its slow reaction rather than a cool flame.

The temperature of the border between the lower no-ignition region and either cool-flame- or ignition-region increases with pressure. The activity of chemical reactions is higher in general at higher pressures. Hence, reaction alone must realize decreased lower limits at higher pressures. The contrary tendency of these figures requires reasons other than reaction. Change in physical process must explain the tendency. There are influences of natural convection. The stronger natural convection at higher pressures yields

higher loss of heat and mass from a reactive place causing a slower reaction development. The reactivity of chemical reactions is reduced by the stronger convection because the intermediates and the produced heat are removed by it. The higher rates of diffusive mass transfer (dissipation) at high pressures have the same influence. The stronger convection and dissipation also play a role on the life time of a droplet that is one controlling factor of the limits. Droplet life time needs to be longer than the time to induce active reactions. Both the strong natural convection and higher dissipation rate indicate an increased heat transfer to the droplet [67]. Evaporation is promoted with the increased heat flow. Droplet life time is shorter as pressure increases. These tendencies are also confirmed experimentally by Nomura [68]. The sum of these influences results in the increase of the lower limits with pressure.

The cool flame upper limit increases with pressure. The reason is simply that the temperature range where the low-temperature reactions are active shift to the higher region due to the elevated ceiling temperature at high pressures.

4-3. Place of ignition

4-3-1. Normal gravity cases

Gravity yields natural convection. The place of ignition under normal gravity is influenced by the convection. Typical sequences for the three different ignition types are shown in Fig. 4-3-1 to 3 as interferometric images.

Ignition process starts from the heating up of the droplet and evaporation of fuel.

Since the evaporated fuel has lower temperature than the ambient gas and since fuel has larger molecular weight, the vapor has higher density. Natural convection during the evaporation phase flows downward. This convective flow forms a preferable condition for reactions at the down side of the droplet. There is a large amount of fuel-air mixture below the droplet and it is distributed widely compared with the upper side. The dissipation rate below the droplet is smaller than that above it. The convective flow itself is weakened as it goes far from the droplet. Weaker convection is also preferable due to the less loss of heat and intermediates from reactive region. The stagnation point at upper side of the droplet is free from convection, too. This place, however, is not suitable for the development of reactions since the flow field there is extremely stretched. As a consequence, a cool flame or a hot flame of single-stage ignition starts below the droplet.

A hot flame for the case of two-stage ignition shown in Fig. 4-3-2 starts above the droplet, on the contrary. A cool flame is burning before the occurrence of a hot flame. The cool flame causes upward convection for this case. The most preferable place for ignition is above the droplet for the same reason as it is below when convection is downward. Cool flame does not cause upward convective flow when its temperature is nearly equal to the ambient or when the duration of cool flame is very short. A hot flame starts spherically about the droplet for this case (See Fig. 4-3-3).

These clarify the fact that the most reactive place always exists at the down stream of a convective flow. This agrees with the numerical analysis of droplet ignition in forced convection done by Tsai and Yang [20]. They predicted a hot flame occurrence from the wake region.

4-3-2. Microgravity cases

Since the convective flow field around a droplet is spherical symmetric, the place of ignition mirrors the other influences clearly. Three cases are shown in Fig. 4-3-4 and 4-3-6.

The place of the cool flame occurrence at the lowest temperature case (Fig. 4-3-4) is far from the droplet. Reactions are expected to be more active at hotter places and a cool flame starts from the outer edge of the temperature-fuel boundary layer formed by dissipative transfer. The starting point is situated on the other side of the suspender. The suspender side has slightly lower temperature than the other side due to the cooling of the suspender. A hot flame appears before the cool flame reaches the droplet. The cool flame induces a hot flame while its propagation.

A cool flame starts near the droplet and it propagates to surround the droplet for the middle temperature case (Fig. 4-3-5). The temperature-fuel boundary layer for this case is smaller than the former case. Induction time is short and the layer can not develop as widely as the lower temperature case. A hot flame appears after a steady cool flame is established. The place of the hot flame occurrence is different from the lower temperature case. The temperature of the steady cool flame is controlling it. The temperature of the cool flame seems to be high very near the droplet where mixture has fuel-rich conditions.

For the highest temperature case (Fig. 4-3-6), ignition is single-stage and a hot flame starts from the other side of the suspender. It starts from the side because temperature there is hotter than the suspender side. Ignition place is close to the droplet because induction time is very short and can not form a widely spreaded temperature-fuel layer.

4-4. Simulated result

4-4-1. Temperature history and heat release rate of the low- and the high-temperature reactions

A typical calculated temperature history in the case of two-stage ignition by using the empirical 10-reaction model is shown in Fig. 4-4-1. The two-step temperature rise can be seen clearly. The low-temperature reactions cause the first temperature rise and after the temperature reaches around 1100 K the reactions are inhibited. After a while, the high-temperature reactions are activated to cause ignition. Since these high temperature reactions do not have a ceiling temperature, the temperature rise continues until either fuel or oxygen is consumed completely. This two-step temperature rise agrees with the experimentally observed phenomena except the temperature of the first stage (i.e. cool flame temperature). The present model shows advantages over the conventional models [17-23] that do not reproduce the first stage even qualitatively.

The roles of the low- and the high-temperature reactions on ignition process can be evaluated by tracing their heat production over time that is the measure of the activity of the reactions. Chemical heat release rates normalized by gas phase heat capacity is shown in Fig. 4-4-2. The heat release is divided into that of the low-temperature reactions and of the high-temperature ones. Both values are taken from a grid point where total heat release rate is the maximum among all the grid points. The low-temperature reactions are leading heat release almost all the time. The low-temperature reactions produce heat from the early stage of the ignition process. The heat release increases as the amount of their intermediates increases. The constant exponential increase of heat production with time,

that appears as a straight line in the figure's coordinates, is the typical for a chain reaction that grows cycle by cycle. When gas temperature reaches the ceiling value, the heat release rate decreases due to the inhibition. The high-temperature reactions do not dominate the heat release until ignition process comes to the final phase. Their heat release keeps constant almost all the time. The heat release of the high-temperature reactions has a very strong dependence on the maximum gas temperature seen in the previous figure.

4-4-2. Place of ignition, initial flame propagation and diffusion flame establishment

The low-temperature reactions employed here demonstrate a unique process to the diffusion flame establishment. Time varying temperature distribution is shown in Fig. 4-4-3 and 4-4-4. Ambient temperature of Fig. 4-4-3 is lower than the temperature at which the low-temperature reactions are most active (i.e. below the NTC temperature region) and that of Fig. 4-4-4 is higher (in the NTC temperature).

Although ignition is induced by the low-temperature reactions in both cases, the succeeding process to the establishment of a diffusion flame differs. For the lower ambient temperature case, i.e. for Fig. 4-4-3, the initial temperature peak propagates inward to the droplet until it reaches the maximum value. After the maximum temperature is reached, the reaction zone propagates both in- and outwards. The inward propagation is due to the reaction between fuel and oxygen through the high-temperature reactions. It stops after consuming oxygen in the vicinity of the droplet. The outward one is the reaction between low-temperature intermediates and oxygen. It stops after consuming the intermediates. For the higher ambient temperature case, the initial temperature peak moves outward. The succeeding flame propagation to both directions happens as well. In this case, both of the

propagation are due to the reaction between fuel and oxygen through the high-temperature reactions.

The most characteristic difference between the phenomena of these figures is the relation between the location of initial temperature rise and that of maximum temperature. Initial temperature rise starts outside the place where the maximum temperature happens for lower ambient temperature case while it starts inside for the case of higher ambient temperature. Since the location of the maximum temperature is approximately where gas mixture is in the stoichiometric condition, it means that ignition starts from a point of lean condition for the lower temperature case and from that of rich condition for the higher temperature case.

Preceding ignition, a spherical vapor and temperature boundary layer are formed around the droplet, which is due to the evaporation and diffusion of fuel and to the cooling effect of the droplet respectively. For ambient temperatures below the ceiling temperature, the reactivity of the reactions increases with increasing gas temperature everywhere. Therefore the most reactive point is away from the droplet where gas temperature is high, namely the outer edge of the vapor boundary layer will be the starting place of a cool flame. Cool flame starts from a lean region and propagates inward with increasing its temperature. The increased temperature activates the high-temperature reactions and causes a hot flame. There is a partial premixed region inside the initial temperature peak and there is almost no fuel outside. This results in the inward propagation.

Situation differs if ambient temperature is in the NTC region. The low-temperature reactions prefer a place close to the droplet where gas is cooled by the droplet because there is a particular temperature for the low-temperature reactions to be most active and it is

lower than the ambient temperature. Cool flame does not start from the edge but from somewhere in the middle of the temperature boundary layer for this case. Since fuel vapor layer is closely related to the temperature boundary layer, this means that the starting point is the middle of the fuel layer. After the occurrence of a cool flame, a widely spread high temperature region is formed around the starting point of the cool flame. The cool flame can spread because there is fuel enough both inside and outside of the starting point. A hot flame starts from the place where temperature is maximum among the wide high temperature region. The place of highest temperature exists at a fuel rich place. The stoichiometric fuel-to-oxygen ratio of the low-temperature chain, that controls the ceiling behavior, is high compared with the ratio of its total oxidation process. Highest cool flame temperature at a given pressure is attainable for a "fuel-rich" (in terms of total oxidation step) condition. Hot flame starts from a fuel rich place. Since there is fuel outside the place of the initial temperature rise, the initial flame propagates mainly outward. It is a unique fact that ignition can happen from the place of fuel rich condition and it is due to the particular behavior of the low-temperature reactions.

For temperatures much higher than the ceiling value (above the NTC region), ignition is dominated by the high-temperature reactions. Since the high-temperature reactions prefer higher temperatures, ignition takes place at a point of fuel lean condition by the same mechanism as the case of Fig. 4-4-3 with the low-temperature reactions at an ambient temperature below the NTC region.

4-5. Discussion

4-5-1. Observed phenomena

Experimentally observed phenomena can be summarized as follows;

1. The process can take a type of either no-ignition, cool flame, single-stage ignition or two-stage ignition according to ambient condition.
2. Reaction characteristics of fuel determine the characteristics of ignition type that is specified to the above four regions. The employed normal alkanes have cool flame occurrence and hence the first stage temperature rise while it is not observed for *iso*-octane.
3. The first stage has ceiling temperature that is approximately 750 K and that increases with pressure.
4. Ignition occurs near the droplet where fuel-rich conditions exist when ambient temperature is in the NTC region. For other temperatures, a hotter place is preferred.

The observed phenomena agree with those observed for the spontaneous ignition process of premixed gases. The phenomenological aspect of the ignition process of a droplet is mainly determined by the chemical reactions that is unique to the each fuel. The ignition process is able to be explained with the knowledge that is obtained by the researches on chemistry.

The branched chain reaction, that is inhibited at temperatures above a ceiling value due to the equilibrium of the second oxygen addition, causes the first stage. The forward shift of the equilibrium reaction with increasing pressure realizes higher values of the ceiling temperature at high pressures and hence higher cool flame temperatures. The differences in molecular structure govern the reactivity of the low-temperature reactions. The freedom in

bending the molecular chain of normal alkanes gives more opportunities for a chain propagation step, yielding the relatively active low-temperature reactions compared with *iso*-octane that has no straight chain. The second stage is caused by the high-temperature reactions.

4-5-2. Analysis on the criticality for the reaction development

Ignition process up to the onset of the first stage can be analyzed without considering temperature rise due to chemical heat production. The process has criticality for the reaction development. That is, the rate of chemical reaction must be higher than the rate of dissipation to cause the first stage. The transient reaction rate and dissipation rate can be assessed by using evaporation model of a droplet and a model of premixed gas ignition respectively.

A schematic explanation on the transient vapor formation can be done with Fig. 4-5-1. Time varying gas phase conditions around a droplet are plotted on a plane of temperature versus fuel mass fraction. Each straight line expresses a set of conditions existing in gas phase at an instance. The line will be called as "transient flamelet" and the diagram as "flamelet plot" in the following for convenience. The line can be straight on an assumption of unit Lewis number. The line moves as time goes on and as physical process proceeds. Ambient condition remains constant throughout the process. Surface condition changes. At the moment when a droplet is suddenly exposed to a high temperature ambient, its surface is cold and vapor pressure is low realizing the line denoted as 'initial state'. The droplet is heated up by the heat flow from the hot ambient to the droplet. The surface temperature rises gradually and yields higher fuel mass fraction at the surface through the

increase in vapor pressure. The trajectory of continuously varying surface condition is also shown. The trajectory is equal to the liquid-gas phase equilibrium conditions. The change in surface condition stops after a quasi-steady state is reached.

Figure 4-5-2 shows a change in conditions of gas mixture for the three ambient temperature cases that is calculated with the present simulation model without the reaction term. The stoichiometric fuel-air mixture exists somewhere in gas phase and this mixture is taken as a sample. The temperature of the mixture rises with time and as the line in the previous figure shifts upward by the change in the surface condition. As this temperature rise, the reactivity of this mixture increases. The reactivity is approximated with the reciprocal of the first induction time for premixed gas ignition at these temperatures. The history is shown in Fig. 4-5-3. The 12-step reduced model [58] is used to calculate the first induction time. These reactivities increase more than two orders of magnitude for unit magnitude of time. Dissipation rate for the point of stoichiometry is also calculated from the simulation and its temporal decay is shown in Fig. 4-5-4. Ambient temperature does not have significant influence on the history of dissipation rate throughout the droplet life time. Fuel and temperature field develop widely in physical space with time. Gradient of these two scalars becomes less and less. It decreases approximately one order of magnitude for unit magnitude of time increase. The amount of dissipation is almost proportional to the reciprocal of time, namely. Dissipation is more than reaction at the very beginning of the ignition process. The increase in the reactivity and the decrease in the dissipation rate bring a chance for the chemical reactions to develop. If the production of heat or species due to reaction is faster than the loss due to dissipation, the reaction is sustained and causes the first stage. The ratio of reactivity and dissipation rate is a kind of

Damköhler number and is shown in Fig. 4-5-5. Above a certain value of the number, the reaction has a chance to cause the first stage. Considering the first induction time that will be shown in the next chapter, about 10 is the critical value for the present definition.

The slow decay in the dissipation rate and the quick increase in the reactivity through temperature rise indicate the relative importance of the two controlling factor for the occurrence of the first stage. Heat-up characteristics instead of dissipation decay control the process mainly. In addition, the ambient temperature dependence of the characteristics of the first stage occurrence must be explained through the difference in reactivity rather than dissipation because dissipation history is nearly identical for different ambient temperatures. Therefore the mixture formation and the reactivity variation must be emphasized for the interpretation of the observed phenomena.

4-5-3. Interactive process of mixture development and reaction

A few characteristic behaviors exist for droplet ignition compared with premixed gas ignition that has no physical process. One is the fact that the two-stage ignition occurs at ambient temperatures even higher than cool flame temperature. The other is the selectivity of the place of ignition. Both of those are due to the non-homogeneity of the fuel-air mixture around the droplet.

Figure 4-5-6 is an example of how the activity of the reactions depends on temperature and fuel mass fraction. This is a calculated result by using the 12-step reduced model of *n*-heptane [58]. The low-temperature reactions have activity peak around 760 K. The high-temperature reactions play a role above 900 K. The dependence on fuel mass fraction is comparatively less than that on temperature except extremely fuel-lean region. The most

reactive region exists in fuel rich conditions (note that the stoichiometric fuel mass fraction of *n*-heptane is 0.062).

A closer look of the ignition process is possible by overlapping the reactivity distribution and the transient flamelet on temperature-fuel fraction space. An example is shown in Fig. 4-5-7. The reactive region is where reactivity of chemical reaction is higher than dissipation rate. The reactive region becomes wider as time goes on and as dissipation rate decreases. This change is neglected in the succeeding discussions to put more importance on how mixture field is developed with time.

The low-temperature reactions are very active around 760 K and are inhibited above 800 K that is the ceiling temperature. The transient flamelet line goes through the region where the low-temperature reactions are very active. Its activity is higher than any other conditions below 1000 K as is shown in Fig. 4-5-6. The low-temperature reactions at the place of this condition control the cool flame occurrence. The high-temperature reactions have no chance to dominate the process unless ambient temperature is higher than 1000 K. Fuel mass fraction of the most reactive place changes as the process proceeds. A place of fuel lean is the most active at the very beginning. It shifts to the fuel rich places as the surface condition changes. The range of the reactive region relative to the range of the gas phase conditions present around a droplet is very small in terms of temperature range and is very wide for fuel mass fraction. This means that the place where reactions are most active is determined by temperature. A place that has a certain temperature leads ignition process and it is a fuel rich place unless ignition occurs at the very beginning of heat-up period.

The above mechanisms control the process before a cool flame starts. The occurrence of cool flame changes the relation between temperature and fuel mass fraction in gas phase.

The transient flamelet does not take a straight line. The propagating cool flame is shown in Fig. 4-5-8. The succeeding process can be specified to the two cases. One is the case a cool flame causes a hot flame before it spread over widely. Instantaneous cool flame temperature controls the hot flame occurrence. The other case is, on the contrary, a hot flame appears after a widely spread high temperature region is formed by the cool flame. Temperature of the steady cool flame controls the process. Very fuel-rich conditions are favorable to attain higher cool flame temperatures. Initial temperature in gas phase does not have a strong influence on the temperature of the steady cool flame established by propagation. The propagation is driven by the increased temperature at the flame front. The temperature of a propagating cool flame is mainly controlled by the inhibition characteristics of the low-temperature reactions rather than the dynamic behavior. If a pressure condition is given, the only parameter that characterises the inhibition is fuel mass fraction of gas mixture. As is seen in Fig. 4-5-9, the fuel mass fraction that realizes the shortest second induction time, that is a measure of highest cool flame temperature, is 0.2. Change in the second induction time when fuel mass fraction is changed is less at richer side than leaner side. Cool flame temperature seems to be nearly constant for the fuel-rich mixtures. The temperature seems to decrease rapidly, on the contrary, if condition becomes leaner than 0.2 in fuel mass fraction. If cool flame starts from leaner places, it propagates towards droplet with increasing its temperature. A hot flame may happen during this propagation if the temperature becomes high enough. This is the former case. The place of hot flame occurrence depends on the propagation characteristic and can not be defined from the flamelet plot. Dynamic behavior must be taken into account. On the contrary, the place of ignition is easily determined from the plot for the other (the latter)

case. After the propagation pass through the place of the most favorable mixture condition, or if cool flame started from the place, the flame starts decreasing its temperature as propagation proceeds. Instead of the propagation front, a hot flame appears at a place where the cool flame temperature takes maximum. This is due to the fact that the high-temperature reactions are sensitive against temperature more than against fuel fraction. The place of the hot flame occurrence can be determined by looking for a place of a particular fuel mass fraction that realizes highest cool flame temperature. The place of a hot flame occurrence is controlled by fuel mass fraction instead of temperature at the onset of the cool flame. It is in contrast to the case of the cool flame occurrence where temperature determines the place.

Introduction of the transient flamelet supplies how the observed characteristic ignition behaviors come out and the difference between ignition of a droplet and that of homogeneous premixed systems. Reaction development through mixture formation is controlling the process mainly. The relative locations of ambient condition, reactive region and the trajectory of surface condition are the important factor for the phenomena in the droplet ignition process.

5. Induction times

Three different induction times are employed for the analysis of the two-stage ignition process; the first, the second and the total induction time, namely. The definitions of these are equivalent to those of Halstead [32] and the detail for the present case is described in the section 2-4-2. The distinction of the first and the second induction times has not been employed so far for the droplet ignition. The only one that have been researched on are the total induction time (so-called ignition delay, namely). The newly introduced distinction enables a more detailed analyses on the pressure, temperature or droplet size dependence of "ignition delay".

Since *iso*-octane does not produce cool flame and since the process is always single stage, the distinction of the three kinds of induction times is not possible. Only the total induction time is used for this fuel.

The induction times are plotted against ambient temperature for several pressure cases of the three different fuels. The whole set of data can be found in Appendix C; in the figures C-1 to C-21. Droplet life time is also included. Fig. C-1 to 7 are those of *n*-heptane, C-8 to 14 are of *n*-dodecane and C-15 to 21 are of *iso*-octane. Measurements of these induction times are mostly done with the interferometric images stored on 8 mm video tapes. This limits the resolution of these times to 20 msec and the figures show induction times of discrete values.

5-1. The first induction time

The first induction time is required to activate the low-temperature reactions to cause a cool flame. It includes periods for heating the droplet, vaporizing fuel and for mixing fuel and air by diffusion. The first induction time can be determined only for the two normal alkanes. They are shown in Fig. 5-1-1 and Fig. 5-1-2. Only a few pressure cases are plotted to avoid overlapped data. See Appendix C for the data of the other pressure conditions.

5-1-1. Temperature dependency

In all of the pressure conditions for both fuels, the first induction time decreases with ambient temperature. Both chemical and physical processes contribute to this tendency. The activity of the low-temperature reactions increases with temperature unless it exceeds a certain value. The heat-up of a droplet and mixture formation in gas phase are faster at higher temperatures. The higher activity of reactions and The faster mixture formation shorten the induction time.

For the case of *n*-heptane, this induction time can be measured only in the relatively low temperatures (< 800 K) because it becomes too short to be determined at higher temperatures.

The temperature dependency of the first induction time of *n*-dodecane contains more information about the interplay of physical and chemical part. The ceiling temperature of the low-temperature reactions is approximately the cool flame temperature. It is about 750 K as is shown in the ignition region diagrams. The first induction time decreases even at ambient temperatures higher than the ceiling temperature. The temperature of the place that leads the first stage can be below the ceiling temperature even if ambient temperature is above it. The

occurrence of a cool flame is controlled by a place that has a certain temperature at which the low-temperature reactions are most active. This, however, should realize a constant first induction time at any ambient temperature above the ceiling value, because the same gas phase condition of the highest reactivity exists near the droplet irrespective of the ambient. The first induction time includes also heat-up period. It is a time to realize highly reactive mixture conditions. Fuel mass fraction at the droplet surface is extremely low for *n*-dodecane in the initial state of the ignition process. The mixture condition of the highest reactivity does not exist for this moment as is seen also in Fig. 4-5-7. The flamelet line of the initial state exists in the fuel-lean side of the most reactive region. A certain time for heat-up and to shift the line is required. Two factors determine this heat-up period for the present case. One is how quickly the required surface condition is satisfied. A higher ambient temperature realizes a faster rise of the surface temperature because the higher temperature gradient in gas phase promotes heat inflow to the droplet. The other is the requirement of the surface condition (namely, how much temperature and fuel mass fraction are necessary) to have a reactive mixture somewhere in gas phase. The surface fuel mass fraction required for a flamelet line to cross the reactive region becomes smaller as ambient temperature increases as is shown in Fig. 5-1-3 schematically. Both of these two factors yield shorter heat-up periods at higher ambient temperatures. Note that the present heat-up period is different from the definition used for evaporation process that is just determined from a view point of the first one of the two factors. The discussion above can be extended to the regions of arbitrary reactivity, that can be seen in Fig. 4-5-6 as the areas surrounded by iso-reactivity contours. Namely, a higher ambient temperature yields a shorter time to have a certain reactive condition somewhere in gas phase. This principle realizes the general tendency that the first induction time decreases

with increasing ambient temperature.

5-1-2. Pressure dependency

The first induction time has very little dependence on ambient pressure. This trend owes a great part to the characteristic of the low temperature reactions. The theoretical analyses of Keck and Hu [69] showed an induction time inversely proportional to the square of pressure for *n*-heptane premixed gas explosion. The induction time should be slightly shorter at higher pressures from the chemical point of view. The experimental results show this behavior only below 0.5 MPa. For the higher pressures, the first induction time increases with pressure. This is a result of a contradictory influence of physical process. The great part of the induction time is spent for the heating up of the droplet. Higher pressure yields lower fuel fraction at the droplet surface in the initial state because vapor pressure remains constant even when (total) pressure is increased. Although the increased heat inflow to the droplet at higher pressures accelerates the temperature rise at the surface, the time to achieve a certain fuel mass fraction may take longer. The result of Nomura [68] showed longer heat-up periods for high pressures due to the decreased fuel fraction. The increased first induction time is due to the lengthened heat-up of the droplet. In addition, these results are obtained under normal gravity conditions where natural convection influences. The stronger natural convection at higher pressures also tends to lengthen the first induction time. The detail of the influence of natural convection will be discussed in the later section.

5-2. The second induction time

There are two ways how the second induction time exists. One is the case where the low- and the high-temperature reactions interact in the two-stage ignition process. When ambient temperature is lower than the temperature of a cool flame, a hot flame is induced by the cool flame. The second induction time is a time for the cool flame to activate, through its temperature rise, the high-temperature reactions to cause the hot flame. The characteristics of the cool flame control the time. The other case is where these two kinds of reactions act independently. At ambient temperatures higher than the cool flame temperature, the high temperature of the ambient rather than that of a cool flame activates the high-temperature reactions. There is no interaction between the two kinds of reactions through the cool flame. If the low-temperature reactions cause a cool flame before the high-temperature ones cause a hot flame, the phenomenon becomes two-stage ignition. The difference between the times to the appearances of these flames becomes the second induction time.

This induction time is determined only for the two normal alkanes. The second induction times of *n*-heptane and *n*-dodecane for several pressure cases are plotted in Fig. 5-2-1 and 2, respectively.

5-2-1. Temperature dependency

The second induction time of *n*-heptane droplet does not vary for most of the ambient temperatures. On the contrary, those of *n*-dodecane have a peak at an ambient temperature equal to the ceiling temperature for each pressure case.

The second induction times of *n*-heptane at ambient temperatures above the ceiling temperatures are not measured because the first induction times for these conditions are too

short to determine. The second induction times at these temperatures are, though it is not plotted, supposed to decrease with temperature since the total induction time decreases and since the first induction time is negligible short. Hence, the decrease of the second induction time with temperature when ambient temperature is higher than the cool flame temperature is to be a common behavior for these two fuels.

The second induction times at the low temperature ends become infinitesimal for both fuels. Thus, the general trend is that the second induction time increases with increasing temperature while ambient temperature is below the ceiling temperature and it decreases above it. The fact that the second induction time of *n*-heptane does not become longer than a certain value exists in addition to the general trend.

The decrease in the second induction time at ambient temperatures above the cool flame temperature is explained by the low- and the high-temperature reactions that are acting independently. The low- and the high-temperature reactions need induction times to cause a cool and a hot flame respectively. The decrease in the induction time for a hot flame with increasing temperature is more than that for a cool flame. Therefore the second induction time, that is the difference of these induction times, decreases.

The increase in the second induction time with ambient temperature at the lower temperature cases is due to the decreased cool flame temperature. There are two reasons why cool flame temperature decreases with increasing ambient temperature. One is the change in mixture conditions around a droplet at the cool flame occurrence. The first induction time becomes short as ambient temperature increases. This yields a leaner mixture. A leaner mixture tends to yield a shorter second induction time through a lower cool flame temperature as is seen in the Fig. 4-5-9. The other reason is the dynamic behavior of a cool flame. For a

lower ambient temperature, a more amount of chain carriers is required to start a cool flame. The heat release step of the low-temperature reactions does not start until these radicals are pooled enough because the lower temperature tends to reduce the activity of the step. A larger amount of radical pool before the occurrence of a cool flame yields a higher excess temperature as is explained in the section 4-1-2. Thus, cool flame temperature is elevated when ambient temperature is decreased. If a hot flame occurs before the cool flame propagates and forms a steady cool flame, the dynamic behavior of the cool flame controls the induction time. Namely, the dynamics becomes important near the low temperature end of the data where the second induction time becomes infinitesimal short. The second induction time decreases to zero with decreasing ambient temperature.

The qualitative difference that the second induction time of *n*-dodecane increases with ambient temperature while that of *n*-heptane does not exceeds a certain value must be explained from the difference in physical part. The natures of the chemical reactions for the two fuels are almost identical. The difference in the mixture conditions when a cool flame starts is the reason. The gas phase conditions at the moment of cool flame occurrence are shown as the flamelet lines in Fig. 5-2-3. The surface conditions are not measured in the present experiments. Therefore, calculated values are employed for these plots. Evaporation processes are simulated with the present numerical model and the surface condition at the experimentally-measured first induction time is chosen. The conditions for *n*-dodecane are leaner (fuel mass fraction < 0.1) while those of *n*-heptane are very fuel-rich. The cool flame can have possible highest temperature when the gas contains about 20 per cent of *n*-heptane. The value must be a bit higher for *n*-dodecane since its molecular weight is larger while the stoichiometric mole fraction for the highest cool flame temperature must be nearly equal to

that of *n*-heptane. The cool flame temperature decreases as the fuel mass fraction deviates from this value. For the case of *n*-heptane, there exists this condition somewhere in gas phase for all the ambient temperature cases. The gas phase conditions of *n*-dodecane do not have this most favorable condition. The second induction time of *n*-heptane keeps a constant value over ambient temperature because the best condition always exists and controls the induction time irrespective of the ambient. On the contrary, the second induction time of *n*-dodecane increases with temperature because the decreased first induction time with temperature yields leaner mixture conditions that realize lower cool flame temperatures.

5-2-2. Pressure dependency

The second induction time decreases drastically with pressure as is seen from Fig. 5-2-1 and 2. The pressure dependence of the high-temperature reactions contributes the decrease in the second induction time with pressure. The simple model of Westbrook indicates that the global reaction rate of the high-temperature reactions is proportional to the 1.75th power of pressure [25]. This alone does not realize the strong pressure dependence of the observed second induction time. The change in cool flame temperature with pressure explains the drastic decrease. The cool temperature becomes higher as pressure increases as is described in section 4-2-2. The increased cool flame temperature activates the high-temperature reactions more and yields the shorter second induction times at high pressures.

5-3. The total induction time

Since the total induction time is the sum of the first and the second induction time, the characteristics can be explained by combining the former two sections' contexts. Those of *n*-heptane, *n*-dodecane and *iso*-octane are plotted in Fig. 5-3-1, 2 and 3 respectively.

For the *n*-heptane case and at pressure conditions above 0.2 MPa, there are a temperature range where the total induction times are almost independent of ambient temperature (i.e. zero temperature coefficient; ZTC). The constant second induction time in this temperature range realizes this distinctive feature. Independence of the second induction time on ambient temperature appears as the ZTC behavior of the total induction time if the first induction time is negligible short. Droplets of small sizes and of volatile fuel can have the ZTC behavior.

The total induction times of *iso*-octane show a very similar trend as the other two fuels. The increase in pressure drastically reduces the time around 1.0 MPa. The pressure dependence at other pressure ranges seems not to be as much. This similarity in the total induction times of *iso*-octane and the other two fuels implies the hidden roles of the low-temperature reactions. They surely play the similar roles as the other two fuels' cases, though they do not cause any sudden temperature rise like cool flame. The low-temperature reactions of *iso*-octane are less active compared with the other fuels. This yields the longer total induction times.

At high temperatures where no cool flame and hence the first stage occurs, the total induction times show characteristics of the high-temperature reactions. The induction time decreases with ambient temperature since the reactions are more activated with temperature and since the heat-up period is shorter.

5-4. Influence of initial droplet diameter

Initial droplet diameter is the parameter that controls the time scale of the heat-up of a droplet. The initial diameter dependence of the induction times clarifies the importance of the heat-up characteristics.

Figure 5-4-1 shows the first and the total induction times for several initial droplet diameters. Microgravity conditions are used to avoid the influence of natural convection whose strength is diameter dependent. The diameter is varied more than a factor of five. The suspender is not able to hold all of those droplets of different diameters. A suspender without the spherical tip is used for the smallest droplet and porous spheres made of AlO_3 are employed for the large droplets. The amount of fuel fed to the porous spheres is controlled so that the whole surface is in a wet condition. The use of porous spheres does not produce significant differences in the heat-up time scale compared with real droplets, because observed induction times are so short that the properties near the droplet surface alone determine the rate of surface temperature rise. The first induction time of the smallest droplet is not plotted since the reduced size yields a sensitivity of the interferometer too low to detect the temperature inflection properly.

The first induction time varies with initial droplet diameter. It increases as the diameter increases. The heat flux (heat flow per unit surface area) is proportional to the reciprocal of the radius of a surface. A smaller radius realizes a larger heat flux and hence the faster surface temperature rise. Simple evaporation obeys the d-square law. Theoretically and experimentally, it is well proofed that the time required to achieve a certain surface temperature and hence fuel mass fraction is proportional to the square of the initial droplet

diameter [68]. Dimension analysis of these first induction times gives a droplet diameter dependence with a power of 1.4 instead of 2. This slightly smaller value, i.e. a weaker dependence on diameter, means that larger droplets ignite faster than are expected from the surface temperature rise. The surface mass fraction required for the occurrence of the first stage should be lower for larger droplets. Relatively lower reactivity is enough to cause the first stage for larger droplets since the time scale is elongated. To have regions of relatively lower reactivity requires less fuel mass fraction at the surface as is easily derived from the flamelet plots.

The total induction times seem to be on a line parallel to the line of the first induction times. The second induction time is almost independent of the initial droplet diameter. A power of 0.05 is obtained from dimension analysis for the diameter dependence of the second induction time. Since the fuel-air mixture around a droplet is already prepared before the onset of the first stage, no heat-up like period is necessary to cause a hot flame. It is a time for chemical reactions to develop. The slight increase of the second induction time with diameter is due to the lower fuel mass fraction for the larger droplets at the onset of the cool flame. The cool flame temperature is lower for the larger droplets that has leaner mixtures in gas phase. The decreased temperature result in the slight increase in the second induction time.

5-5. Influence of natural convection

Since convection is an important way of heat and mass transfer, the influence is examined. The influence of natural convection is investigated here as an example. Two counteracting

influences exist. One is the increased heat transfer to the droplet that shortens the heat-up period. The other is the increased heat and species transfer from a reactive place that slows down the reaction development. Induction time is shortened if the former influence plays a dominant role and is lengthened if the latter one does. Comparisons between induction times obtained in microgravity and those in normal gravity clarify the influence of natural convection.

The first induction time and the total induction time are plotted against ambient temperature in Fig. 5-5-1 and 2. Microgravity data on these figures are obtained by using the parabolic flights. The detection of the onset of the first or of the second stage for these figures is done with the thermocouple placed at 3 mm distant from the suspender end. The thermocouple detection yields slightly slower response than the interferometer since it is a point measurement that can detect only if the temperature rise comes at where it is placed. A rough comparison between data obtained with the two methods are done and the measurement error of the thermocouple is found to be less than 40 msec in those induction times.

The first induction times at 0.2 MPa under both gravity conditions show agreements at high ambient temperatures. The induction time is lengthened under normal gravity compared with microgravity for lower temperatures. Natural convection lengthens the induction time through the removal of heat and intermediate species of reaction. The reason why the induction times agree at high temperatures can be explained from two viewpoints. One is the strength of convection. Natural convection during the first induction time is downward as is seen in Fig. 4-3-1 and 2. The reduced gas temperature due to the cooling of the droplet and the larger molecular weight of fuel yields higher density compared with ambient. Thus the gas

around the droplet sedimentates. The bulk force to sedimentate is weak at the very beginning of the heat-up period since the gas around the droplet is not cooled widely and since the evaporated fuel is little. Natural convection needs a certain time to develop, in addition. The first stage of a cool flame starts before natural convection becomes strong for the high ambient temperature cases. The weaker convection does not influence the induction times. The other is the amount of convective loss of heat and species relative to that of chemical production. A shorter first induction time indicates a faster chemical reaction. A more convective loss is required to influence the reaction rate compared with the case when chemical reaction is slow. Therefore the influence of convection appears at lower ambient temperatures where convection can be strong and reaction is slow. The difference between both gravity conditions becomes larger as temperature decreases. The more developed convection and the less active reactions at lower temperature yield this trend. A simple modeling can demonstrate this principle. For low ambient temperatures, a droplet ignites after the quasi steady evaporation state is nearly reached. The first induction times for these cases are thought to be proportional to the rate of reactions. Therefore, the mean reaction rate at a given ambient temperature can be approximated as;

$$A / \tau_{mg}$$

where A is constant over temperature and τ_{mg} is induction time without convective loss (i.e. microgravity case). When a constant rate of convective loss 'C' is introduced, the induction time with loss (τ_{ng} , i.e. normal gravity case) can be derived with

$$\tau_{ng} = 1 / (A / \tau_{mg} - C)$$

Rewriting this equation to show the ratio between induction times under normal and microgravity yields;

$$\tau_{ng} / \tau_{mg} = 1 / (A - C * \tau_{mg})$$

This ratio becomes infinity in the limit ($\tau_{mg} \Rightarrow A/C$), that is the low ambient temperature case when the induction time under microgravity becomes longer. The experimental results agree with this rational behavior.

These experiments are conducted to the cool or the hot flame lower limit for these figures. The shown data of lowest temperature for both gravity cases correspond to the temperature of the cool flame lower limit. The shorter first induction time for microgravity guarantees the occurrence of the first stage during droplet life time realizing the lower limiting temperature than normal gravity case.

The total induction times for both gravity conditions agree with each other. The total induction time for the figure's cases is nearly equal to the second induction time since the first induction time is negligible short. Natural convection due to a cool flame exists during the second induction time. This convection is very weak because the temperature of the cool flame is nearly equal to the ambient. The weak convection can not influence the second induction time and hence the total induction time.

The total induction time at 1.0 MPa shows a similar influence as can be seen for the first induction time at 0.2 MPa. The total induction time for this pressure case is nearly equal to the first induction time, the second induction time being negligible short. The influence of natural convection explained for the first induction time of 0.2 MPa appears directly in the difference of total induction times for the two gravity conditions. The influence is stronger since natural convection becomes stronger as pressure increases.

5-6. Simulated result

The current level of understanding on reaction kinetics does not provide a fully quantitative reaction model. The analysis of Kojima [46] showed that even the most-reliable detailed model is not satisfactory. A small error in a reaction rate constant may change the total reaction path. The present simulated results with the systematically reduced model, however, achieve a fair agreement with experiments.

5-6-1. The total induction time of numerical simulation

Calculated total induction times are shown in Fig. 5-6-1.

The model reproduces induction times similar to the experiments except the region where the simulated value jumps. This exists in the temperature range where reaction is switched from the low-temperature ones to the high-temperature ones. The transition from the low-temperature reactions dominant ignition process to the high-temperature one is not reproduced successfully. Temperature dependence of cool flame temperature and hence the second induction time does not agree with experiments. A hot flame occurs immediately after the cool flame occurrence for low ambient temperature cases. Ignition is single-stage for all of these temperatures. An extremely long second induction time is required at ambient temperatures above the switching point.

The calculated hot flame lower limit agrees with experiments as well as the ignition delays of off-intermediate temperature range. The reaction model is useful except reproducing dynamics of the reactions.

5-6-2. *Temperature history*

Figure 5-6-2 shows an example of temperature history for the case of two-stage ignition. A dynamic behavior of a cool flame can be seen. The total induction time can be short if the first temperature rise yields a hot flame. On the contrary, the induction time becomes very long if a hot flame happens after the cool flame temperature settles down to the steady value. The difference between the initial temperature of the cool flame (i.e. the height of the temperature spike at the onset of the cool flame) and the temperature of the steady cool flame seems to be too large. This too strong dynamic behavior also appears as the stronger negative dependence of ignition delay on temperature that is found in Fig. 3-5-2. The decrease in the cool flame temperature when initial temperature is raised is too much for the 12-step model compared with reality. A possible cause of this tendency is an unrealistically high activation energy of the heat release steps. Unrealistically large amount of radical pool is needed to start a cool flame when temperature is low. This yields excess temperature and results in an unrealistically high instantaneous cool flame temperature. A further improvement of the reaction model can be done, for instance, by calibrating the amount of radical pool or of consumed fuel preceding the cool flame occurrence.

5-6-3. *Sensitivity analysis*

The relative importance of transport and of reactions can be estimated by analyzing the sensitivity of the induction times on those parameters. Either doubled or halved rate of heat and mass transport or of reactions is tested. All of binary diffusivities and heat conductivities in gas phase are doubled or halved to change the rate of transport. The same procedure is done for all of the rate coefficients of the elementary reactions to change the reaction

frequency without influencing chemical equilibrium.

The induction times of these cases and sensitivities are listed in Table 3. Transport properties influence the first induction time while reaction rate does little. Doubling the rate of transport almost halves the first induction time. A higher rate of transport shortens the induction time through a faster heat-up of a droplet. The contrary tendency can be seen in the second induction time. More active reactions shorten the second induction time. Increased transport yields longer second induction time. A higher dissipation calms down the development of reactions and lowers the temperature of a cool flame. The decreased cool flame temperature lengthens the second induction time.

The results from the sensitivity analysis show that the first induction time is controlled by physical properties and the second one by chemical reactions

5-7. Discussion

The distinction of the first and the second induction times enables the detailed analyses of the roles of physical and chemical processes. It also uncovers many kinds of influences.

Apart from the heat-up of a droplet, the ignition of a droplet shows distinctive behavior due to the variation of the gas mixture condition around a droplet. The ZTC behavior is a typical of such non-homogeneous systems. Figure 5-7-1 illustrates the relation between ignition of homogeneous and non-homogeneous systems. Since a variety of conditions is coexisting for the non-homogeneous gas mixture, ignition is controlled by the most reactive condition among them and the short-cut of the NTC happens. Two important facts can be

derived from it. One is the fact that imperfection in the homogeneity of a gas mixture may result in a faster ignition occurrence. The other is that what controls ignition delay in the intermediate temperature range is not temperature but pressure. Ignition delay is constant over a temperature difference of more than 100 K. On the other hand, the drastic decrease of the second induction time with pressure yields significant reduction of the total induction time as pressure increases.

Adiabatically compressed fuel-air mixtures have conditions that overlap with the NTC region as is shown in the Fig. 5-7-2. This means that almost all of the high pressure ignition in practice fall into the problems of such intermediate temperature range. The present knowledge for this region provides a clear explanation to the practical problems. Maly [70], for example, report the engine knock occurrence from end-gas near the cylinder wall. The variation of temperature due to the cooling of the wall realizes the non-homogeneity and supplies the best mixture condition for the low-temperature reactions. Pressure plays a role for the occurrence of ignition. The combustion partially happens in a cylinder compresses the unburned mixture. Pressure rise is the most favorable condition to shorten the transition period from cool to hot flame. Avoidance of knock may possible by strongly stirring the mixture in a cylinder to minimize the non-homogeneity and by using an appropriate shape of combustion section not to have any convergent pressure wave that produces high pressures. A similar example is reported by Poeschl et al. [71]. They observed an unwanted ignition in the premixing section of their pre-vaporized-premixed plug flow combustor when mixing is done poorly. Homogeneity of mixture prevents back-fire and widens the safety margin of operations of these combustors.

6. Conclusions

From detailed process analyses on the ignition of isolated fuel droplets, the followings are concluded.

Ignition process of a droplet is specified to the four types. No ignition, cool flame, single- and two-stage ignition, namely. No ignition is the case a droplet evaporates completely before chemical reaction causes a sudden temperature rise. Cool flame is the case a cool flame happens due to the low-temperature reactions and the droplet burns out before the cool flame induces a hot flame. A hot flame appears during droplet life time for single- and two-stage ignition. Single-stage ignition is specified to two types. One is the low-temperature reactions dominant ignition. That is, the low-temperature reactions cause a cool flame and its temperature rise activates the high-temperature reactions causing a hot flame right after the occurrence of the cool flame. It is a special case of two-stage ignition with an infinitesimal short cool flame duration. Another is the high-temperature reactions dominant. When ambient temperature is very high, the low-temperature reactions do not play any role on heat release. The high-temperature reactions are activated by the high temperature of ambient and cause a hot flame. Cool flame does not happen for this type.

The types of ignition and its ambient condition dependence are controlled by the reaction characteristics of the employed fuel. The ignition regions are almost the same as those reported from the ignition of premixed gases. The difference is that the cool flame and the two-stage ignition process happens for droplet ignition even at ambient temperatures higher than the ceiling temperature of the low-temperature reactions. The variation in the gas-phase

conditions around the droplet gives chances for a cool flame to appear in such high ambient temperatures.

Ignition process proceeds in several steps. Two-stage ignition has all of these typical steps. A droplet suddenly exposed to a hot ambient is heated up by the gas and raises its temperature. The increased temperature yields an increase in fuel mass fraction at the surface. Thus, the mixture conditions changes from fuel-lean to fuel-rich as time goes on. The low-temperature reactions prefer a particular temperature. When a place of this temperature get enough fuel, the reactions are activated and a cool flame occurs. Temperature in gas-phase increases widely and a fuel-rich place realizes the highest temperature. The high-temperature reactions are activated by temperature and a hot flame firstly appears at the place of the highest temperature. The flame propagates consuming partially premixed reactants and finally a diffusion flame is formed about the droplet. In these steps, the place of the cool flame occurrence is controlled by the temperature and that of the hot flame occurrence is by fuel mass fraction.

To characterise the time to each event, the first, the second and the total induction times are introduced. The first induction time is the time to have a cool flame after a droplet is brought into a hot ambient. The second induction time is the duration of a cool flame. The total induction time is the time to the hot flame occurrence. The first induction time is controlled by the heat-up characteristics of a droplet. It is a time to realize a certain fuel mass fraction at the place of a certain temperature. If the low-temperature reactions require less fuel to become active, or if high fuel mass fraction can be achieved sooner by a higher vapor pressure, the time is decreased. A higher ambient temperature, a higher volatility of the fuel or a smaller droplet diameter realizes a shorter first induction time. The second induction time is

controlled by the gas phase conditions at the onset of a cool flame. The temperature of a cool flame controls the activity of the high-temperature reactions and hence the second induction time. If very fuel-rich conditions exist when a cool flame starts, the cool flame temperature can take the possible maximum and a particular value of the second induction time is obtained irrespective of ambient conditions. If a cool flame starts before rich mixture is achieved, the cool flame temperature depends on the stoichiometry of the mixture. The leaner conditions yield the longer second induction time. Thus, a rapidly vaporizing droplet has a constant second induction time over ambient temperature while a slowly vaporizing droplet does not. Ambient temperature has no influence on the second induction time of volatile fuel or a droplet of small diameter. Since the cool flame temperature has a strong dependence on pressure due to the equilibrium characteristics of the inhibition step in their chain, pressure is the dominant parameter for the second induction time. An increase in ambient pressure dramatically reduces the induction time.

The first induction time is mainly controlled by the physical characteristics of fuel while the second one is by the characteristics of chemical reaction.

The total induction time can be quantified and qualified by summing the first and the second induction times.

Nomenclatures

C_p	heat capacity
D_{ij}	binary diffusivity of i th species in j th species
f_i	fugacity of i th species
h	absolute enthalpy
k_{ij}	correlation factor of Peng-Robinson equation of state
L	latent heat
M	molecular weight
P	pressure
q_T	conductive heat flux
r	radial coordinate
R	gas constant
R	regression rate of droplet radius
t	time
T	temperature
v	velocity
V	critical volume
V_i	diffusive velocity of i th species
w_i	chemical mass production rate of i th species
X_i	mole fraction of i th species
Y_i	massfraction of i th species
Z	compression factor
ϕ	fugacity coefficient
λ	heat conductivity
ρ	density
σ	12-6 Lennard-Jones potential parameter
ω	acentric factor
Ω	collision integral

sub- and superscript

c	critical state
ex	excess value
g	gas phase
i, j, k	i, j, k th species
l	liquid phase
m	mean value
r	reduced value
R^+	gas side of liquid-gas interface
R^-	liquid side of liquid-gas interface
tr	translational
0	reference state

Acknowledgement

I would like to express my sincerest appreciation to Professor Michikata Kono, at the University of Tokyo, who is the supervisor throughout this study and the chief referee of the thesis.

I would express my sincere thanks also to the Professors Yoshihiro Arakawa, Toshio Nagashima, Toshisuke Hirano and Hiroyuki Matsui, the co-referees, all at the University of Tokyo, for usefull discussions and revisions.

This study is supported by various organizations and foundations. The most part of the study is done in cooperation with ZARM (Center of Applied Space Technology and Microgravity), the University of Bremen, Germany. Special thanks to Professor Hans J. Rath, the head of the institute, and to Mr. Christian Eigenbrod, Mr. Jens Koenig, Mr. Gunther Marks and the other members of the combustion department of the institute. The cooperation is supported by the Special Coordination Fund for Promoting Science and Technology through the STA in Japan and by a grant from the DARA in Germany.

I have got very useful help and supports from many researchers for this study. I would like to appreciate Dr. Jun'ichi Sato at Ishikawajima-Harima Heavy Industry for his useful advices and guidance. Many thanks to Professor Norbert Peters and Dr. Heinz Pitsch, at RWTH Aachen, Germany, for their kind support for the chemical reaction model. Heartfelt thanks to Dr. Friedlich Dinkelacker, at the University of Erlangen-Nurnberg, Germany, and to Dr. Masato Mikami, at Yamaguchi University, for very useful discussions.

I would express my sincere gratitude to all the persons in the labor at the University of Tokyo; expecially to Mrs. Sayako Hebiguchi, Mr. Yoshiyuki Wada, Mr. Masafumi Utsumi, Mr. Naohiro Sato, Mr. Hideki Kato, Mr. Shuhei Takahashi and Mr. Osamu Moriue who have helped and supported to make this study from all aspects.

References

1. Law, C. K. and Faeth, G. M. (1994). Opportunities and Challenges of Combustion in Microgravity. *Progress in Energy and Combustion Science*, 20, 65-113.
2. Faeth, G. M. and Olson, D. R. (1968). The Ignition of Hydrocarbon Fuel in Air. SAE TR-680465, 77, 1793-1802.
3. Faeth, G. M., Karahan, B. L. and Yanyecic, G. A. (1968). Ignition and Combustion of Monopropellant Droplets. *AIAA Journal*, 6-4, 684-689.
4. Law, C. K. (1975). Asymptotic Theory for Ignition and Extinction in Droplet Burning. *Combustion and Flame* 24, 89-98.
5. Law, C. K. (1978). Theory of Thermal Ignition in Fuel Droplet Burning. *Combustion and Flame*, 31, 285-296.
6. Law, C. K. and Chung, S. H. (1980). An Ignition Criterion for Droplets in Sprays. *Combustion Science and Technology*, 22, 17-26.
7. Chao, B. H., Matalon, M. and Law, C. K. (1985). Gas-Phase Transient Diffusion in Droplet Ignition. *Combustion and Flame*, 59, 43-51.
8. Bryant, J. T. (1975). Ignition Delay Time of Fuel Droplets, an Empirical Correlation with Flash Point. Short Communication, *Combustion Science and Technology*, 10, 185-187.
9. Saitoh, T., Ishigro, S. and Nioka, T. (1982). An Experimental Study of Droplet Ignition Characteristics Near the Ignitable Limit. *Combustion and Flame*, 48, 27-32.
10. Nakanishi, R., Kobayashi, H., Kato, S. and Nioka, T. (1994). Ignition Experiment of a Fuel Droplet in High-Pressure High-Temperature Ambient. Twenty-Fifth Symposium (International) on Combustion, The Combustion Institute, 447-453.
11. Peskin, R. L., Polymeropoulos, C. E. and Yeh, P. S. (1967). Results from a Theoretical Study of Fuel Drop Ignition and Extinction. *AIAA Journal*, 5-12, 2173-2178.
12. Wood, B. J. and Rosser Jr. W. A. (1969). An Experimental Study of Fuel Droplet Ignition. *AIAA Journal*, 7-12, 2288-2292.
13. Sangiovanni, J. J. and Kesten, A. S. (1977). A Theoretical and Experimental Investigation of the Ignition of Fuel Droplets. *Combustion Science and Technology*, 16, 59-70.
14. Bergeron, C. A. and Hallett, W. L. H. (1989). Ignition Characteristics of Liquid Hydrocarbon Fuels as Single Droplets. *The Canadian Journal of Chemical Engineering*, 67, 142-149.
15. Takei, M., Kobayashi, H. and Nioka, T. (1993). Ignition Experiment of a Blended-fuel Droplet in a Microgravity Field. *Microgravity Science and Technology*, VI/3, 184-187.
16. Ristau, R., Nagel, U., Iglseeder, H., König, J., Rath, H. J., Nomura, H., Kono, M., Tanabe, M. and Sato, J. (1993). Theoretical and Experimental Investigations on Droplet Evaporation and Droplet Ignition at High Pressures. *Microgravity Science and Technology*, VI/4, 223-228.

17. Niioka, T., Ishiguro, S. and Saitoh, T. (1980). A Numerical Approach to Fuel Droplet Ignition. Technical Report of National Aerospace Laboratory, TR-628-T.
18. Ruzsalo, R. and Hallett, W. L. H. (1992). A Model for the Autoignition of Single Liquid Droplets at High Pressures. *Combustion Science and Technology*, 86, 183-197.
19. Tsukamoto, T. Okada, H. and Niioka, T. (1993). Ignition Simulation of a Fuel Droplet in High-Pressure High-Temperature Atmosphere. *Transaction of Japan Soc. Aero. Space Sci.*, 35-110, 165-176.
20. Tsai, G.-T. and Yang, J.-T. (1994). Numerical Analysis of Convective Ignition and Flame Development over a Porous Sphere. *Combustion Science and Technology*, 96, 1-21.
21. Bergeron, C. A. and Hallett, W. L. H. (1989). Autoignition of Single Droplets of Two-Component Liquid Fuels. *Combustion Science and Technology*, 65, 181-194.
22. Dwyer, H. A. and Le, D. P. (1993). Numerical Experiments on Fuel Droplet Vaporization and Ignition. 31st Aerospace Sciences Meeting and Exhibit, AIAA 93-0905.
23. Shaygan, N. and Prakash, S. (1995). Droplet Ignition and Combustion Including Liquid-Phase Heating. *Combustion and Flame*, 102, 1-10.
24. Westbrook, C. K. and Dryer, F. L. (1981). Simplified Reaction Mechanisms for the Oxidation of Hydrocarbon Fuels in Flames. *Combustion Science and Technology*, 27, 31-43.
25. Westbrook, C. K. and Dryer, F. L. (1984). Chemical Kinetic Modeling of Hydrocarbon Combustion. *Progress in Energy and Combustion Science*, 10, 1-57.
26. Townene, D. T. A. (1948). Ignition Regions of Hydrocarbons. Second Symposium (International) on Combustion, The Combustion Institute, 134-145.
27. Lincquin, M. and Laffitte, P. (1956). Cool Flames of Pentane-Oxygen Mixtures. Sixth Symposium (International) on Combustion, The Combustion Institute, 130-134.
28. Bonner, B. H. and Tipper, F. H. (1965). Cool-Flame Combustion of Hydrocarbons. Tenth Symposium (International) on Combustion, The Combustion Institute, 145-150.
29. Hoare, D. E., Li, T. M. and Walsh, A. D. (1966). Cool Flames and Molecular Structure. Eleventh Symposium (International) on Combustion, The Combustion Institute, 879-887.
30. Barnard, J. A. and Watts, A. (1972). The Relationship between Slow Reaction and Cool Flames in Combustion Process. *Combustion Science and Technology*, 6, 125-131.
31. Barnard, J. A. and Lee, R. K. Y. (1972). The Combustion of *n*-Pentane in a Shock Tube. *Combustion Science and Technology*, 6, 143-150.
32. Halstead, M. P., Kirsch, L. J., Prothero, A. and Quinn, C. P. (1975). A Mathematical Model for Hydrocarbon Autoignition at High Pressures. *Proceedings of the Royal Society in London*, A-346, 515-538.
33. Harstead, M. P., Kirsch, L. J. and Quinn, C. P. (1977). The Autoignition of Hydrocarbon Fuels at High Temperatures and Pressures - Fitting of a Mathematical Model. *Combustion and Flame*, 30, 45-60.

34. Morley, C. (1988). Photolytic Perturbation Method to Investigate the Kinetics of Hydrocarbon Oxidation near 800 K. Twenty-Second Symposium (International) on Combustion, The Combustion Institute, 911-918.
35. Lignola, P. G., DI Maio, F. P., Marzocchella, A. and Mercogliano, R. (1988). JSFR Combustion Processes of *n*-Heptane and Isooctane. Twenty-Second Symposium (International) on Combustion, The Combustion Institute, 1625-1633.
36. Carlier, M., Corre, C., Minetti, R., Pauwels, J-F., Ribaucour, M. and Sochet, L-R. (1990). Autoignition of Butane: A Burner and a Rapid Compression Machine Study. Twenty-Third Symposium (International) on Combustion, The Combustion Institute, 1753-1758.
37. D'anna, A, Mercogliano, R. Barbella, R. and Ciajolo A. (1992). Low Temperatur Oxidation Chemistry of *iso*-Octane under High Pressure Conditions. Combustion Science and Technology, 83, 217-232.
38. Blin-Simiand, N., Rigny, R., Viossat, V., Circan, S. and Sahetchian, K. (1993). Autoignition of Hydrocarbon/Air Mixtures in a CFR Engine: Experimental and Modeling Study. Combustion Science and Technology, 88, 329-348.
39. Cavaliere, A., Ciajolo, A., D'anna, A., Mercogliano, R. and Ragucci, R. (1993). Autoignition of *n*-Heptane and *n*-Tetradecane in Engine-like Conditions. Combustion and Flame, 93, 279-286.
40. Dagaut, P., Reuillon, M., Boettner, J.-C. and Cathonnet, M. (1994). Kerosene Combustion at Pressures up to 40 atm: Experimental Study and Detailed Chemical Kinetic Modeling. Twenty-Fifth Symposium (International) on Combustion, The Combustion Institute, 919-926.
41. Benson, S. W. (1986). Combustion, a Chemical and Kinetic View. Twenty-First Symposium (International) on Combustion, The Combustion Institute, 703-711.
42. Lignola, P. G. and Reverchon, E. (1987). Cool Flames. Progress in Energy and Combustion Science, 13, 75-96.
43. Westbrook, C. K., Warnatz, J. and Pitz, W. J. (1988). A Detailed Chemical Kinetic Reaction Mechanism for the Oxidation of *iso*-Octane and *n*-Heptane over an Extended Temperature Range and its Application to Analysis of Engine Knock. Twenty-Second Symposium (International) on Combustion, The Combustion Institute, 893-901.
44. Cowart, J. S., Keck, J. C., Heywood, J. B., Westbrook, C. K. and Pitz, W. J. (1990). Engine Knock Predictions Using a Fully-Detailed and a Reduced Chemical Kinetic Mechanism. Twenty-Third Symposium (International) on Combustion, The Combustion Institute, 1055-1062.
45. Chevalier, C., Pitz, W. J., Warnatz, J., Westbrook, C. K. and Melenk, H. (1992). Hydrocarbon Ignition: Automatic Generation of Reaction Mechanisms and Applications to Modeling of Engine Knock. Twenty-Fourth Symposium (International) on Combustion, The Combustion Institute, 93-101.
46. Kojima, S. (1994). Detailed Modeling of *n*-Butane Autoignition Chemistry. Combustion and Flame, 99, 87-136.

47. Ranzi, E., Sogaro, A., Gaffuri, P., Pennati, G., Westbrook, C. K. and Pitz, W. J. (1994). A New Comprehensive Reaction Mechanism for Combustion of Hydrocarbon Fuels. *Combustion and Flame*, 99, 201.
48. Griffiths, J. F., Hughes, K. J. Schreiber, M. and Poppe, C. (1994). A Unified Approach to the Reduced Kinetic Modeling of Alkane Combustion. *Combustion and Flame*, 99, 533.
49. Ranzi, E., Faravelli, T., Gaffuri, P. and Sogaro, A. (1995). Low-Temperature Combustion: Automatic Generation of Primary Oxidation Reactions and Lumping Procedures. *Combustion and Flame*, 102, 179-192.
50. Ranzi, E., Gaffuri, P. and Faravelli, T. (1995). A Wide-Range Modeling Study of *n*-Heptane Oxidation. *Combustion and Flame*, 103, 91-106.
51. Griffiths, J. F., Jiao, Q., Shreiber, M., Meyer, J. and Knoche, K. F. (1992). Development of Thermokinetic Models for Autoignition in a CFD Code: Experimental Validation and Application of the Results to Rapid Compression Studies. Twenty-Fourth Symposium (International) on Combustion, The Combustion Institute, 1809-1815.
52. Griffiths, J. F. (1993). Kinetic Fundamentals of Alkane Autoignition at Low Temperatures. Brief Communication, *Combustion and Flame*, 93, 202-206.
53. Schreiber, M., Sadat Sakak, A., Lings, A. and Griffiths, J. F. (1995). A Reduced Thermokinetic Model for the Autoignition of Fuels with Variable Octane-Ratings. Twenty-Fifth Symposium (International) on Combustion, The Combustion Institute, 933-940.
54. Griffiths, J. F. (1995). Reduced Kinetic Models and Their Application to Practical Combustion Systems. *Progress in Energy and Combustion Science*, 21, 25-107.
55. Peters, N. and Rogg, B. (1993). *Reduced Kinetic Mechanisms for Applications in Combustion Systems*. Springer-Verlag.
56. Müller, U. C., Peters, N. and Linan, A. (1992). Global Kinetics for *n*-Heptane Ignition at High Pressures. Twenty-Fourth Symposium (International) on Combustion, The Combustion Institute, 777-784.
57. Müller, U. Ch. (1993). *Reduziert Reaktionsmechanismen für die Zündung von n-Heptan und iso-Octan unter Motorrelevanten Bedingungen*. Dissertation, Institute für Technische Mechanik der RWTH Aachen.
58. Pitsch, H. and Peters, N. (1994). personal communication, RWTH Aachen, Germany.
59. Shih, A.T. and Megaridis, C. M. (1995). Suspended Droplet Evaporation Modeling in a Laminar Convective Environment. *Combustion and Flame*, 102, 256-270.
60. Heitor, M. V. and Moreira, A. L. N. (1993). Thermocouples and Sample Probes for Combustion. *Progress in Energy and Combustion Science*, 19, 259-278.
61. Reid, R. C., Prausnitz, J. M. and Poling, B. E. (1988). *The Properties of Gases and Liquids*, Fourth Edition. McGraw-Hill, Inc., New York.

62. Oran, E. S. and Boris, J. P. (1981). Detailed Modeling of Combustion Systems. *Progress in Energy and Combustion Science*, 7, 1-72.
63. Coffee, T. P. and HeimeI, J.M. (1981). *Combustion and Flame*, 43, 273-.
64. Stoer, J. and Bulirsch, R. (1992). *Introduction to Numerical Analysis, Second Edition*. Springer-Verlag, New York.
65. Ciezki, H. K. and Adomeit, G. (1993). Shock-Tube Investigation of Self-Ignition of *n*-Heptane-Air Mixtures Under Engine Relevant Conditions. *Combustion and Flame*, 93, 421-433.
66. Griffiths, J. F. and Scott, S. K. (1987). Thermokinetic Interactions: Fundamentals of Spontaneous Ignition and Cool Flames. *Progress in Energy and Combustion Science*, 13, 161-197.
67. Ranz, W. E. and Marshall Jr., W. R. (1952). Evaporation from Drops. Part I and Part II. *Chemical Engineering Progress*, 48-3, 141-146 and 173-180.
68. Nomura, H. (1993). dissertation, University of Tokyo, Japan.
69. Keck, J. C. and Hu, H. (1986). Explosions of Adiabatically Compressed Gases in a Constant Volume Bomb. Twenty-fifth Symposium (International) on Combustion, The Combustion Institute, 521-529.
70. Maly, R. (1994). State of the Art and Future Needs in S. I. Engine combustion. Twenty-fifth Symposium (International) on Combustion, The Combustion Institute, 111-124.
71. Poeschl, G., Ruhkamp, W. and Pfost, H. (1994). Combustion with Low Pollutant Emissions of Liquid Fuels in Gas Turbines by Premixing and Prevaporization. ASME 94-GT-443.

Table 1. Properties of fuels

	<i>n</i> -heptane	<i>n</i> -dodecane	<i>iso</i> -octane
molecular weight [g/mol]	100.2	170.3	114.2
critical temperature [K]	540.2	658.3	566.4
critical pressure [MPa]	2.74	1.80	2.73
normal boiling point [K]	371.6	489.5	386.6
liquid density [g/cm ³]	0.684	0.748	0.719

Table 2. reaction steps of Pitsch's model
(R: C₇H₁₆, Q: C₇H₁₄)

	reaction step
1a	$n\text{-C}_7\text{H}_{16} = \text{C}_3\text{H}_6 + 2 \text{C}_2\text{H}_4 + \text{H}_2$
1b	$n\text{-C}_7\text{H}_{16} + \text{O}_2 + \text{OH} = \text{RO}_2 + \text{H}_2\text{O}$
2	$\text{RO}_2 + \text{O}_2 = \text{OH} + \text{OQOOH}$
3	$\text{OQOOH} = 2 \text{C}_2\text{H}_4 + \text{CH}_2\text{O} + \text{CH}_3 + \text{CO} + \text{OH}$
4	$\text{C}_3\text{H}_6 + \text{H}_2\text{O} = \text{C}_2\text{H}_4 + \text{CH}_2\text{O} + \text{H}_2$
5	$\text{C}_2\text{H}_4 + \text{O}_2 = 2 \text{CO} + 2 \text{H}_2$
6	$\text{CH}_2\text{O} = \text{CO} + \text{H}_2$
7	$\text{CH}_3 + \text{OH} = \text{CH}_2\text{O} + \text{H}_2$
8	$2 \text{HO}_2 = \text{O}_2 + \text{H}_2\text{O}_2$
9	$\text{H}_2\text{O}_2 = 2 \text{OH}$
10	$\text{CO} + \text{H}_2\text{O} = \text{CO}_2 + \text{H}_2$
11	$\text{O}_2 + \text{H}_2 = 2 \text{OH}$
12	$2 \text{OH} + \text{H}_2 = 2 \text{H}_2\text{O}$

Table 3. Sensitivities on transport properties and reaction rate coefficients
 12-step model, ambient condition; 0.5 MPa, 780 K, initial droplet diameter; 0.7 mm
 (the value of sensitivity is defined as a power by which induction times depends on these parameters)

	first induction time [msec]	sensitivity of first induction time	second induction time [msec]	sensitivity of second induction time
original	61.54	-	255.4	-
transport $\times 2$	28.04	1.13	377.9	-0.565
transport $\times 0.5$	143.0	1.22	208.3	-0.294
reaction $\times 2$	49.23	0.322	102.5	1.32
reaction $\times 0.5$	79.83	0.375	723.5	1.50

Figures

- 2-1-1. a schematic of the experimental setup
- 2-1-2. suspender configuration
- 2-1-3. temperature rise that a droplet undergo at insertion to the furnace
- 2-1-4. fuel pump system
- 2-1-5. gas supply system
- 2-2-1. Bremen droptower
- 2-2-2. gravity level during free-fall in droptower
- 2-2-3. Caravelle twin jet used for parabolic flights
- 2-2-4. flight profile of parabolic flight
- 2-2-5. gravity level during parabola
- 3-4-1. a schematic illustration of Griffiths' 10-reaction model
- 3-5-1. squared diameter history for the case of evaporation, a comparism between experimental resuslts and simulation
- 3-5-2. ignition delay over temperature, a comparism between shock-tube experiment and simulations
- 4-1-1. sequential images of phase shift distribution obtained by the interferometer, false color
- 4-1-2. estimated temperature field variation with time
- 4-2-1. ignition regions and characteristic temperatures of *n*-heptane droplet
- 4-2-2. ignition regions and characteristic temperatures of *n*-dodecane droplet
- 4-2-3. ignition regions and characteristic temperatures of *iso*-octane droplet
- 4-3-1. sequential images of interferometric fringes, cool flame under normal gravity
- 4-3-2. sequential images of interferometric fringes, two-stage process under normal gravity
- 4-3-3. sequential images of interferometric fringes, single-stage process under normal gravity
- 4-3-4. sequential images of interferometric fringes, low ambient temperature case, under microgravity
- 4-3-5. sequential images of interferometric fringes, middle ambient temperature case, under microgravity
- 4-3-6. sequential images of interferometric fringes, high ambient temperature case, under microgravity
- 4-4-1. simulated two step tpreature rise with 10-reacton model
- 4-4-2. heat release history, the time varying activity of the low- and the high-temperature reaction
- 4-4-3. variation of temperature profiles with time up to the diffusion flame formation, ambient temperature of below NTC region
- 4-4-4. variation of temperature profiles with time up to the diffusion flame formation, ambient temperature of in NTC region
- 4-5-1. transient process of mixture formation, surface temperature rise and the movement of the flamelet line on temperature-fuel mass fraction plane
- 4-5-2. temperature change at a place of stoichiometry during evalopration, simulation
- 4-5-3. mixture reactivity history at a place of stoichiometry, simulation

- 4-5-4. temporal decay of dissipation rate at a place of stoichiometry, simulation
- 4-5-5. Damköhler number history
- 4-5-6. mixture reactivity
- 4-5-7. transient flamelet and reactivity change with time, before the onset of a cool flame
- 4-5-8. transient flamelet during the first stage
- 4-5-9. fuel mass fraction dependence of the second induction time
- 5-1-1. the first induction time against ambient temperature for a few pressure cases, *n*-heptane
- 5-1-2. the first induction time against ambient temperature for a few pressure cases, *n*-dodecane
- 5-1-3. geometric derivation of required surface condition
- 5-2-1. the second induction time against ambient temperature for a few pressure cases, *n*-heptane
- 5-2-2. the second induction time against ambient temperature for a few pressure cases, *n*-dodecane
- 5-2-3. gas phase conditions at the onset of the first stage
- 5-3-1. the total induction time against ambient temperature for a few pressure cases, *n*-heptane
- 5-3-2. the total induction time against ambient temperature for a few pressure cases, *n*-dodecane
- 5-3-3. the total induction time against ambient temperature for a few pressure cases, *iso*-octane
- 5-4-1. variation in the induction times with initial droplet diameter
- 5-5-1. comparisons of induction times under normal- and microgravity, 0.2 MPa
- 5-5-2. comparisons of the total induction times under normal- and microgravity, 0.2 MPa
- 5-6-1. comparisons of ignition delay, experiments and simulation
- 5-6-2. typical calculated temperature history
- 5-7-1. NTC of homogeneous premixed gas ignition and ZTC of non-homogeneous ignition
- 5-7-2. conditions of adiabatically compressed gases

Appendix A. Numerical reconstruction of temperature field with an assumption of axis symmetry.

Axis symmetric temperature field and the fringe count of the interferometer are correlated by the following equations in general through refractive index that is a function of gas density.

Equation of state:
$$P = \rho RT \Leftrightarrow \frac{T}{T_a} = \frac{\rho_a}{\rho} \text{ for constant } P$$

Gladstone-Dale relation:
$$\Delta n = n - n_a = k(\rho - \rho_a)$$

and an integration through a concentric distribution of refractive index:

$$N(y) = \frac{4}{\lambda} \int_{r=y}^{\infty} [n(r) - n_{\infty}] dl = \frac{4}{\lambda} \int_{r=y}^{\infty} [n(r) - n_{\infty}] \frac{r}{\sqrt{r^2 - y^2}} dr$$

In the first equation, 'P' is pressure, 'ρ' is density, 'R' is gas constant and 'T' is temperature. The subscript 'a' denotes ambient or a reference state. In the second equation, 'n' is refractive index and 'k' is the Gladstone constant that is unique to the component of gas. The 'N' in the third equation is the fringe counts as a function of radial coordinate 'y' that has its origin at the center of the axis of symmetry. This is obtained from the interferometric images. The 'λ' is the wave length of light beam, 'r' is a variable indicating radial distance, and 'l' is a coordinate in the direction parallel to the object light beam.

For a numerical solution, the above equation is rewritten as follows:

$$N(y_i) = \frac{4}{\lambda} \sum_{k=i}^a \Delta n(y_k) dl_{i,k}$$

in another form,

$$[N(y_1) \cdots N(y_a)] = \frac{4}{\lambda} \cdot \begin{bmatrix} dl_{1,1} & dl_{1,2} & \cdots & dl_{1,a} \\ & dl_{2,2} & & \vdots \\ & & \ddots & \vdots \\ 0 & & & dl_{a,a} \end{bmatrix} \cdot \begin{bmatrix} \Delta n(y_1) \\ \vdots \\ \vdots \\ \Delta n(y_a) \end{bmatrix}$$

here, $\Delta n(y_k) = n(y_k) - n(y_a)$,

$$n(y) = n(y_a) = n_\infty \text{ at } y \geq y_a$$

$$dl_{i,k} = \frac{1}{2} \left(\sqrt{y_{k+1}^2 - y_i^2} - \sqrt{y_{k-1}^2 - y_i^2} \right) \quad (k \neq i)$$

$$\frac{1}{2} \sqrt{y_{k+1}^2 - y_i^2} \quad (k = i)$$

Since 'N' and 'dl' are known, Δn can be derived explicitly. After the refractive index distribution is solved, it is transformed into temperature distribution through the aforementioned Gladstone-Dale relation and the equation of state.

Appendix B. Considered reactions in 12 step model of Pitsch and Peters.

- | | |
|--|---|
| 1. $H + O_2 \rightarrow O + OH$ | 34. $CH_4 + OH \rightarrow CH_3 + H_2O$ |
| 2. $O + OH \rightarrow H + O_2$ | 35. $C_2H_2 + O \rightarrow CH_2 + CO$ |
| 3. $H_2 + OH \rightarrow H + H_2O$ | 36. $C_2H_3 \rightarrow C_2H_2 + H$ |
| 4. $H + H_2O \rightarrow H_2 + OH$ | 37. $C_2H_3 + O_2 \rightarrow C_2H_2 + H$ |
| 5. $OH + OH \rightarrow O + H_2O$ | 38. $C_2H_3 + O_2 \rightarrow CHO + CH_2O$ |
| 6. $O + H_2O \rightarrow OH + OH$ | 39. $C_2H_4 + OH \rightarrow C_2H_3 + H_2O$ |
| 7. $H + H + M \rightarrow H_2O$ | 40. $C_2H_4 + H \rightarrow C_2H_3 + H_2$ |
| 8. $H_2O + M \rightarrow H + OH$ | 41. $C_2H_5 \rightarrow H + C_2H_4$ |
| 9. $H + O_2 + M \rightarrow HO_2$ | 42. $C_2H_5 + O_2 \rightarrow C_2H_4 + HO_2$ |
| 10. $H + HO_2 \rightarrow OH + OH$ | 43. $C_2H_6 + H \rightarrow C_2H_5 + H_2$ |
| 11. $HO_2 + OH \rightarrow H_2O + O_2$ | 44. $C_3H_6 + OH \rightarrow C_2H_5 + CH_2O$ |
| 12. $HO_2 + HO_2 \rightarrow H_2O_2 + O_2$ | 45. $C_3H_7 \rightarrow C_2H_4 + CH_3$ |
| 13. $H_2O_2 + M \rightarrow OH + OH$ | 46. $C_3H_7 + O_2 \rightarrow C_3H_6 + HO_2$ |
| 14. $OH + OH + M \rightarrow H_2O_2$ | 47. $C_4H_9 \rightarrow C_2H_5 + C_2H_4$ |
| 15. $CO + OH \rightarrow H + CO_2$ | 48. $C_5H_{11} \rightarrow C_3H_7 + C_2H_4$ |
| 16. $CO_2 + H \rightarrow OH + CO$ | 49. $C_7H_{15} \rightarrow C_5H_{11} + C_2H_4$ |
| 17. $CH + CO_2 \rightarrow CHO + CO$ | 50. $C_7H_{15} \rightarrow C_4H_9 + C_3H_6$ |
| 18. $CH + H_2O \rightarrow CH_2 + OH$ | 51. $C_7H_{16} \rightarrow C_3H_7 + C_4H_9$ |
| 19. $CHO + M \rightarrow H + CO$ | 52. $C_7H_{16} + H \rightarrow C_7H_{15} + H_2$ |
| 20. $CHO + H \rightarrow H_2 + CO$ | 53. $C_7H_{16} + OH \rightarrow C_7H_{15} + H_2O$ |
| 21. $CHO + OH \rightarrow H_2O + CO$ | 54. $C_7H_{16} + HO_2 \rightarrow C_7H_{15} + H_2O_2$ |
| 22. $CH_2 + H \rightarrow CH + H_2$ | 55. $C_7H_{16} + O_2 \rightarrow C_7H_{15} + O_2$ |
| 23. $CH_2 + O_2 \rightarrow CO + OH + H$ | 56. $C_7H_{15} + O_2 \rightarrow C_7H_{15}O_2$ |
| 24. $CH_2 + H_2 \rightarrow CH_3 + H$ | 57. $C_7H_{15}O_2 \rightarrow C_7H_{15} + O_2$ |
| 25. $CH_2O + OH \rightarrow CHO + H_2O$ | 58. $C_7H_{15}O_2 \rightarrow C_7H_{14}OOH$ |
| 26. $CH_3 + O \rightarrow H + CH_2O$ | 59. $C_7H_{14}OOH \rightarrow C_7H_{15}O_2$ |
| 27. $CH_3 + O_2 \rightarrow CH_2O + OH$ | 60. $C_7H_{14}OOH + O_2 \rightarrow O_2C_7H_{14}OOH$ |
| 28. $CH_3 + HO_2 \rightarrow CH_3O + OH$ | 61. $O_2C_7H_{15}OOH \rightarrow HOOC_7H_{13}OOH$ |
| 29. $CH_3 + H \rightarrow CH_4$ | 62. $HOOC_7H_{13}OOH \rightarrow OC_7H_{13}OOH + OH$ |
| 30. $CH_3 + CH_3 \rightarrow C_2H_4 + H_2$ | 63. $OC_7H_{13}OOH \rightarrow OC_7H_{13}O + OH$ |
| 31. $CH_3 + CH_3 \rightarrow C_2H_6$ | 64. $OC_7H_{13}O \rightarrow 1C_5H_{11} + CH_2O + CO$ |
| 32. $C_2H_6 \rightarrow CH_3 + CH_3$ | |
| 33. $CH_3O + M \rightarrow H + CH_2O$ | |

M (third body)

Appendix C. Comprehensive data set of induction times

- C-1 to 7. induction times of *n*-heptane
- C-8 to 14. induction times of *n*-dodecane
- C-15 to 21. induction times of *iso*-octane

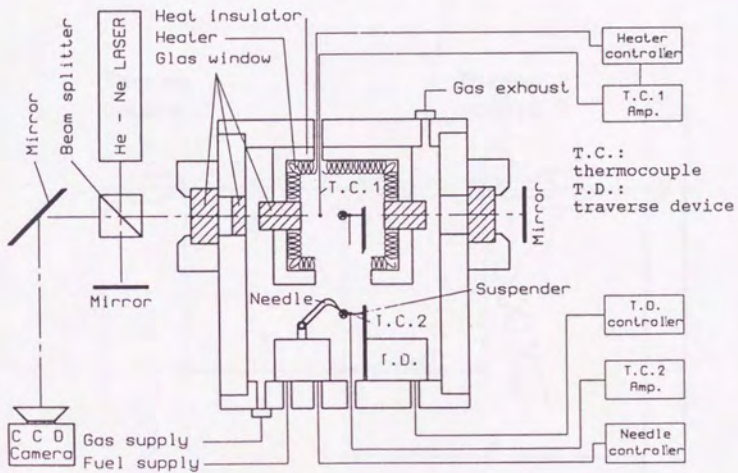


Figure 2-1-1. A schematic of the experimental setup

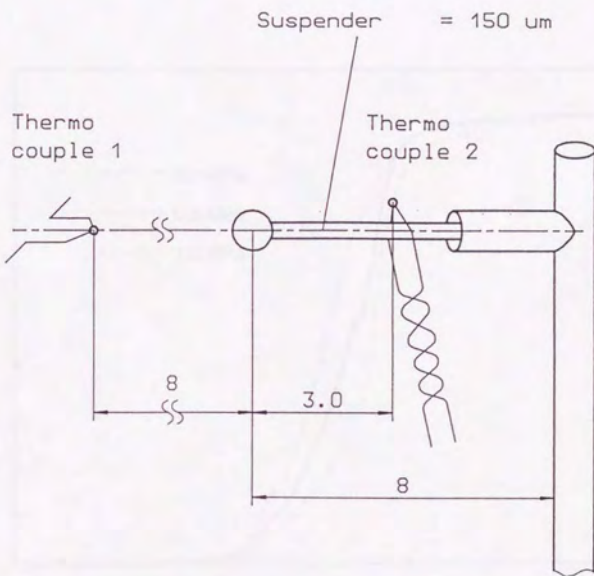


Figure 2-1-2. Suspender configuration

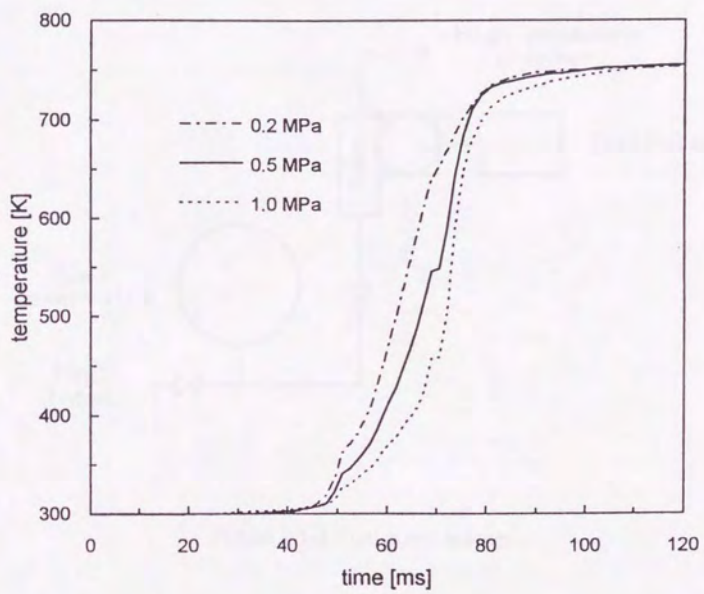


Figure 2-1-3. Temperature rise that a droplet undergoes at insertion to the furnace

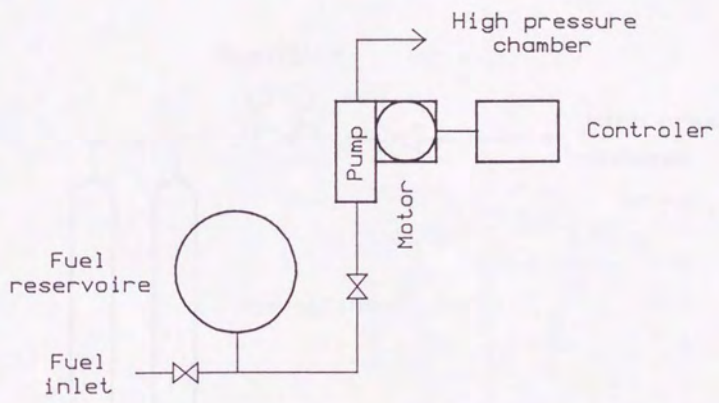


Figure 2-1-4. Fuel pump system

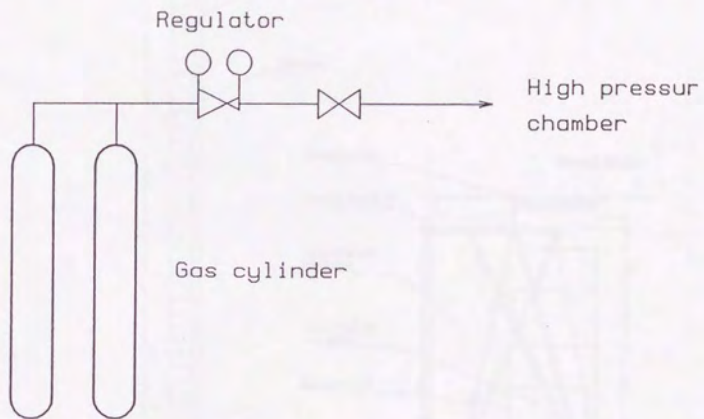


Figure 2-1-5. Gas supply system

146m

Drop Tower "Bremen"

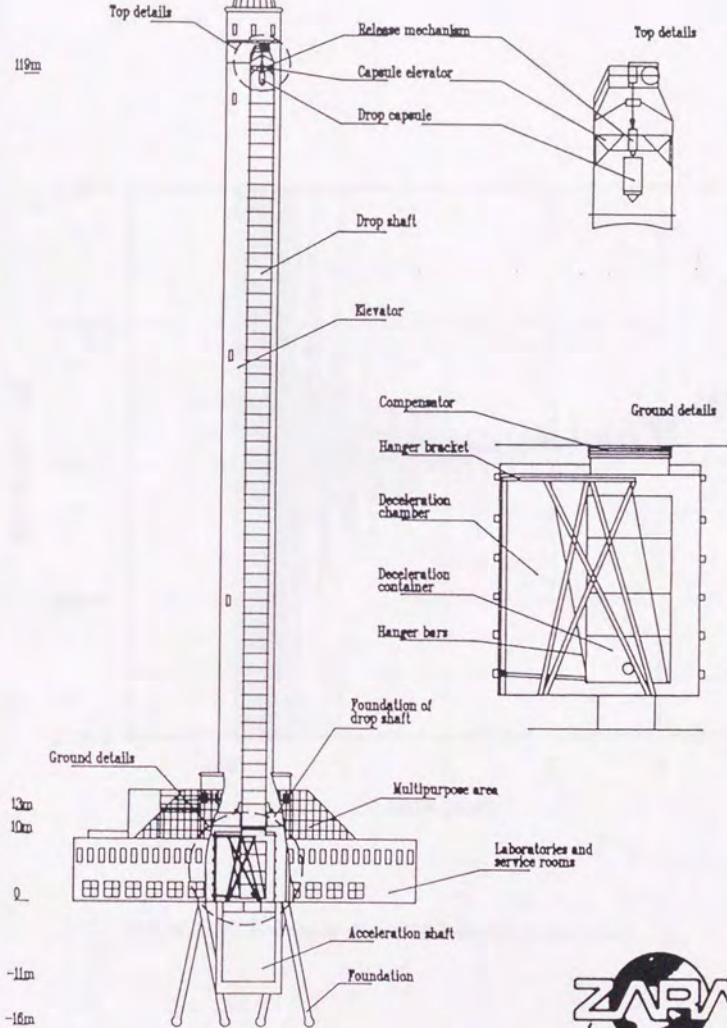


Figure 2-2-1. Bremen droptower

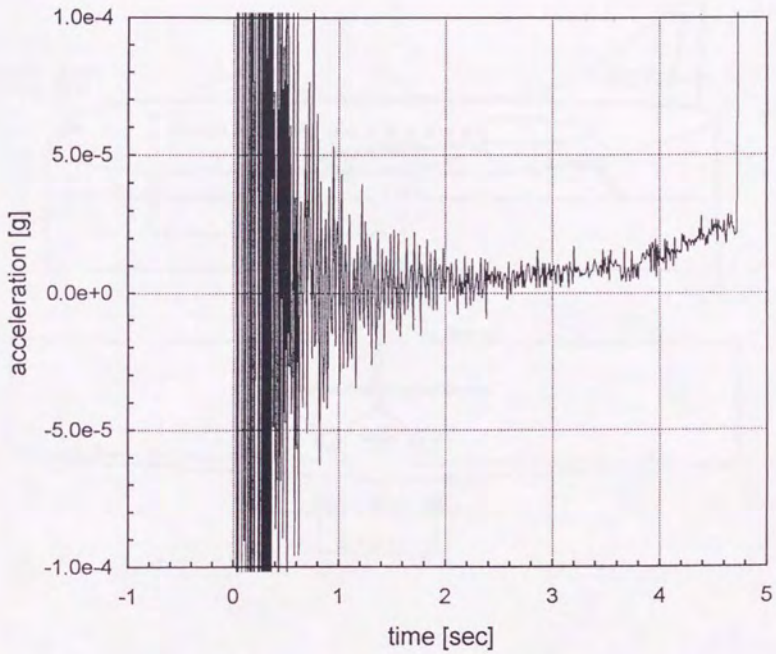


Figure 2-2-2. Gravity level during free-fall in droptower

Porte cargo
1 x 1,70 m

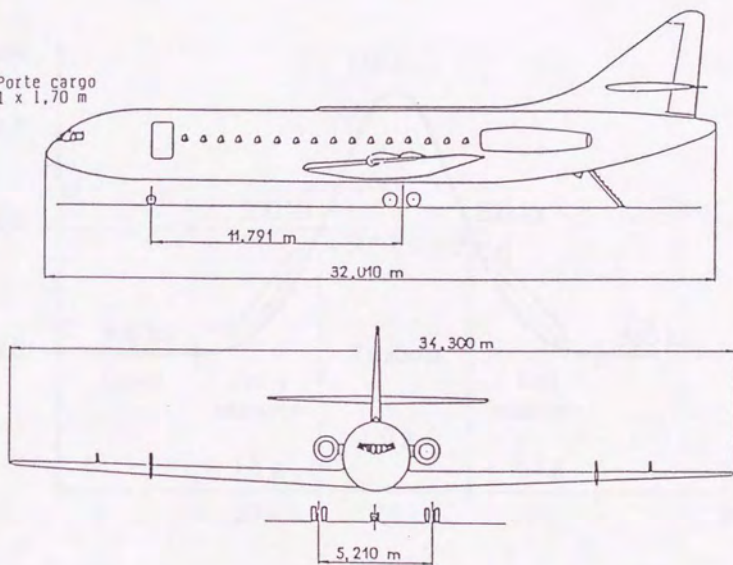


Figure 2-2-3. Caravelle twin jet used for parabolic flights

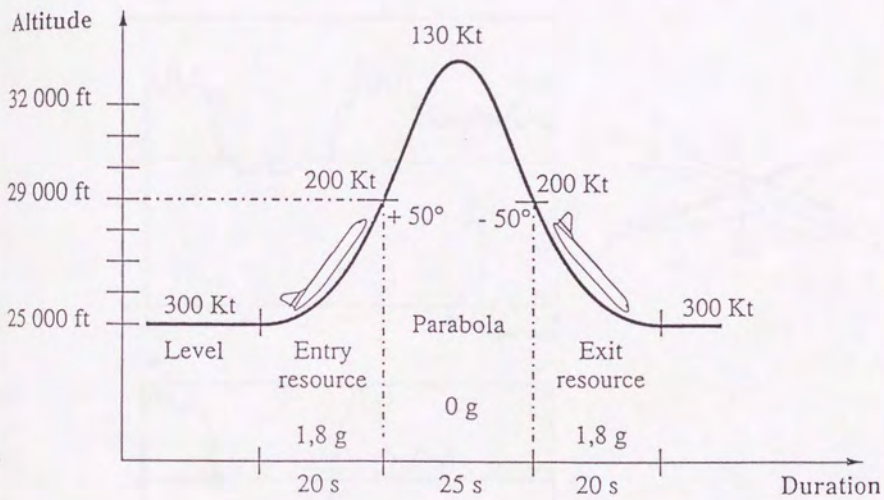


Figure 2-2-4. Flight profile of parabolic flight

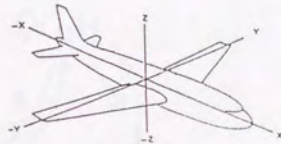
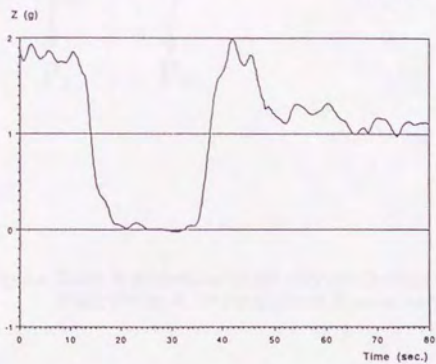
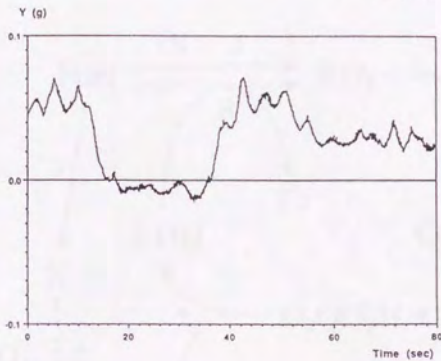
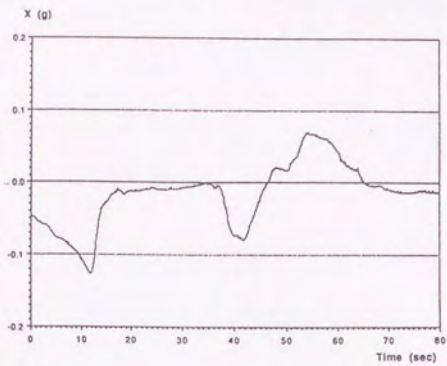


Figure 2-2-5. Gravity level during parabola

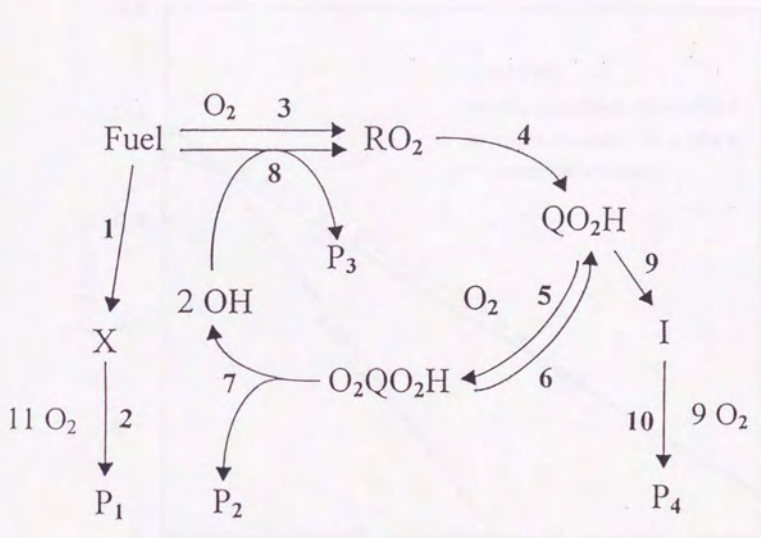


Figure 3-4-1. A schematic illustration of Griffiths' 10-reaction model [52]
 Fuel; C7H16, R; C7H15, Q; C7H14, P; products (imaginaly species)

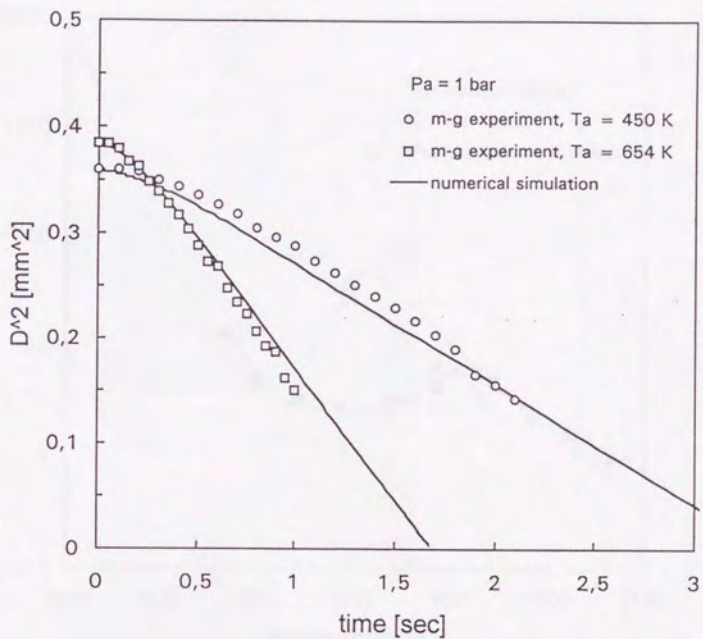


Figure 3-5-1. Squared diameter history for the case of evaporation
 a comparison between experimental results and simulation
 microgravity experiments is taken from ref. [68].

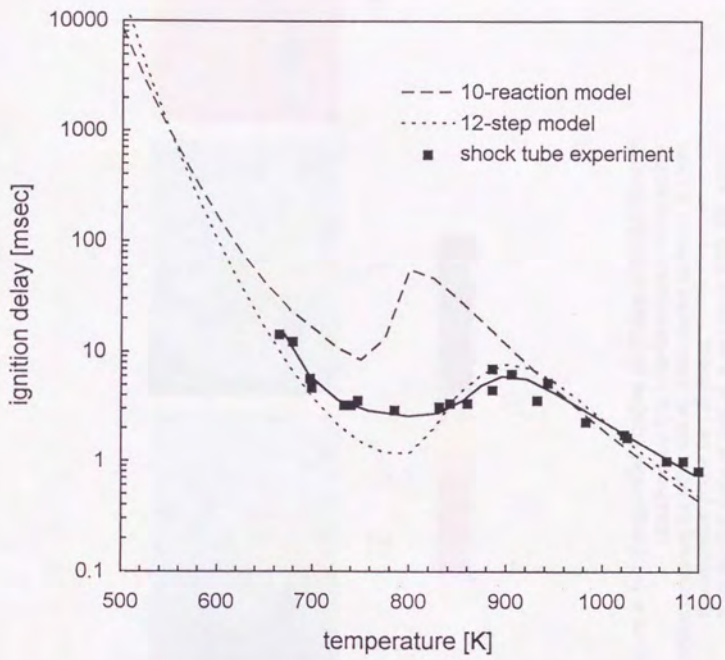


Figure 3-5-2. Ignition delay over temperature
 a comparison between shock-tube experiment and simulations
 initial pressure; 1.35 MPa, shock-tube data is taken from ref. [65].

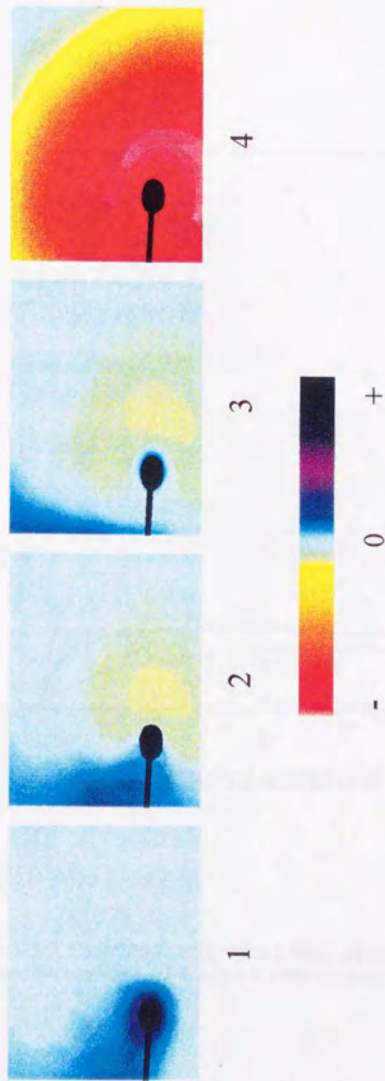


Figure 4-1-1. Sequential images of phase shift distribution obtained by the interferometer, false color ambient condition; 0.5 MPa, 650 K, initial droplet diameter; 0.7 mm

- 1) evaporation phase (at 120 msec)
- 2) the first stage of ignition, a cool flame (160, 200 msec)
- 3) ignition, a hot flame (240 msec)
- 4) ignition, a hot flame (240 msec)

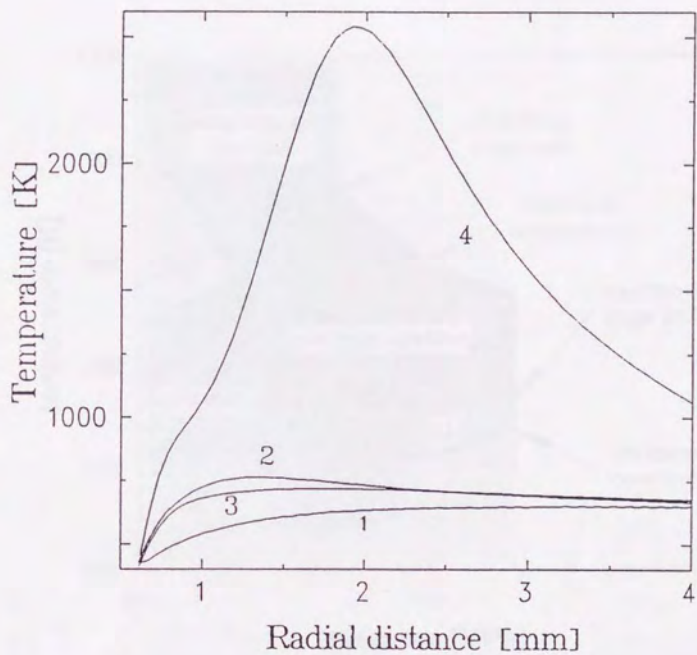


Figure 4-1-2. Estimated temperature field variation with time
the same experiment as figure 4-1-1. origin of radial distance is the droplet center

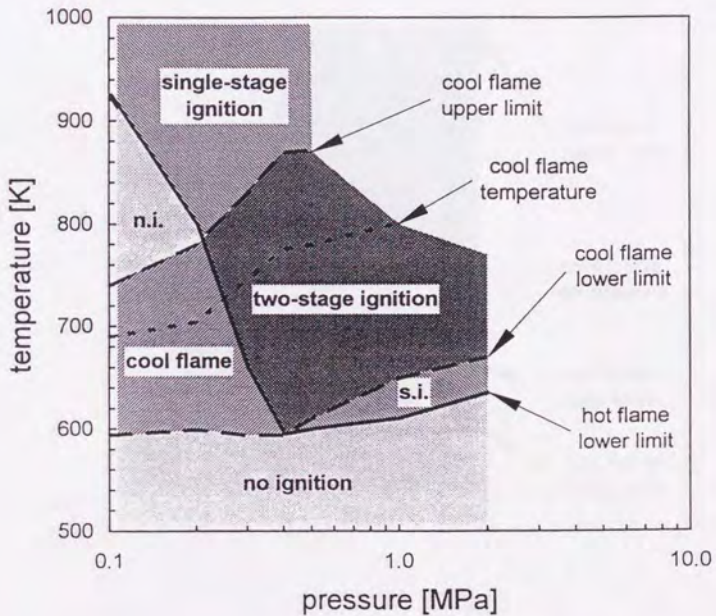


Figure 4-2-1. Ignition regions and characteristic temperatures of *n*-heptane droplet (Initial droplet diameter; 0.7-0.75 mm)

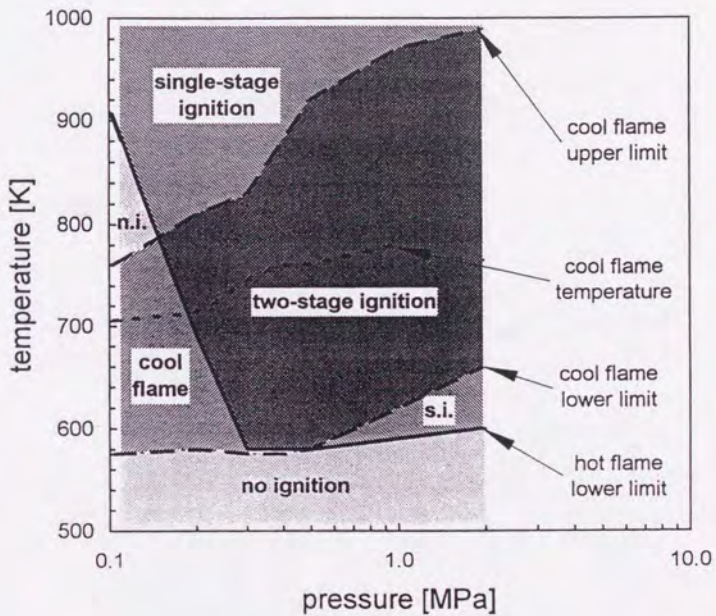


Figure 4-2-2. Ignition regions and characteristic temperatures of *n*-dodecane droplet (Initial droplet diameter; 0.7-0.8 mm)

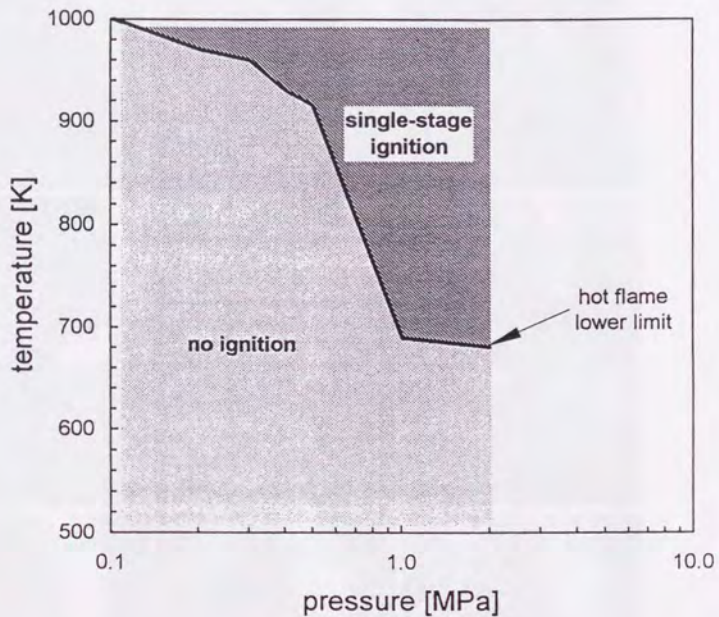


Figure 4-2-3. Ignition regions and characteristic temperatures of *iso*-octane droplet (Initial droplet diameter; 0.7-0.75 mm)

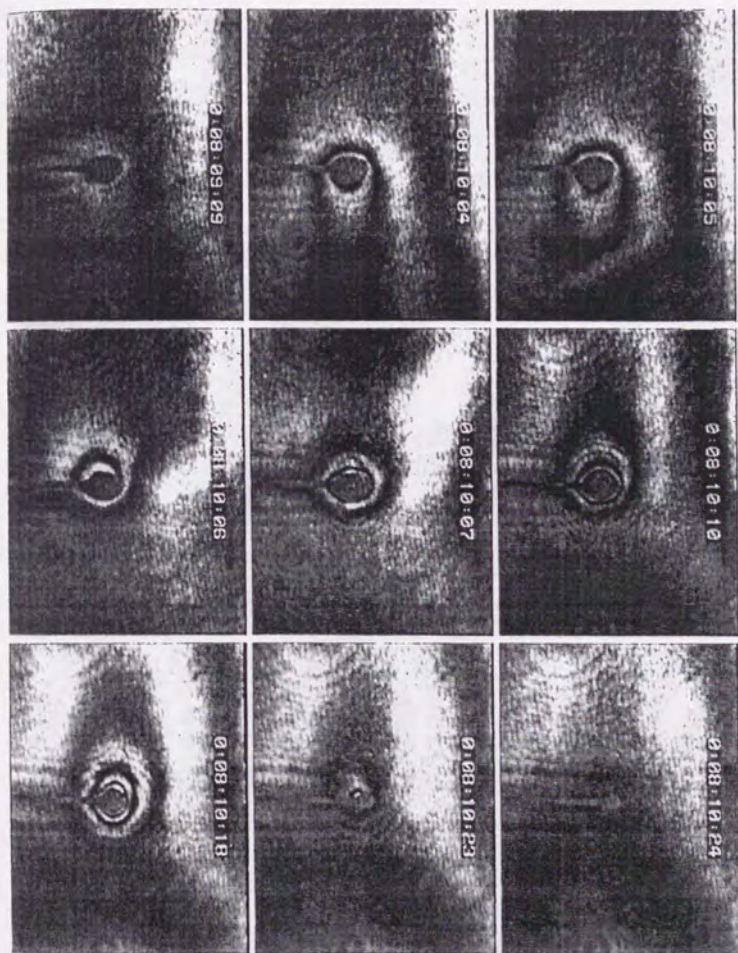


Figure 4-3-1. Sequential images of interferometric fringes
 cool flame under normal gravity
n-dodecane droplet, ambient condition; 0.2 MPa, 610 K

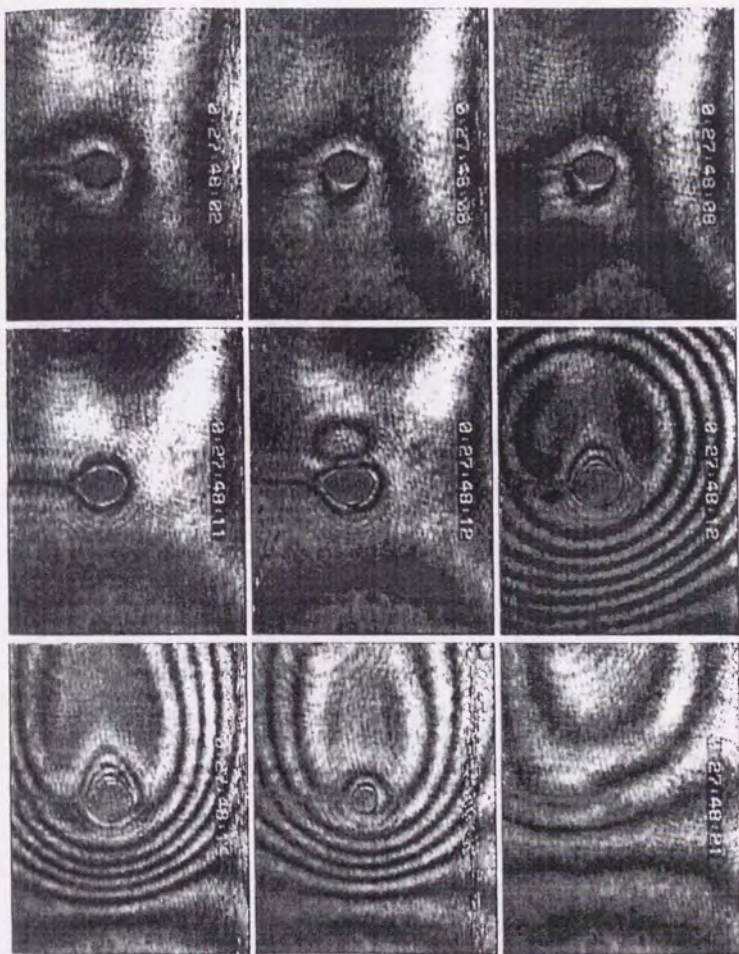


Figure 4-3-2. Sequential images of interferometric fringes
two-stage process under normal gravity
n-dodecane droplet, ambient condition; 0.5 MPa, 680 K

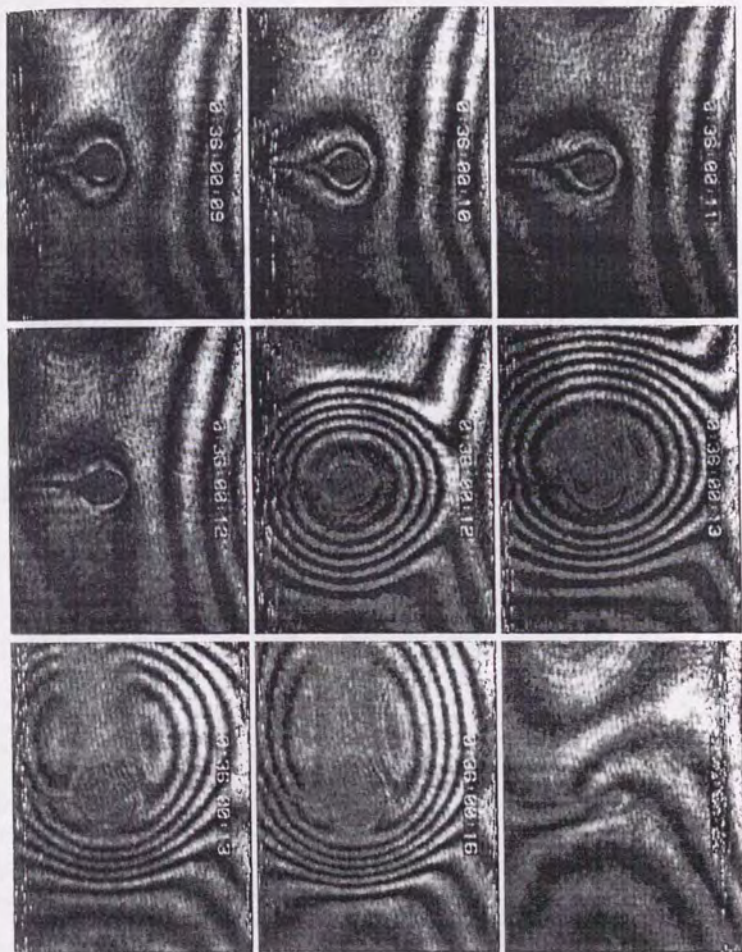


Figure 4-3-3. Sequential images of interferometric fringes
single-stage process under normal gravity
n-dodecane dropelt, ambient condition; 1.0 MPa, 900 K

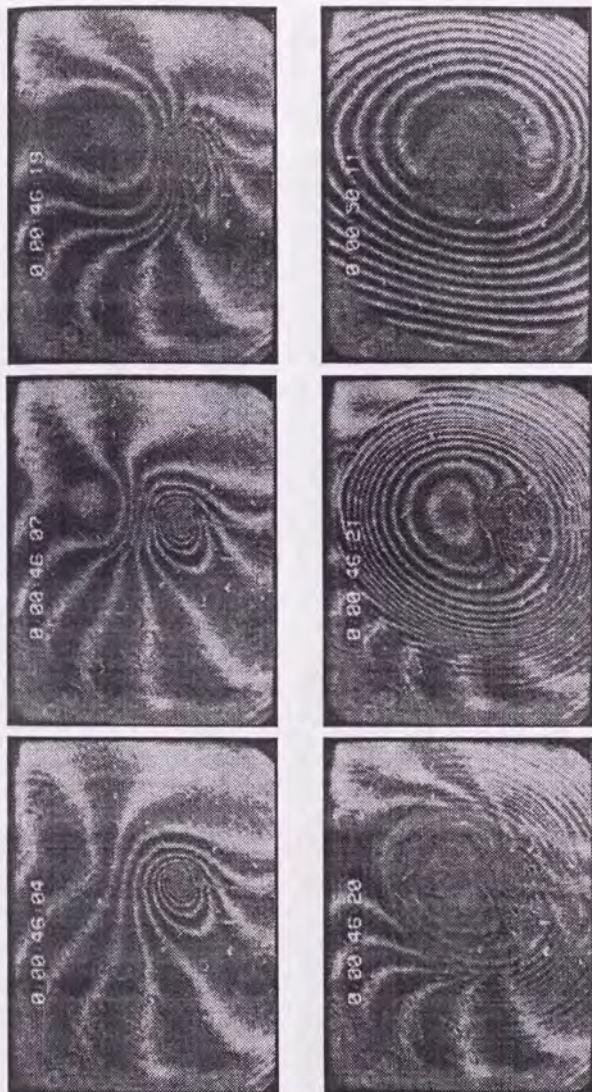


Figure 4-3-4. Sequential images of interferometric fringes
low ambient temperature case
n-heptane droplet, ambient condition; 0.5 MPa, 600 K

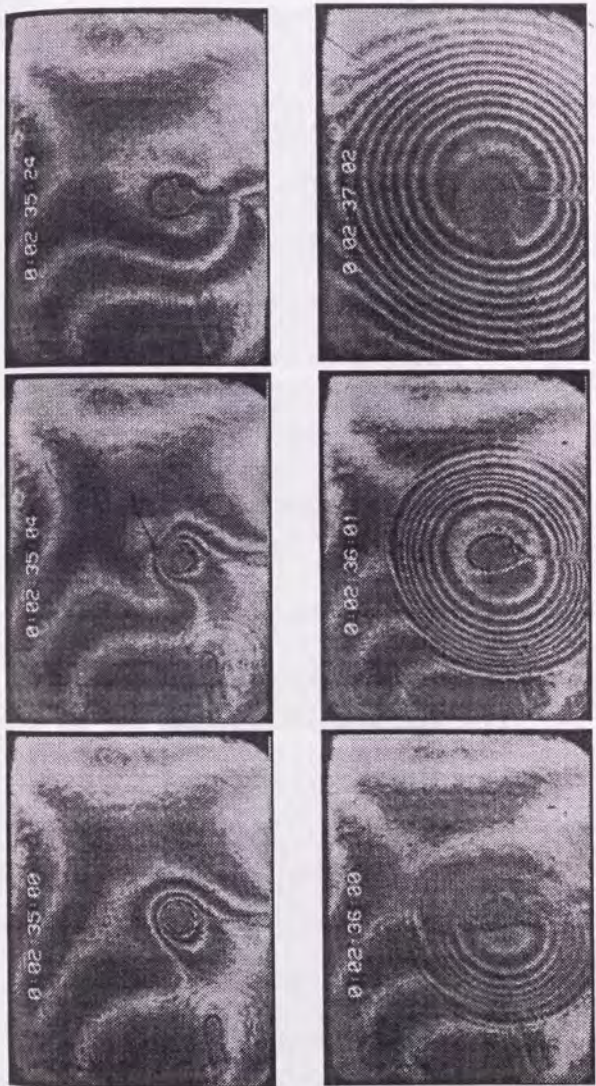


Figure 4-3-5. Sequential images of interferometric fringes
middle ambient temperature case
n-heptane droplet, ambient condition; 0.5 MPa, 650 K



Figure 4-3-6. Sequential images of interferometric fringes
high ambient temperature case
n-heptane droplet, ambient condition: 0.5 MPa, 800 K

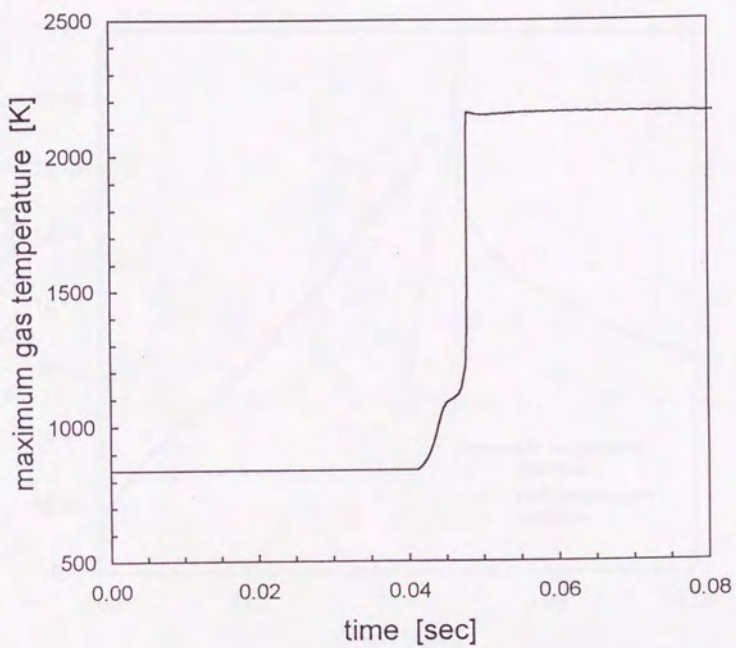


Figure 4-4-1. Simulated two step temperature rise with 10-reactor model
ambient condition; 1.0 MPa, 840 K, initial droplet diameter; 0.7 mm

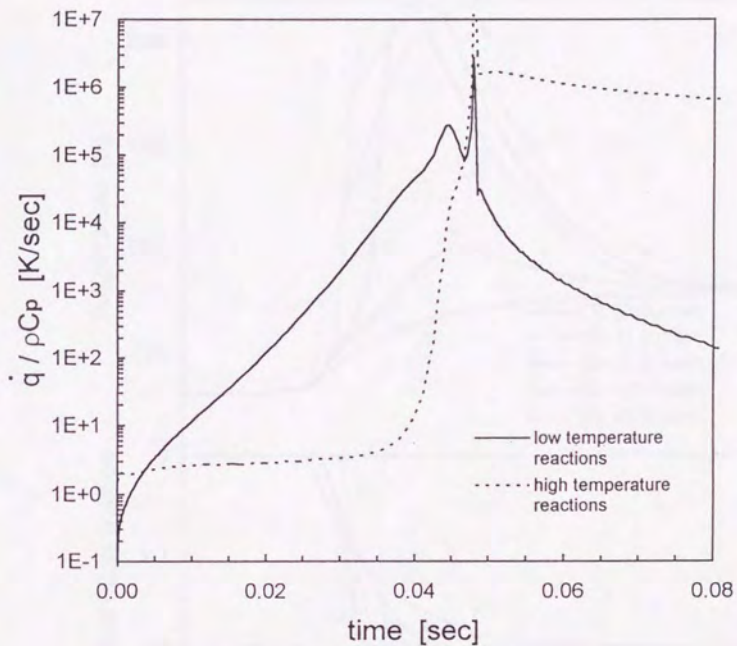


Figure 4-4-2. Heat release history, the time varying activity of the low- and the high-temperature reaction simulated result with 10-step reaction model ambient condition; 1.0 MPa, 840 K, initial droplet diameter; 0.7 mm both values are taken from the grid point where the total heat release is the maximum among all grids

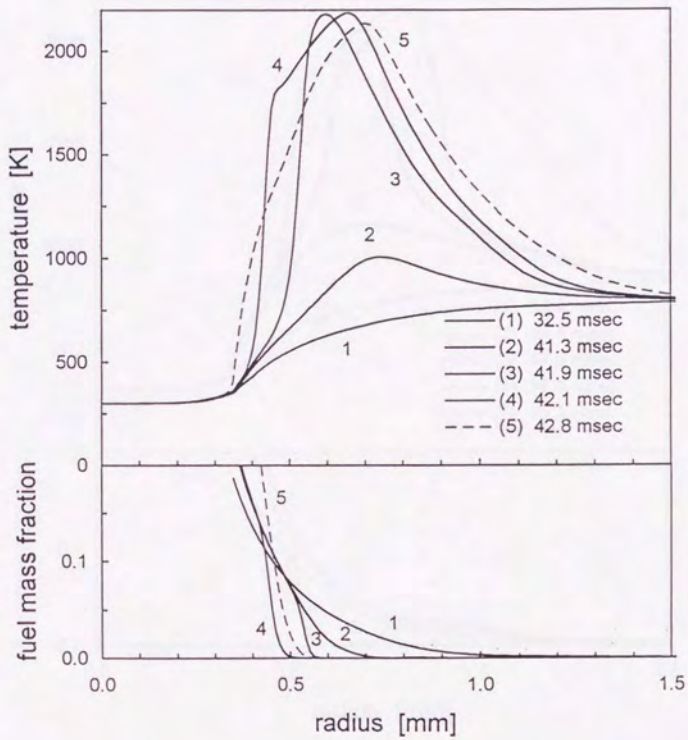


Figure 4-4-3. Variation of temperature profiles with time up to the diffusion flame formation, ambient temperature of below NTC region
 simulated result with 10-step reaction model
 ambient condition; 1.0 MPa, 800 K, initial droplet diameter; 0.7 mm

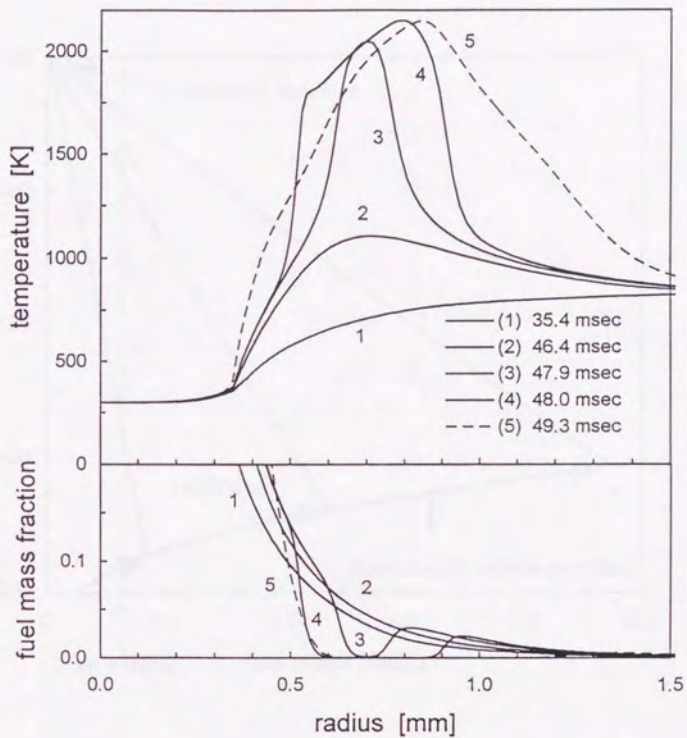


Figure 4-4-4 Variation of temperature profiles with time up to the diffusion flame formation, ambient temperature of in NTC region
 simulated result with 10-step reaction model
 ambient condition; 1.0 MPa, 840 K, initial droplet diameter; 0.7 mm

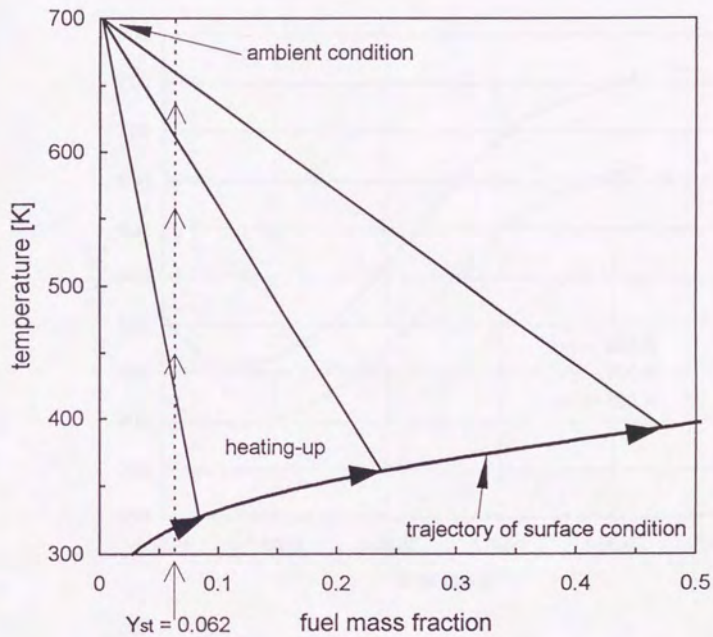


Figure 4-5-1. Transient process of mixture formation, surface temperature rise and the movement of the flamelet line on temperature-fuel mass fraction plane the temperature at the place of stoichiometry raises with the change in surface condition

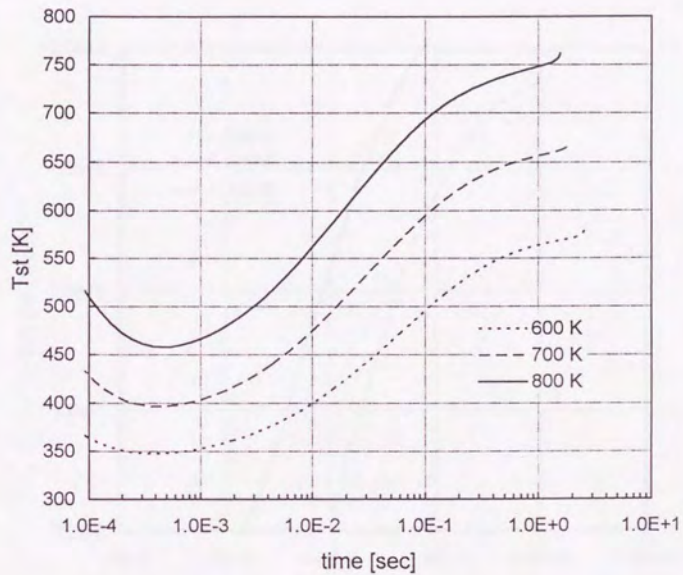


Figure 4-5-2. Temperature change at a place of stoichiometry during evaporation simulation, ambient pressure; 0.5 MPa, initial droplet diameter; 0.7 mm

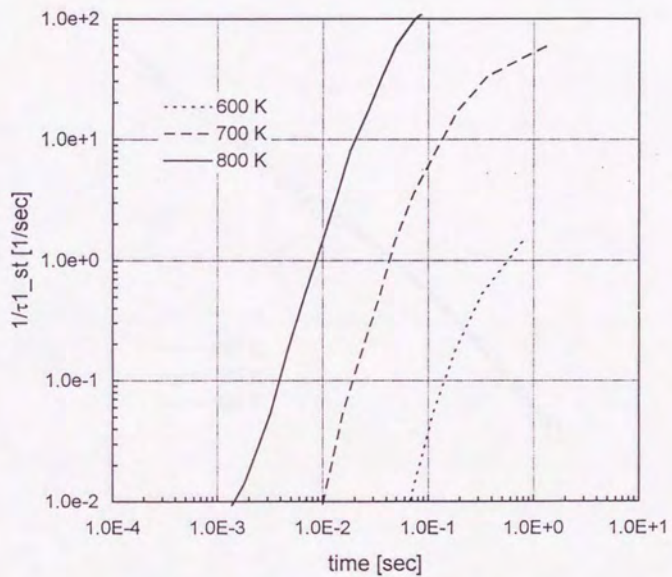


Figure 4-5-3. Mixture reactivity history at a place of stoichiometry simulation, the same condition as figure 4-5-2

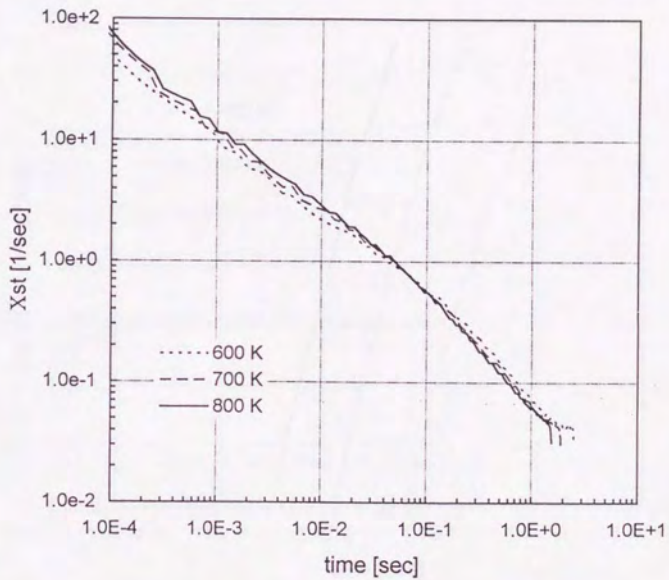


Figure 4-5-4. Temporal decay of dissipation rate at a place of stoichiometry simulation, the same condition as figure 4-5-2

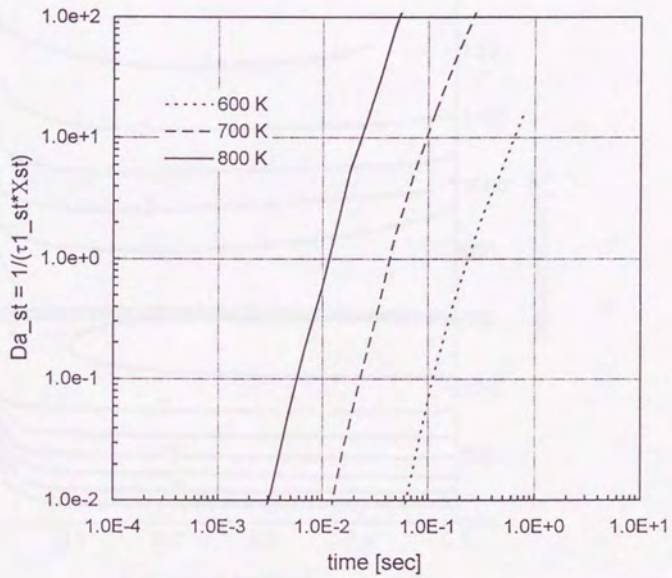


Figure 4-5-5. Damköhler number history simulation, the same condition as figure 4-5-2

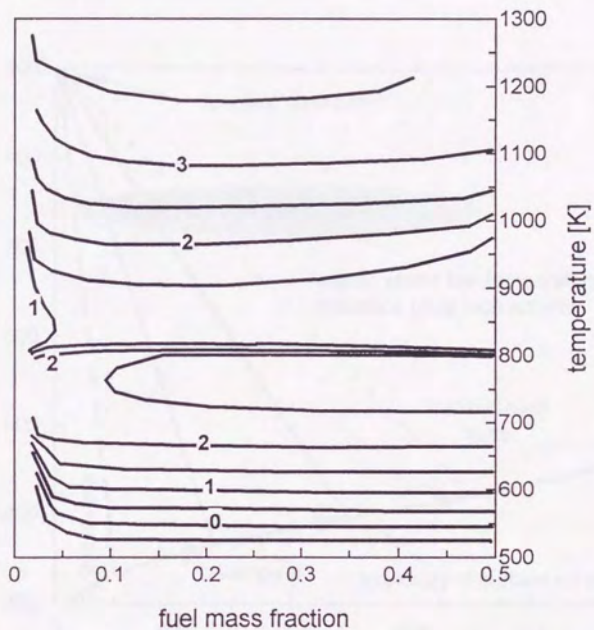


Figure 4-5-6. Mixture reactivity
 12-step model, premixed gas ignition at 0.5 MPa, the plotted values are $\log_{10}(1/\tau_1)$

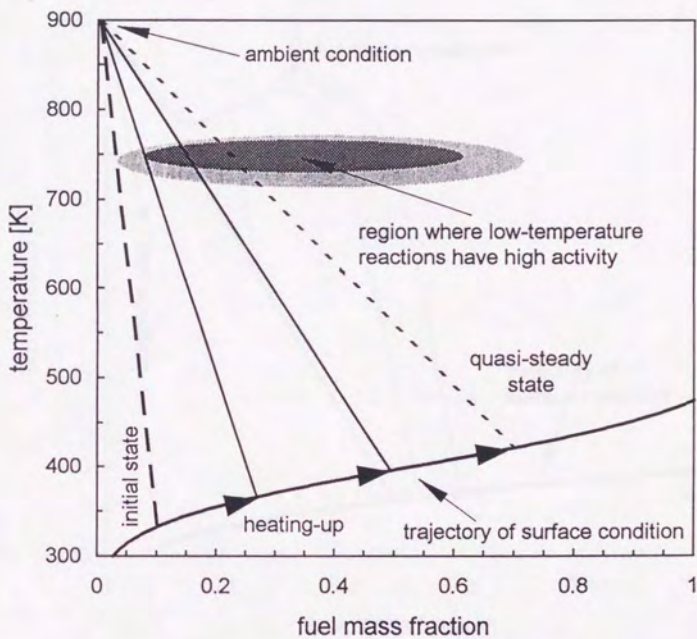


Figure 4-5-7. Transient flamelet and reactivity change with time before the onset of a cool flame

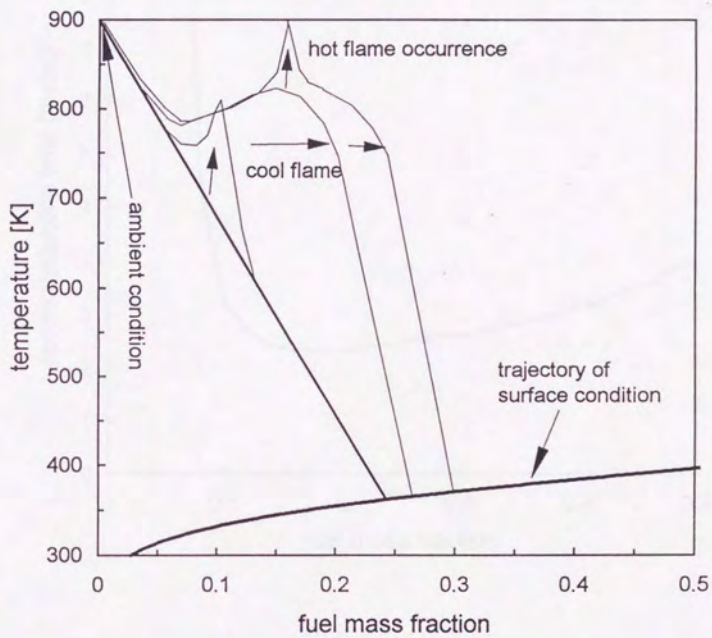


Figure 4-5-8. Transient flamelet during the first stage

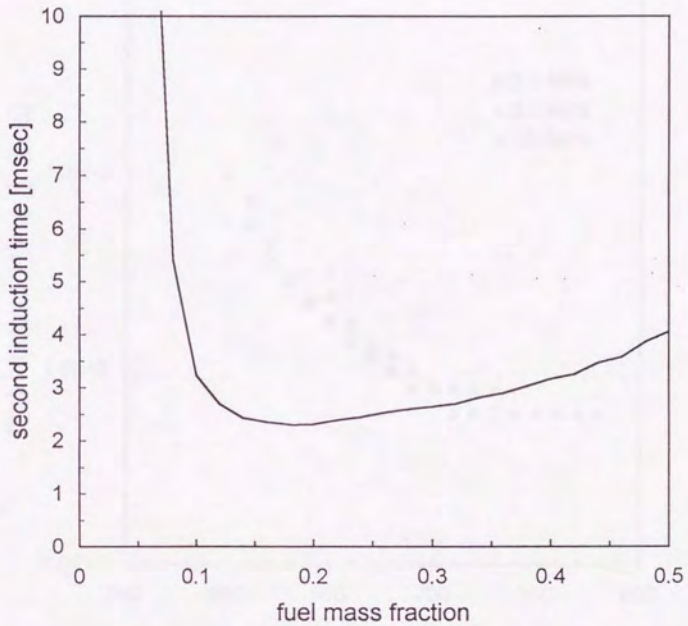
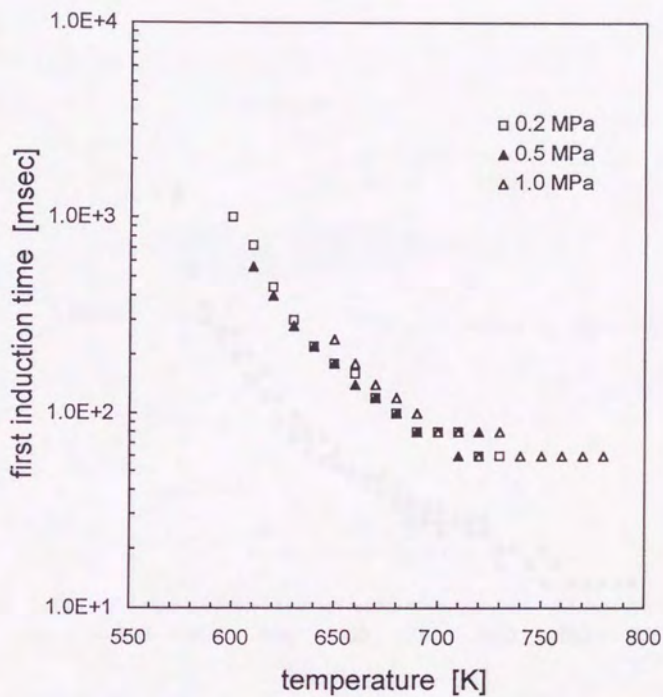
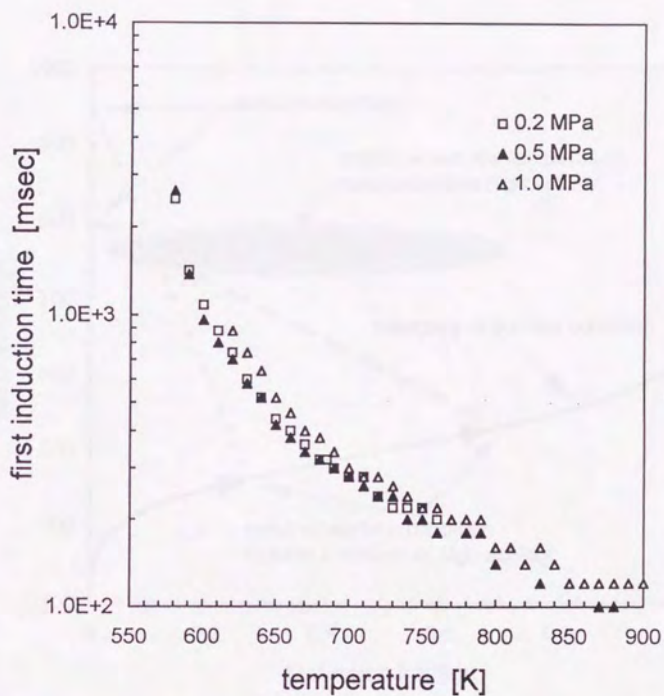


Figure 4-5-9. Fuel mass fraction dependence of the second induction time
12-step model, premixed gas ignition at 0.5 MPa, initial temperature; 600 K



n-Heptane droplet, normal gravity, $D_0 = 0.7-0.75$ mm

Figure 5-1-1. The first induction time against ambient temperature for a few pressure cases, *n*-heptane



n-dodecane droplet, normal gravity, $D_0 = 0.7-0.75$ mm

Figure 5-1-2. The first induction time against ambient temperature for a few pressure cases, *n*-dodecane

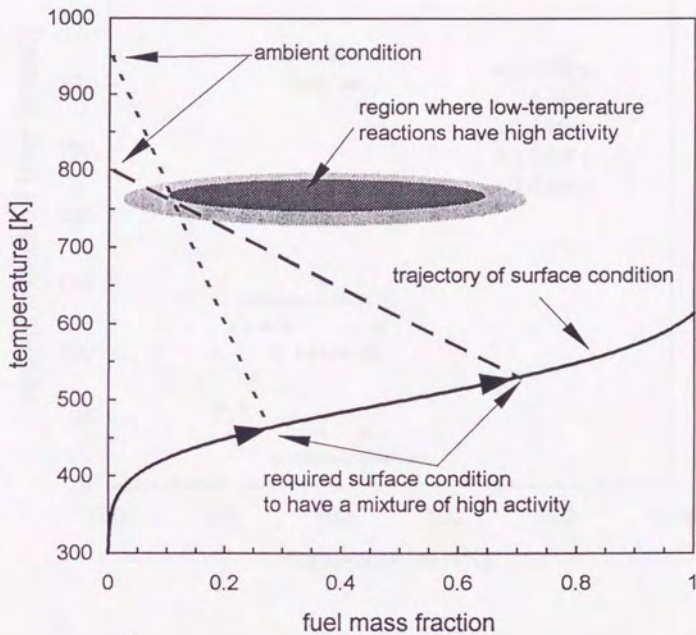
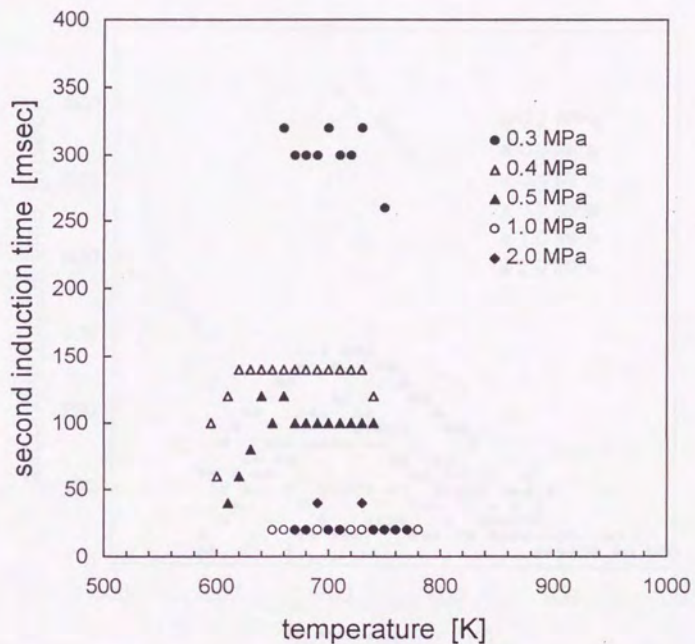
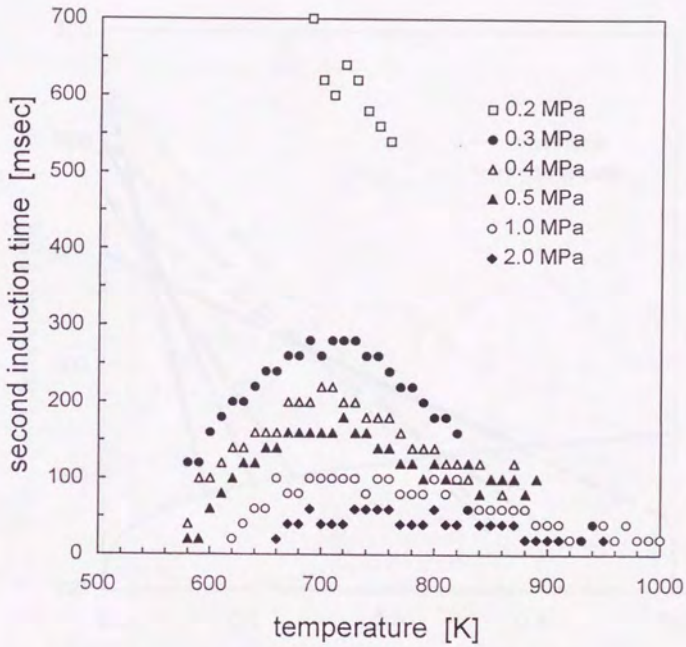


Figure 5-1-3. Geometric derivation of required surface condition



n-Heptane, normal gravity, D0 = 0.7-0.75 mm

Figure 5-2-1. The second induction time against ambient temperature for a few pressure cases, n-heptane



n-Dodecane, normal gravity, $D_0 = 0.7-0.8$ mm

Figure 5-2-2. The second induction time against ambient temperature for a few pressure cases, *n*-dodecane

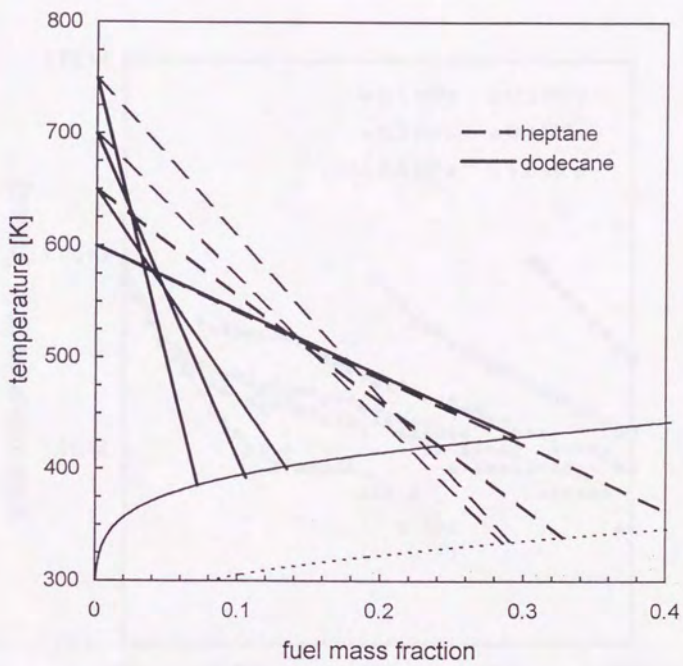
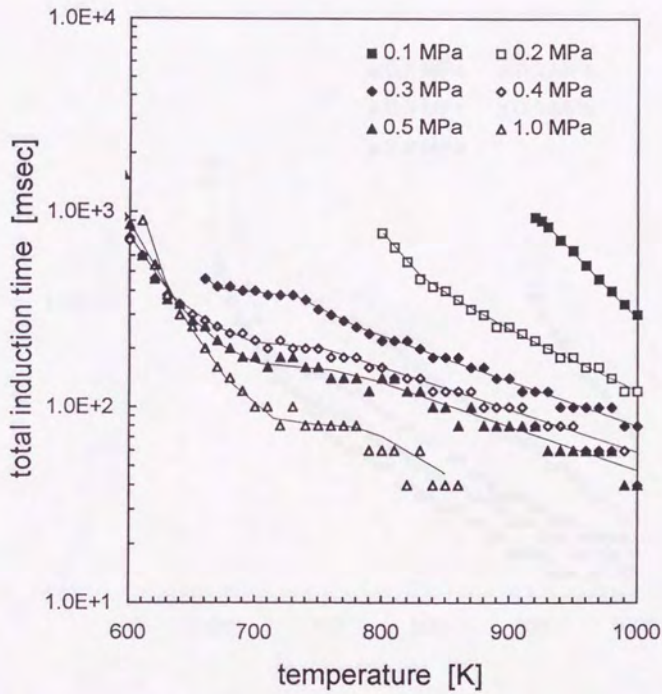
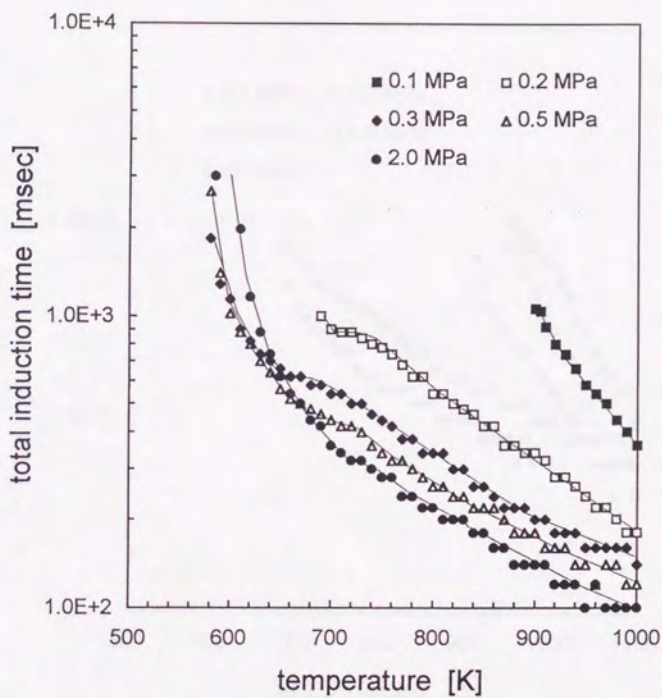


Figure 5-2-3. Gas phase conditions at the onset of the first stage



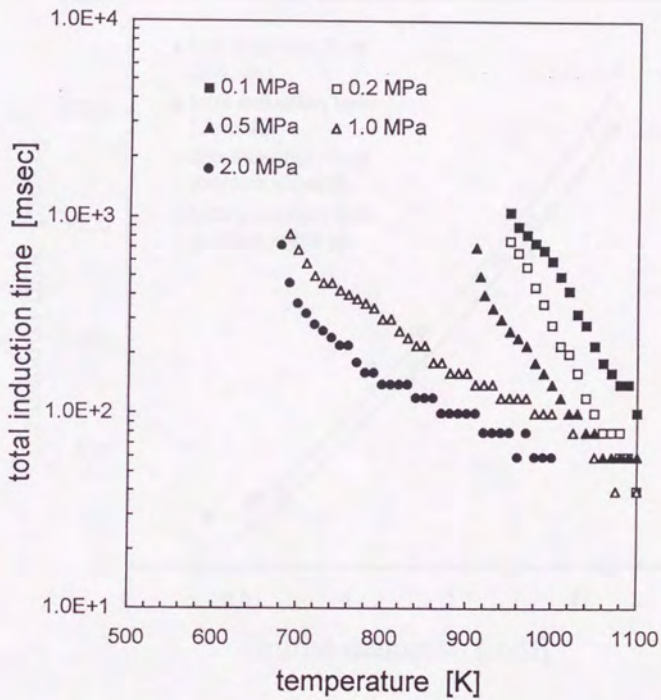
n-Heptane droplet, normal gravity, $D_0 = 0.7-0.75$ mm

Figure 5-3-1. the total induction time against ambient temperature for a few pressure cases, *n*-heptane



n-dodecane droplet, normal gravity, $D_0 = 0.7-0.75$ mm

Figure 5-3-2. The total induction time against ambient temperature for a few pressure cases, *n*-dodecane



i-Octane droplet, normal gravity, $D_0 = 0.7-0.75$ mm

Figure 5-3-3. The total induction time against ambient temperature for a few pressure cases, *iso*-octane

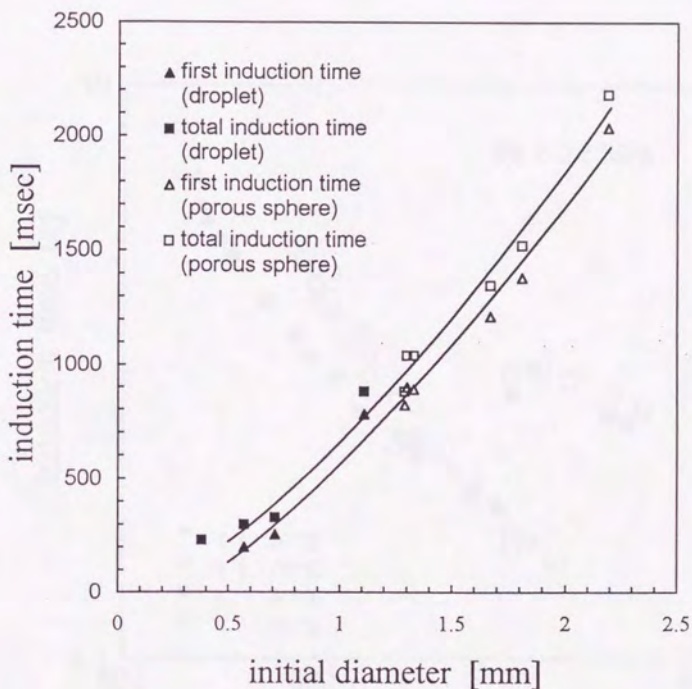


Figure 5-4-1. Variation in the induction times with initial droplet diameter
 spontaneous ignition of isolated droplets and porous spheres
 n-Dodecane, $P_a=0.5\text{MPa}$, $T_a=700\text{K}$, Drop tower experiment

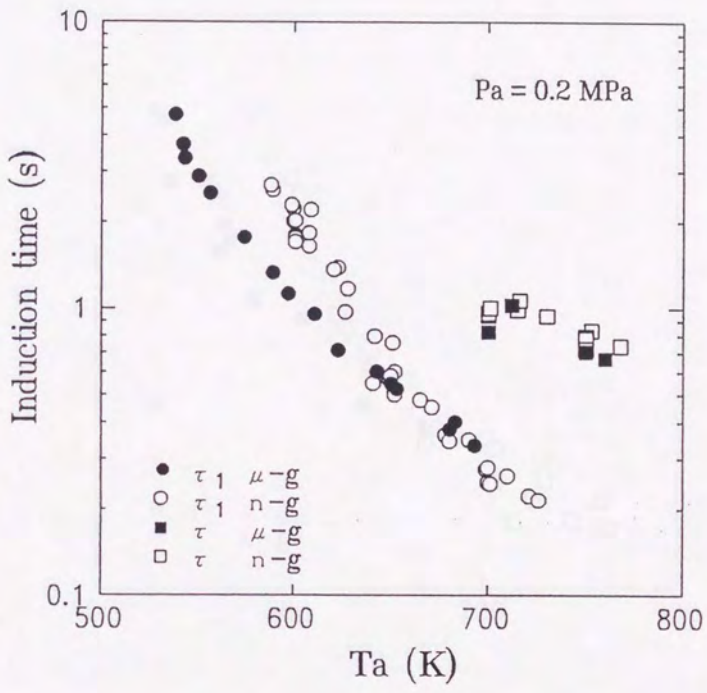


Figure 5-5-1. Comparisons of induction times under normal- and microgravity *n*-dodecane droplet 0.65-0.75 mm, ambient pressure; 0.2 MPa

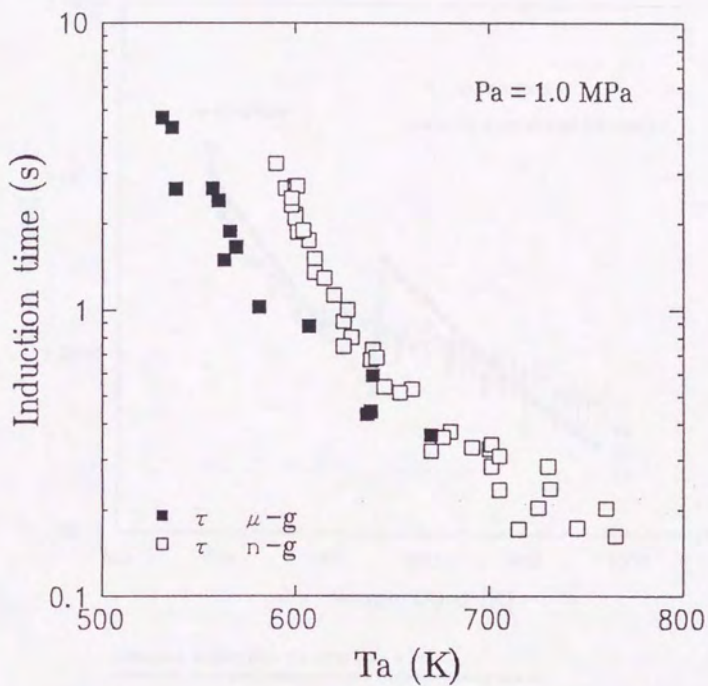
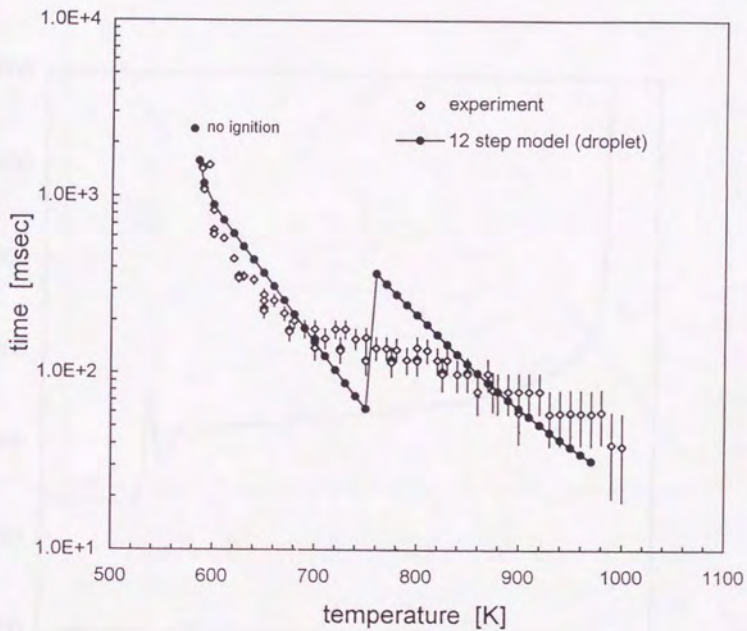


Figure 5-5-2. Comparisons of the total induction times under normal- and microgravity
n-dodecane droplet 0.65-0.75 mm, ambient pressure; 1.0 MPa



n-Heptane droplet, Pa = 0.5 MPa, D0 ~ 0.7 mm
 experiments : normal gravity, measurement error is shown by means of error bar

Figure 5-6-1. Comparisons of ignition delay, experiments and simulation

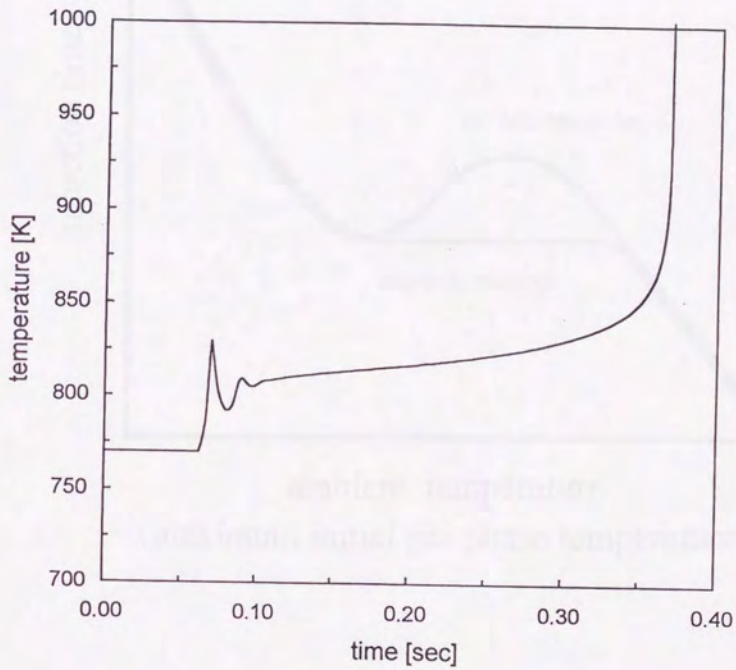


Figure 5-6-2. Typical calculated temperature history
12-step model, 0.7 mm droplet, 0.5 MPa, 780 K

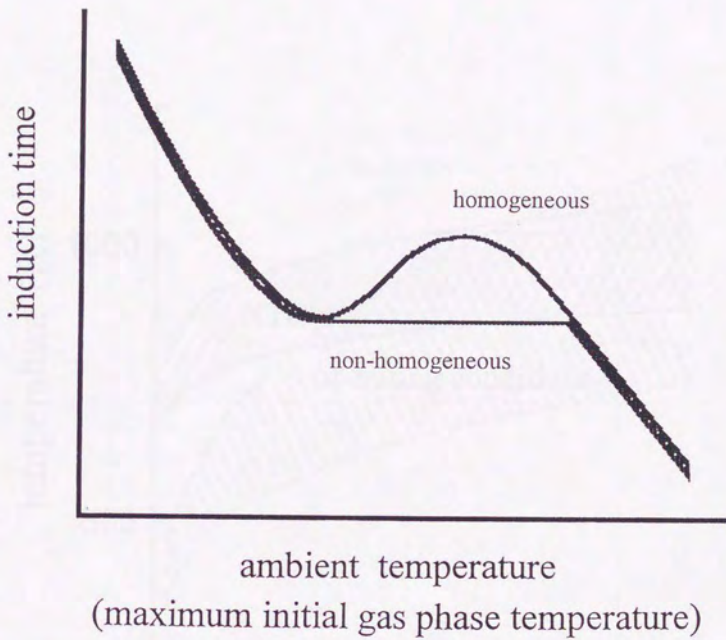


Figure 5-7-1. NTC of homogeneous premixed gas ignition and ZTC of non-homogeneous ignition

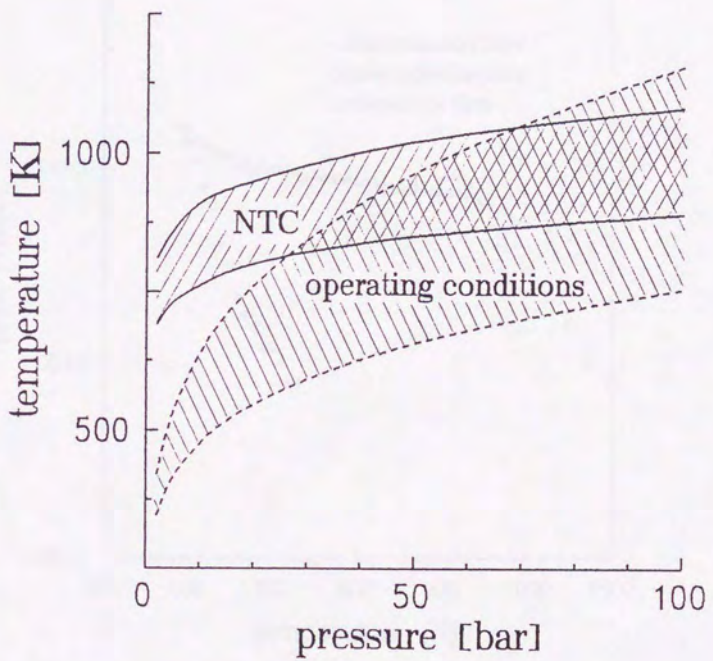
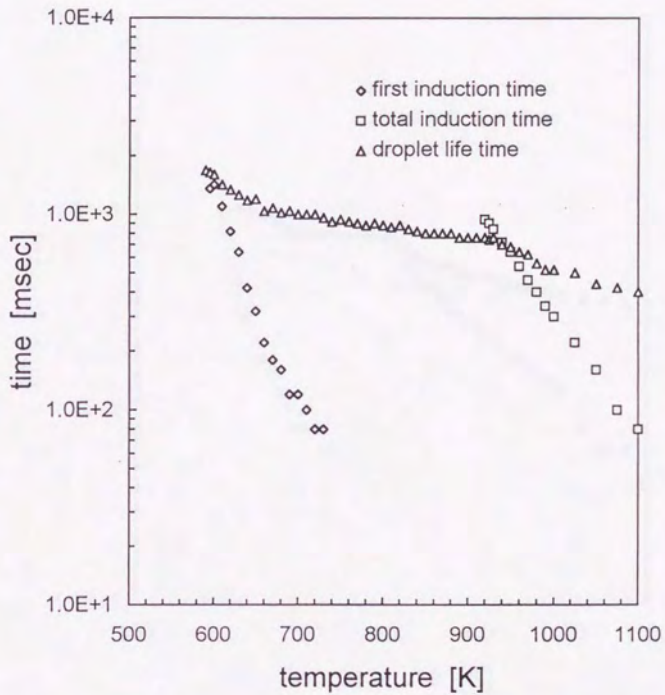
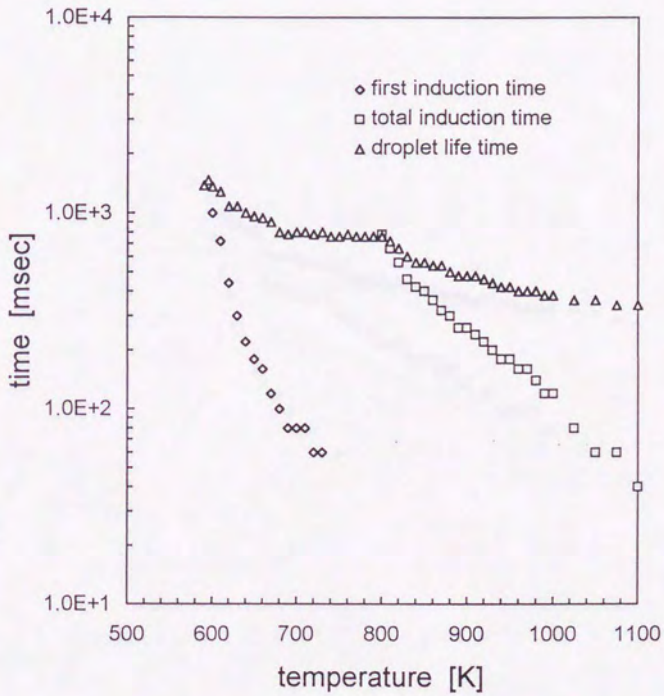


Figure 5-7-2. Conditions of adiabatically compressed gases



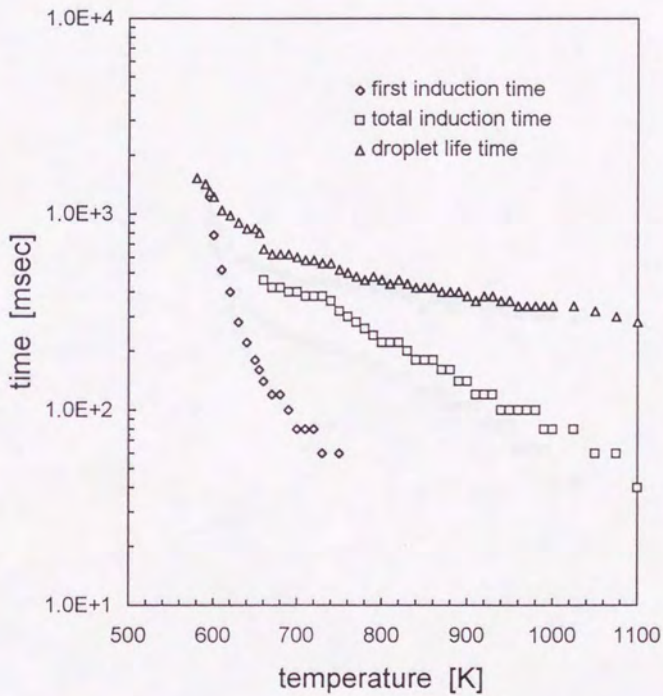
n-Heptane droplet, normal gravity, $D_0 = 0.7\text{-}0.75$ mm, $P_a = 0.1$ MPa

Figure C-1



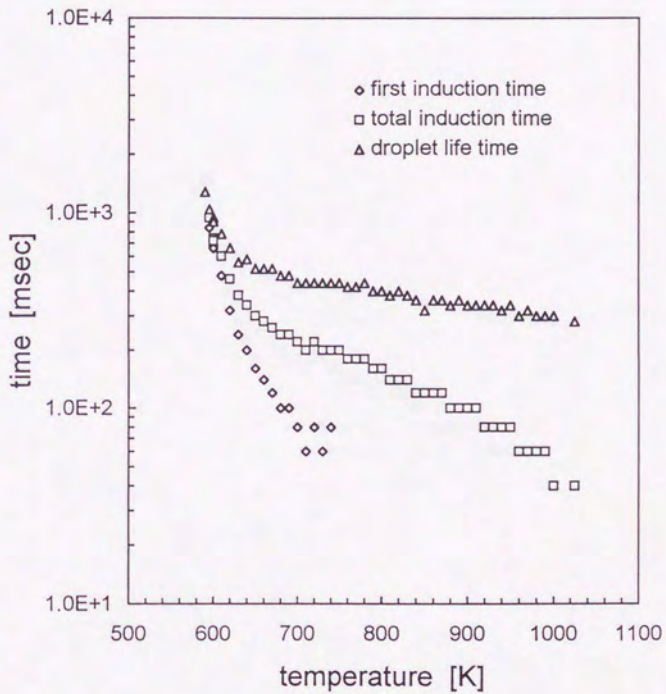
n-Heptane droplet, normal gravity, $D_0 = 0.7-0.75$ mm, $P_a = 0.2$ MPa

Figure C-2



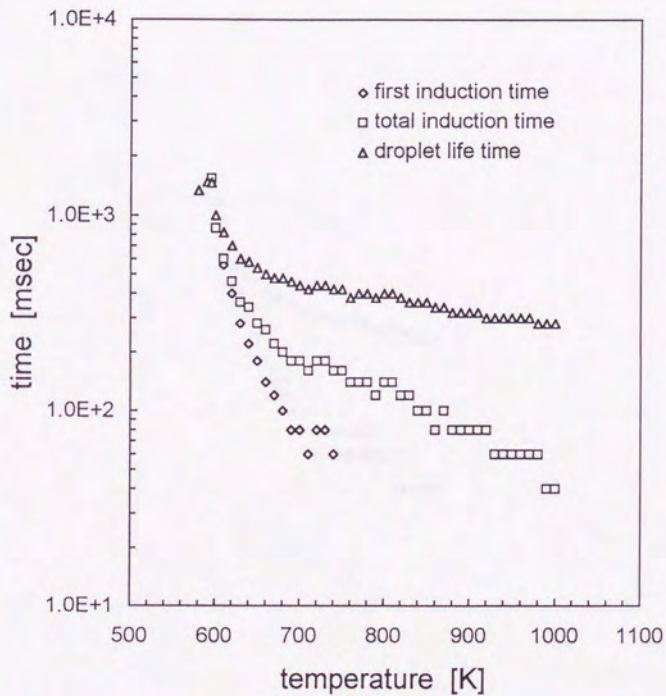
n-Heptane droplet, normal gravity, $D_0 = 0.7-0.75$ mm, $P_a = 0.3$ MPa

Figure C-3



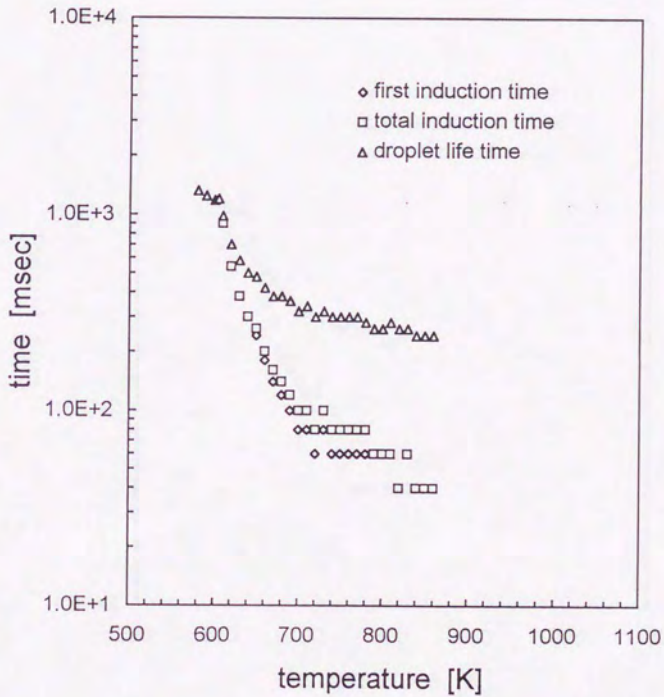
n-Heptane droplet, normal gravity, $D_0 = 0.7-0.75$ mm, $P_a = 0.4$ MPa

Figure C-4



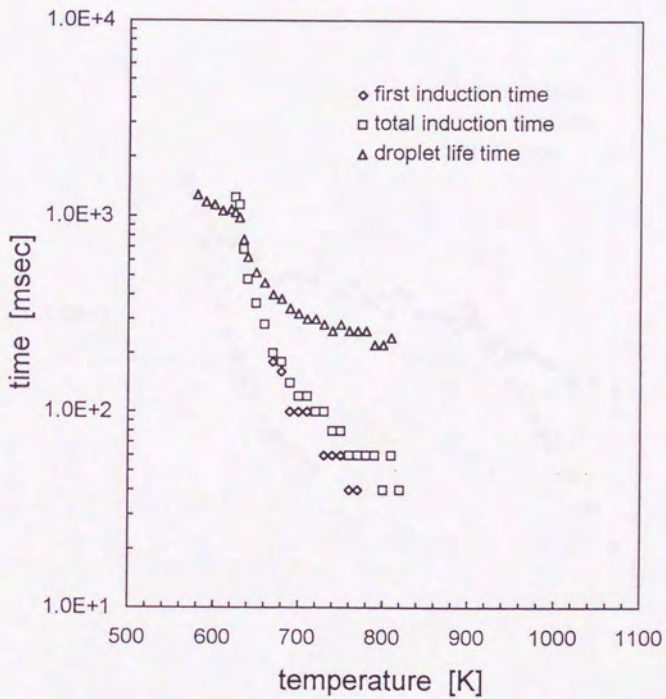
n-Heptane droplet, normal gravity, $D_0 = 0.7\text{-}0.75$ mm, $P_a = 0.5$ MPa

Figure C-5



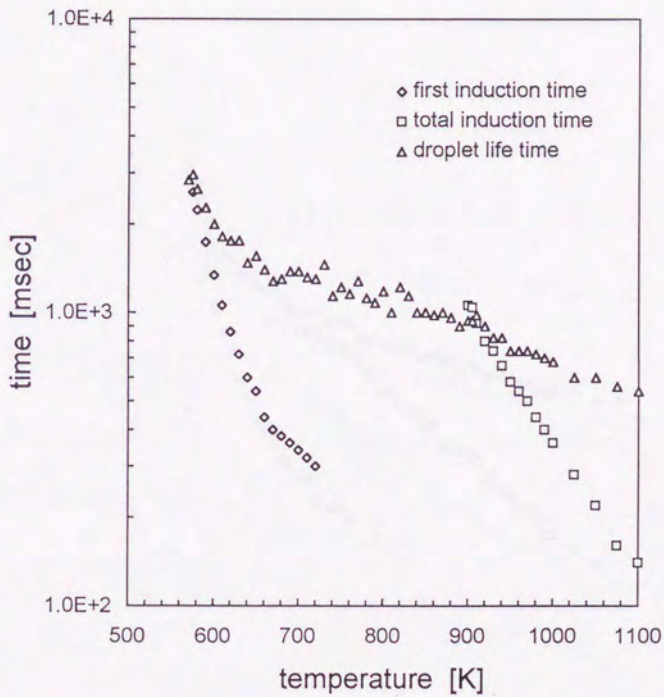
n-Heptane droplet, normal gravity, $D_0 = 0.7-0.75$ mm, $P_a = 1.0$ MPa

Figure C-6



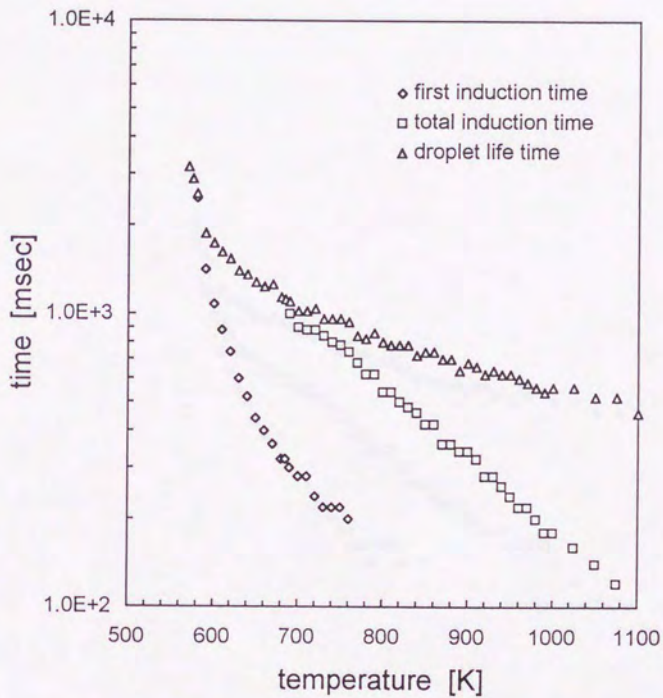
n-Heptane droplet, normal gravity, $D_0 = 0.7-0.75$ mm, $P_a = 2.0$ MPa

Figure C-7



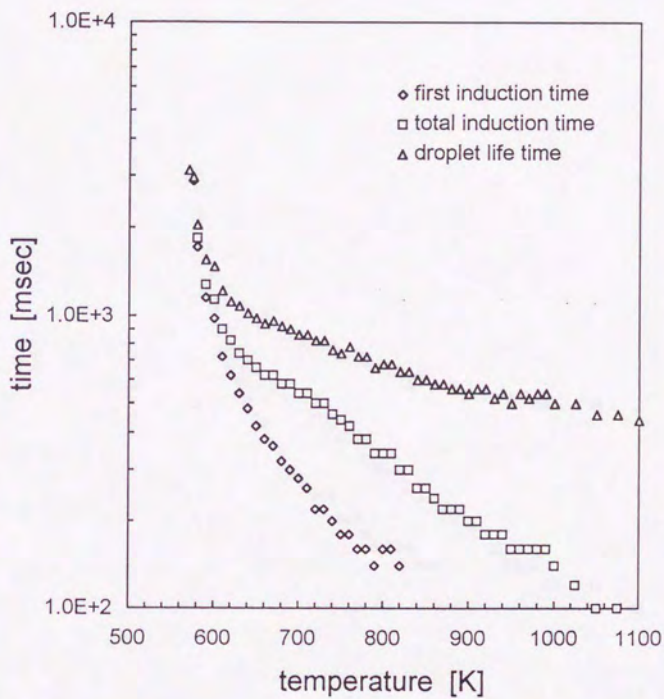
n-Dodecane droplet, normal gravity, $D_0 = 0.7-0.8\text{mm}$, $P_a = 0.1\text{ MPa}$

Figure C-8



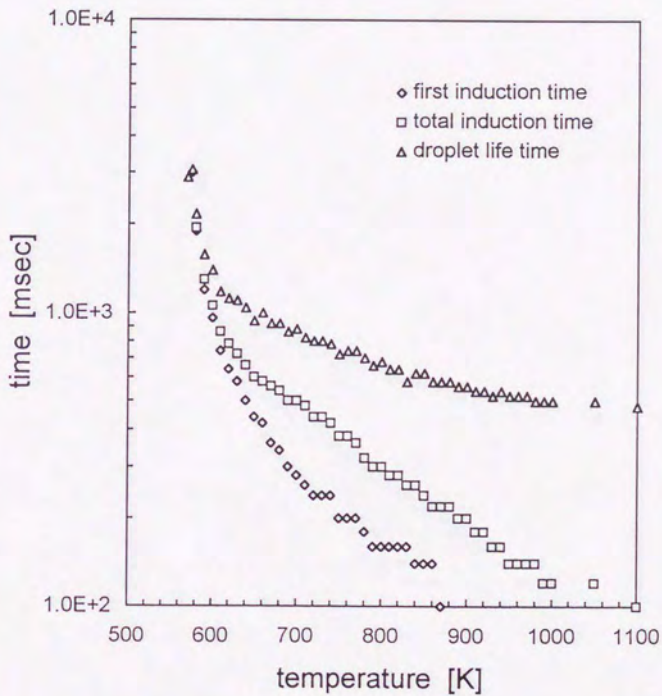
n-Dodecane droplet, normal gravity, $D_0 = 0.7-0.8\text{mm}$, $P_a = 0.2\text{ MPa}$

Figure C-9



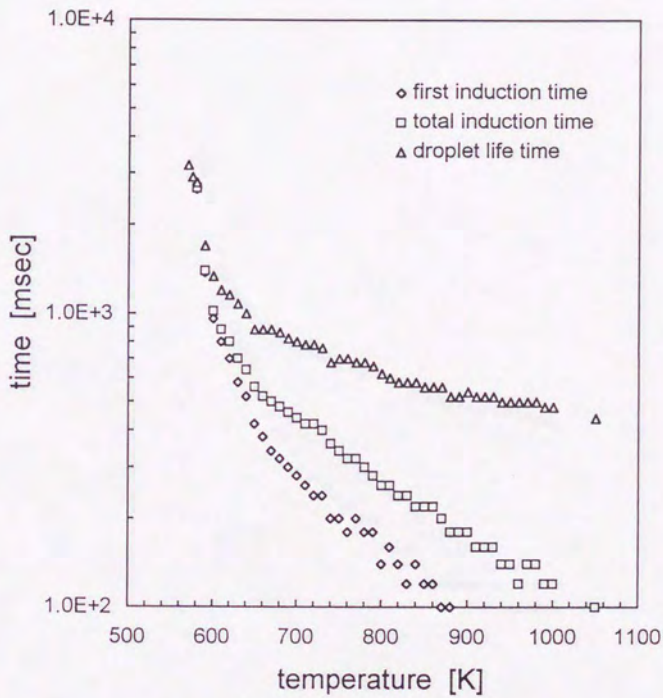
n-Dodecane droplet, normal gravity, $D_0 = 0.7-0.8\text{mm}$, $P_a = 0.3\text{ MPa}$

Figure C-10



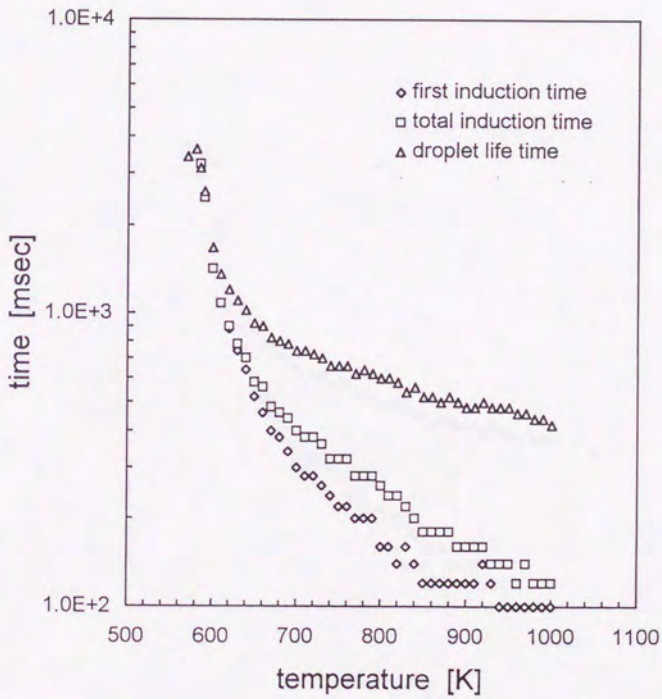
n-Dodecane droplet, normal gravity, $D_0 = 0.7-0.8\text{mm}$, $P_a = 0.4\text{ MPa}$

Figure C-11



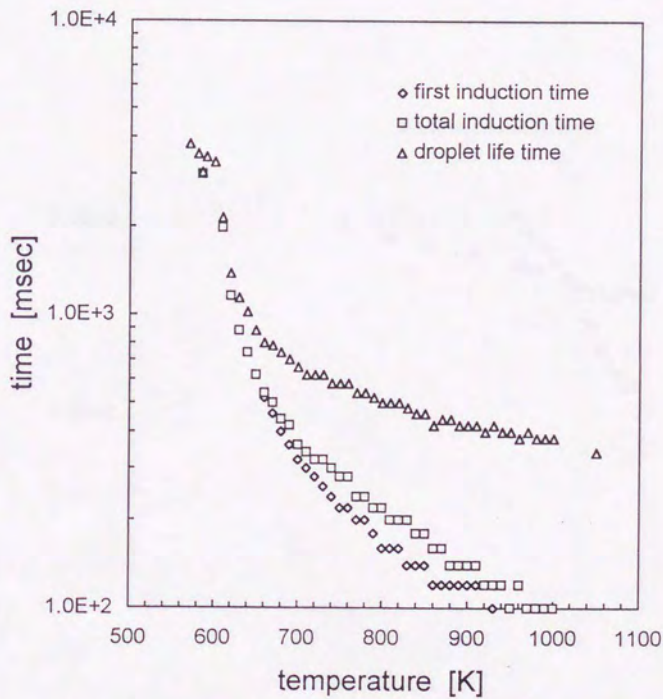
n-Dodecane droplet, normal gravity, $D_0 = 0.7-0.8\text{mm}$, $P_a = 0.5\text{ MPa}$

Figure C-12



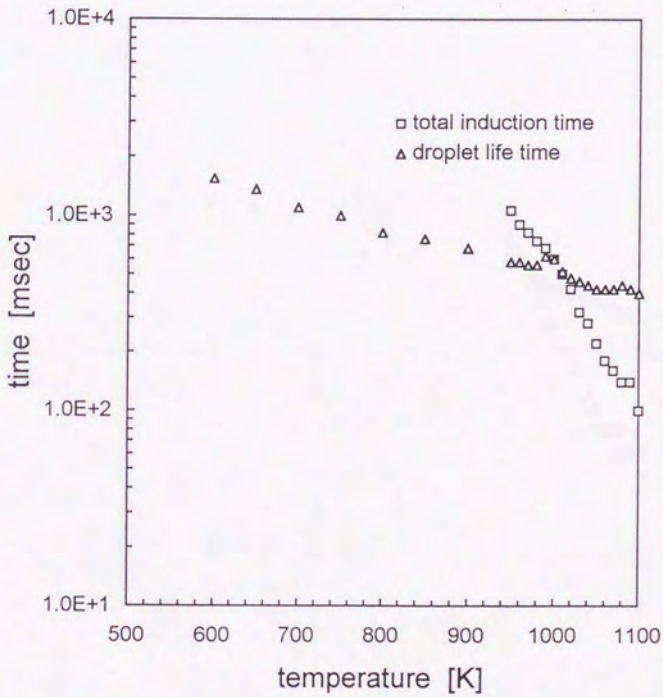
n-Dodecane droplet, normal gravity, $D_0 = 0.7-0.8\text{mm}$, $P_a = 1.0\text{ MPa}$

Figure C-13



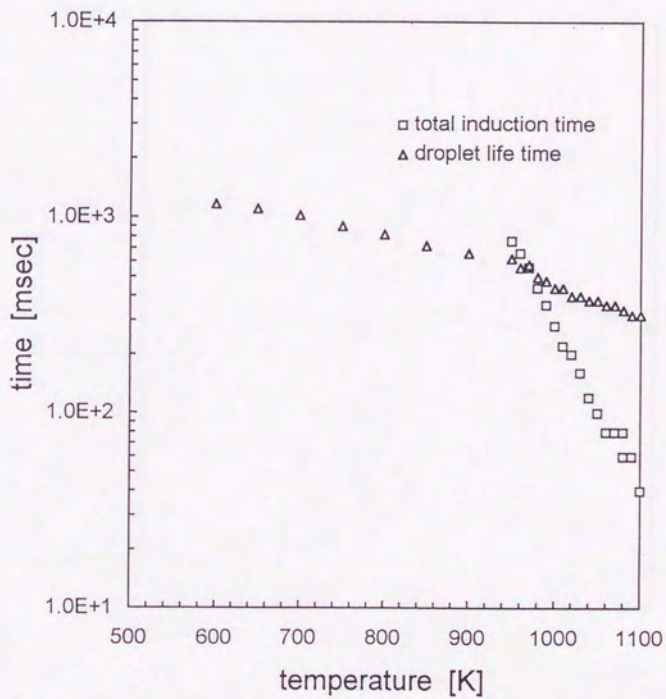
n-Dodecane droplet, normal gravity, $D_0 = 0.7\text{-}0.8\text{mm}$, $P_a = 2.0\text{ MPa}$

Figure C-14



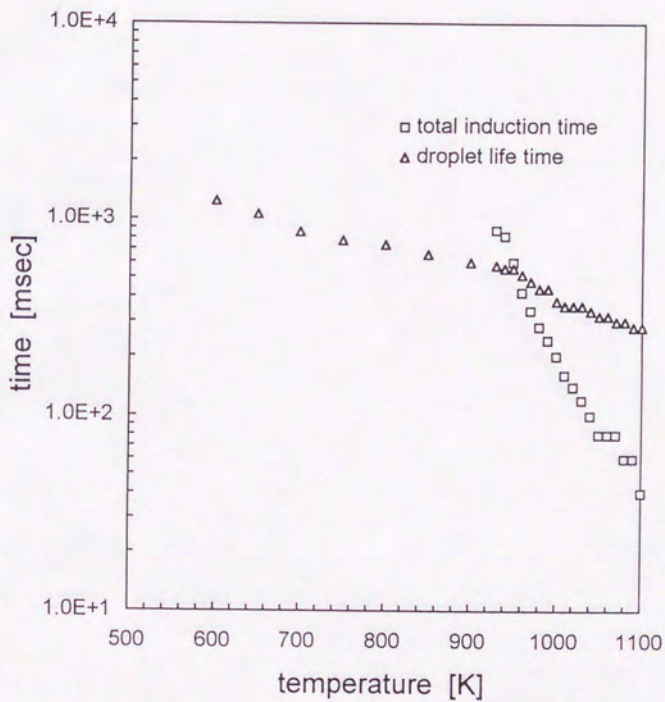
i-Octane droplet, normal gravity, $D_0 = 0.7-0.75$ mm, $P_a = 0.1$ MPa

Figure C-15



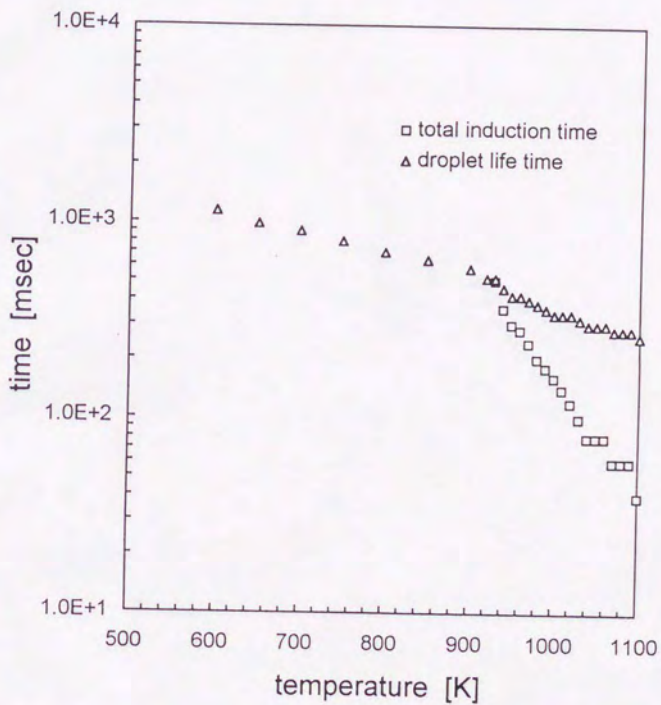
i-Octane droplet, normal gravity, $D_0 = 0.7-0.75$ mm, $P_a = 0.2$ MPa

Figure C-16



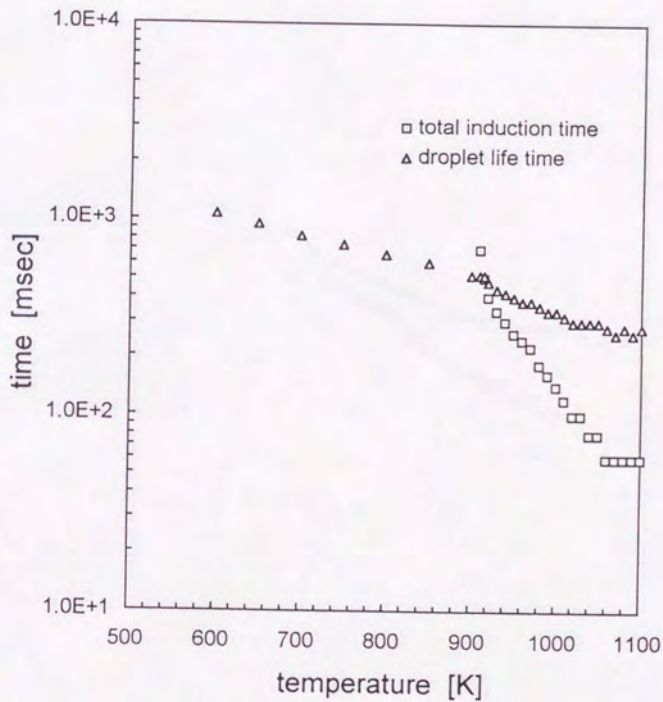
i-Octane droplet, normal gravity, $D_0 = 0.7-0.75$ mm, $P_a = 0.3$ MPa

Figure C-17



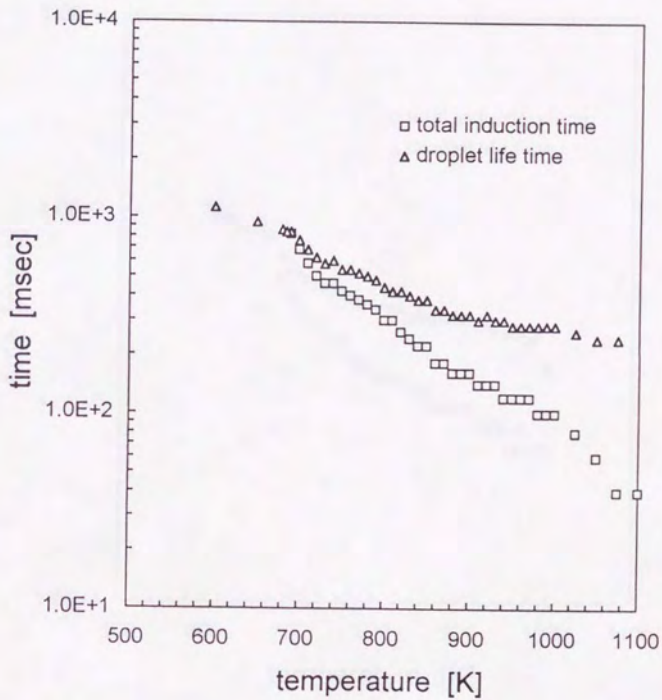
i-Octane droplet, normal gravity, $D_0 = 0.7-0.75$ mm, $P_a = 0.4$ MPa

Figure C-18



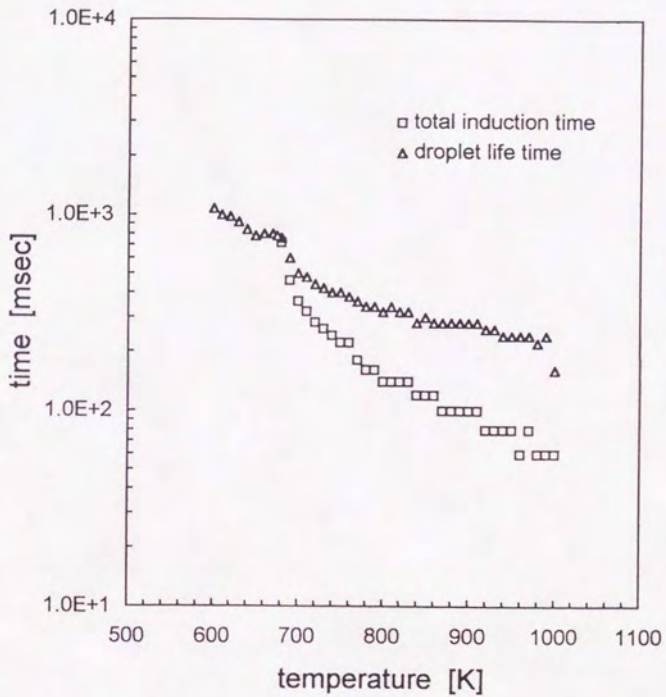
i-Octane droplet, normal gravity, $D_0 = 0.7-0.75$ mm, $P_a = 0.5$ MPa

Figure C-19



i-Octane droplet, normal gravity, $D_0 = 0.7-0.75$ mm, $P_a = 1.0$ MPa

Figure C-20



i-Octane droplet, normal gravity, $D_0 = 0.7-0.75$ mm, $P_a = 2.0$ MPa

Figure C-21

THE UNIVERSITY OF CHICAGO PRESS



Kodak Color Control Patches

Blue Cyan Green Yellow Red Magenta White 3/Color Black

Kodak Gray Scale



A 1 2 3 4 5 6 M 8 9 10 11 12 13 14 15 B 17 18 19

© Kodak, 2007 TM Kodak